STUDIES OF LONG HIGH-LEVEL RAILWAY BRIDGES IN HIGH SEISMIC ZONE

A Thesis Submitted
in Partial Fulfilment of the Requirements
for the Degree of

DOCTOR OF PHILOSOPHY

by

Sumantra Sengupta

Under the Supervision of

Prof. Anjan Dutta

Department of Civil Engineering
Indian Institute of Technology Guwahati
December, 2023

Dedicated to my Father

Declaration

I hereby declare that work presented in this thesis entitled "**Studies of long high-level railway bridges in high seismic zone**", submitted in partial fulfilment of the requirement for the award of the degree of Doctor of Philosophy in Civil Engineering, with specialization in Structural Engineering, is an authentic record of my own research work carried out in the Department of Civil Engineering, Indian Institute of Technology Guwahati under the supervision of Dr. Anjan Dutta, Professor, Department of Civil Engineering, IIT Guwahati.

The matter embodied in this thesis work has not been submitted by me for the award of any other degree, diploma associate-fellowship, fellowship or its equivalent to any University or Institute.

Date: 14.12.2023

Place: IIT Guwahati (Sumantra Sengupta)

Certificate

It is certified that the work contained in the thesis entitled "**Studies of long high-level railway bridges in high seismic zone**", by Sumantra Sengupta, a student in the Department of Civil Engineering, Indian Institute of Technology Guwahati, India, for the award of the degree of Doctor of Philosophy, has been carried out under my supervision and, that this work has not been submitted elsewhere for the degree.

Dr. Anjan Dutta
Professor
Department of Civil Engineering
Indian Institute of Technology Guwahati
Guwahati-781039, India

Acknowledgement

At the outset, I would like to mention that this thesis could not have seen the light of the day if Prof. Anjan Dutta's constant persuasion was not there. His appreciation of a professional engineer's continuous engagement in delivery of design and drawing for construction work throughout a major part of his day time, particularly if the engineer works in private organisation, is the primary reason of allowing me to take much longer time than normally a student takes to complete the research. I owe him beyond my capacity.

Being a professional engineer, working in civil engineering consultancy, is a challenging work and it is a real source of satisfaction when one sees one's design is standing and performing satisfactorily at site. My motivation of research is related to one of my such designs which is being under construction by Northeast Frontier Railway. Prof. Anjan Dutta was also a part of the same project and motivated me to work under him for the research work. His constant guidance in technical matters, at length discussion over various topics of my work is really appreciable.

I am also very much obliged to Prof. Sajal Deb, who was the chairman of my doctoral committee, for his constant encouragement and guidance. Prof. Sandip Das and Prof. Kaustubh Dasgupta, who were also members of my doctoral committee have guided me in various steps of my work.

My sincere gratitude to Mr. Amitabha Ghoshal, the then Director of STUP Consultants Pvt. Ltd. who has kindly permitted me to enrol myself in the Ph.D. programme. My sincere thanks to Mr. D.K. Gupta, my senior, with whom I have worked major part of my professional life in STUP, who has continuously encouraged me throughout my Ph.D. work.

I am also thankful to those people around me who have directly or indirectly helped me to achieve my target of completion of this research work, whose name I have not mentioned here.

I am thankful to my family members, my wife Jhunai and my son Supriya, who were there beside me constantly during this long tenure of my research work by showing their patience

and encouragement. My mother would be in tears in happiness when she would see that I have completed my PhD work.

Last but not the least, the person who would have been the happiest one in this world to see that I am submitting the PhD thesis work, at long last, who is no more in this world, my father Prof. Pran Ranjan Sengupta.

Sumantra Sengupta

Abstract

Bridges are integral part of the traffic system of any country and the proper design and construction of bridges are immensely important for advancement of any Nation. The design of the bridges are done as per the guidelines laid in various codes and standards. The guidelines are prepared based on the advancement in the technical knowhow and on the standard practices. The behaviour of the normal structures under different natural forces are understood well and they are well covered in codes and standards for the purpose of design and construction. Special studies may be required which may improve the design in terms of safety of the structure, economy and riding comfort.

North Eastern Frontier Railway (NFR) has envisaged to connect the so far unconnected North-eastern states of India with the mainland through railway. The railway lines pass through eastern trail of Himalaya resulting construction of large number of tunnels and bridges. The entire area is under seismic zone V. The heights of the piers vary from 20m to 141m with maximum length of bridges up to 700m. The substructures are comprised of tall large diameter hollow circular pier section made of RCC. The superstructures are comprised of open web girder (OWG) of steel construction. Inspection opening in the wall of the hollow piers are necessary both at the bottom and top of the pier. For the tallest bridge, the trains are running through the bridge at the level of 140m above the bed level over the rails which are laid on the multiple number of successive OWG superstructure, which are resting on variable height of pier. The design and construction of the bridges have been done following the available codes and standards. However, it is felt that further understanding of the behaviour of the tall piers in seismic case leading to safe movement of the train is necessary. For this purpose, some areas have been identified for further studies and the same have been considered as the present research work.

As per the Indian Railway Standard (IRS), the regular bridge structures are to be designed by response spectrum method (RSM) using code recommended spectrum. The irregular bridges are to be designed by RSM using site specific spectrum and by Time History Method (THM). Irregular bridges are those bridges where total height of pier including pile from its depth of fixity is more than 30m and where the difference of stiffness between the

successive piers are more than 30%. For RSM, response reduction factor (R) for the hollow pier section needs to be applied in the design. The THM is necessary to understand the track deflection in transverse direction to ensure safe movement of train.

It has been found that the codes and standards recommend unique values of R for various components of the structures. As such, none of these standards cover the recommendation of R value for hollow circular pier section. Literature study shows that various works have been done on small diameter solid and hollow circular section. However, the behaviour of large diameter hollow circular pier section is not adequately covered. Further, no study is available on the assessment of R value for pier with hollow circular section with wall opening.

For long bridges, consideration of asynchronous ground motion during a seismic event is important. Continuous rail tracks run over the long bridges and the transverse deflection of the track under seismic loading considerably vary between synchronous and asynchronous ground movement. The study of the same is important to ensure safe movement of the train. Literature study shows that various researchers have worked on the relative movement of the pier top on road bridges, but very little study is available on the effect of seismic loading on railway track mounted over a bridge deck supported on tall piers to ensure safe train movement.

The vehicle induced superstructure response is generally taken care in the design of superstructure by adequately strengthening it, which causes increase in superstructure mass. The seismic responses of the substructure increases accordingly. Introduction of TMD may reduce this vehicle induced superstructure response. As such, literature study shows that the effect of TMD in reducing vehicle induced response of highway bridges is covered by various researchers. The effect of TMD in controlling vehicle induced vibration response in high speed railway bridges with short span length has also been well covered by various researchers. However, very little information is available for long span OWG railway bridges.

In view of the above, three different topics have been chosen for the present study : 1) Response reduction factor of large diameter hollow circular pier section, 2) Asynchronous

motion and its effect on response of tall pier railway bridges and 3) TMD and its effect on vehicle induced vertical response of long span OWG railway bridges.

For the study of *R,* concrete stress-strain graph as per Mander *et al.* (1988) has been considered for generation of M-ϕ curve. Confinement effective coefficient (k_e) has been proposed for hollow circular section. The proposed value of k_e has been substantiated by FEA using a general purpose finite element software, Abaqus. The effect of various parameters like axial load (P/Af_{ck}), main steel ratio (ρ_{cc}), transverse steel ratio (ρ_s), spacing of transverse steel (S_h), grade of concrete (f_{ck}), grade of steel (f_y) and confinement width of the section on the value of *R* have been studied. The study has been done for pier diameter varying between 4m to 16m and the wall thickness varying between 0.5m to 2m. Attempt has been made to propose the value of *R* with respect to various design parameters for large diameter hollow circular pier section, for both with and without wall opening. The stress-strain relation of concrete recommended by Mander *et al*. (1988) is valid up to M50 grade of concrete. The present study is done considering M40 grade of concrete. The slenderness effect of pier plays an important role on *R*. As such the recommended values are applicable for non-slender pier with slenderness ratio lesser than 50. It has been found that compared to the recommended *R* values for hollow circular pier under present study, the code recommended single values for similar structural elements are on higher side in some cases leading to uneconomic design and are on lower side in some other cases leading to unsafe design.

The value of R increases with increase in transverse steel ratio (ρ_s), with decrease in vertical load (P/Af_{ck}) and with decrease in main steel ratio (ρ_{cc}). The proposed value of *R* varies from maximum 5.5 to minimum 1.6 depending on the factors as mentioned. Thus, the code recommended *R* value which is 3 irrespective of other depending parameters is not compatible with the actual behaviour and detailing of the structure as observed in the present study. The recommended *R* values of hollow circular section with door opening reduces with opening size and the reduction varies from 1 to 0.7 times of the value of *R* corresponding to section without door opening.

Asynchronous motion has been generated to cater for incoherence effect by using spatial correlation function suggested by Fenton (1991). Soil structure interaction model by using interaction between pile and soil has been generated in SAP. Three different soil spring curves have been used, namely, *P-y* curve to represent interaction between the lateral resistance of soil and pile displacement, *t-z* curve to represent interaction between shaft skin frictional force and relative movement of the pile with respect to the soil, *Q-z* curve to represent the mobilized tip bearing capacity and settlement. Acceleration time history has been converted to displacement time history to give the ground motion input in the pile spring for asynchronous motion as the governing equation requires the displacement time history. Two different seismic events, namely, El Centro earthquake and Koyna earthquake have been considered for this study. Under the considered earthquake excitation for the bridge under study, it is observed that while the pier top displacement reduces in the case of asynchronous motion as compared to synchronous ground excitation as we consider those piers along the direction of earthquake motion, the relative displacements at pier tops are however higher than those of the synchronous case. Further, it has been found that the effect of curvature in track due to synchronous motion and asynchronous motion is case sensitive and depends on the characteristics of ground motion itself.

The maximum relative displacement between top of piers is occurring at one location 407mm for asynchronous motion against 50mm for synchronous motion. The same maximum relative displacement at other location is 264mm corresponding to synchronous motion and 384mm for asynchronous motion. This suggests that the relative displacement is higher in case of asynchronous motion compared to synchronous motion. Similarly, the maximum torsional rotation in one superstructure of the bridge is found 2e-3 and 2e-5 for asynchronous motion and synchronous motion respectively which shows the value is much higher for asynchronous motion. The track curvature is more in case of synchronous motion for El-Centro EQ. The value is on average 0.75E-3 for synchronous motion and 0.25E-3 for asynchronous motion. The same track curvature is less in case of synchronous motion for Koyna EQ. It is 0.25E-3 for synchronous case and 0.4E-e3 for asynchronous case.

Vehicle Bridge Interaction (VBI) model has been generated for understanding the effect of vehicle induced response in the OWG steel superstructure. A 27 DOF vehicle model as proposed by Young and Wu (2001), has been adopted in the present study. Effect of track irregularity has also been considered to get the actual dynamic augmentation during vehicle movement. As the structure is simply supported, the vehicle induced response occurs mainly in first mode, which leads to use of single TMD. It has been found that the effect of TMD is significant with single bogie loading at some speed above the normal speed range. However, it is not at all significant for multiple bogie loading for any speed as the resonance effect does not occur. As such it has been concluded that the use of TMD is not effective for long span OWG steel railway bridges.

Under single bogie load (SBL) condition, maximum deflection occurs at 750 kmph speed, the speed at which the frequency of occurrence of SBL matches closely with the fundamental frequency of the structure and causes resonance. Some local peaks are visible at 250kmph and 400 kmph speed. Two cases of optimisation was done, one for TMD mass ratio less than 1% and the other is for TMD mass ratio between 1% and 2%. At 250kmph speed the reduction in midspan deflection is 16.2% against 0.6% TMD mass ratio. The same value is 20.8% against 1.2% TMD mass ratio. At 400kmph speed the reduction in midspan deflection is 11.5% against 0.6% TMD mass ratio. The same value is 24% against 1.76% TMD mass ratio. The maximum effect is at 750kmph speed at which the reduction in midspan deflection is 42.5% against 0.92% TMD mass ratio and 51.9% against 1.84% TMD mass ratio. For all the above cases the optimised damping ratio lies between 3% to 5%. In case of MBL, the speed *vs* deflection graph shows that a local peak occurs at 300 kmph speed. However, the deflection almost increases monotonically with higher speeds. As such, no resonance condition occurs under multiple bogie load (MBL) condition. As a result, the effect of TMD has been found almost Nil in case of MBL.

Table of contents

List of figures

List of tables

List of symbols and abbreviations

A_{cc} = Area of concrete core

b'' = Confinement width measured to outside of hoops;

d_s = diameter of confinement;

D_o = Outer diameter of hollow circular pier

D_i = Inner diameter of hollow circular pier

E_c = Flexural modulus;

g = Acceleration due to gravity (9.8 t/m^2)

I_e = Effective moment of inertia of section

I_{cr} = Cracked moment of inertia of section

I_{gr} = Gross section moment of inertia

k_e = Confinement effective coefficient

M_y = Yield moment capacity of the section

M_{cr} = Moment at which first cracking in concrete occurs

M_u = Ultimate moment capacity of the section

R = Response reduction factor

S_h = Spacing of stirrup;

TS = Tensile strength

YS = Yield strength

f_{ck} = Grade of concrete;

f_c = Stress in concrete;

f'_c = Strength of concrete;

f'_{cc} = Strength of confined concrete;

f'_l = Effective lateral confining pressure in concrete;

f_s = Stress in steel;

f_y = Yield stress of reinforcement steel;

f_{yh} = Yield stress of horizontal confining steel;

ε_c = Strain in concrete;

ε_{cc} = Strain in concrete corresponding to maximum stress of confined concrete;

ε_{co} = Strain in concrete corresponding to maximum stress of unconfined concrete;

ε_{cu} = Ultimate strain in concrete

ε_s = Strain in steel;

ε_{sf} = Fracture strain of transverse reinforcement

ε_{sp} = Spalling strain in concrete

ε_{50u} = ε_{c50u} = Strain at 50% of strength in falling curve of unconfined concrete;

ε_{50h} = Horizontal shift of strain at 50% of strength due to effect of confinement;

ε_{c50c} = Strain at 50% of strength in falling curve of confined concrete;

ρ_s = Transverse steel ratio;

ρ_{cc} = Main steel ratio;

σ_{ct} = Modulous of rupture of concrete

CDA	Coefficient of Dynamic Augmentation
CDP	Concrete Damage Plasticity Model
C/G	Centre of Gravity
DBE	Design Basis Earthquake
IRC	Indian Road Congress
IRS	Indian Railway Standard
kmph	Kilometre per hour
MBG	Multiple Bogie Loading
MBL	Multiple Bogie Loading
NFR	North-Eastern Frontier Railway, Govt. of India
OWG	Open Web Girder
PSD	Power Spectral Density function
SBL	Single Bogie Loading
SPA	Standard Pushover Analysis
SBL	Single Bogie Loading
SSI	Soil structure Interaction

TMD	Tuned Mass Damper
VBI	Vehicle Bridge Interaction

Chapter 1

Introduction

1.1. General

Indian Railway intends to connect the capitals of the four North-East states of India, namely Manipur, Mizoram, Nagaland and Arunachal Pradesh with Assam by railway link. The alignments of the railway lines pass through steep rolling hills of Patkai region, eastern trail of Himalaya, and as a result tall bridges need to be designed to connect the gorges. The tallest pier of such bridges span over a gorge at about 140m above its bed level with an overall length about 700m at rail level, refer Fig. 1.1. The piers are RCC hollow type with the tallest piers of 140m height, while in other piers on the slope of the hills vary from 50m to 90m height. The region is under high seismic zone and the design of these tall piers have been done as per the provisions laid in various national and international standards like IRS (Indian Railway Standard), IS (Indian Standard), IRC (Indian Road Congress), AREMA (American Railway Engineering and Maintenance-of-way Association), UIC (International Union of Railway) and Euro code. The design of the bridge components have been done following the guidelines laid in the above mentioned standards and some of the construction of the bridge structures have also been completed. Trains are also running at some of the stretches in Manipur, while at other locations the construction is on full swing.

During the design of the structures it was observed that the behaviour of the large diameter hollow circular pier under seismic excitation has not been adequately covered in different standards/ codes. Further the effect of asynchronous motion for long span railway bridges on continuous rail track and in turn on the movement of the train is also important to look into for safe running of train. Thus, more studies are needed to have improved understanding of long bridges with tall hollow piers in seismic zones.

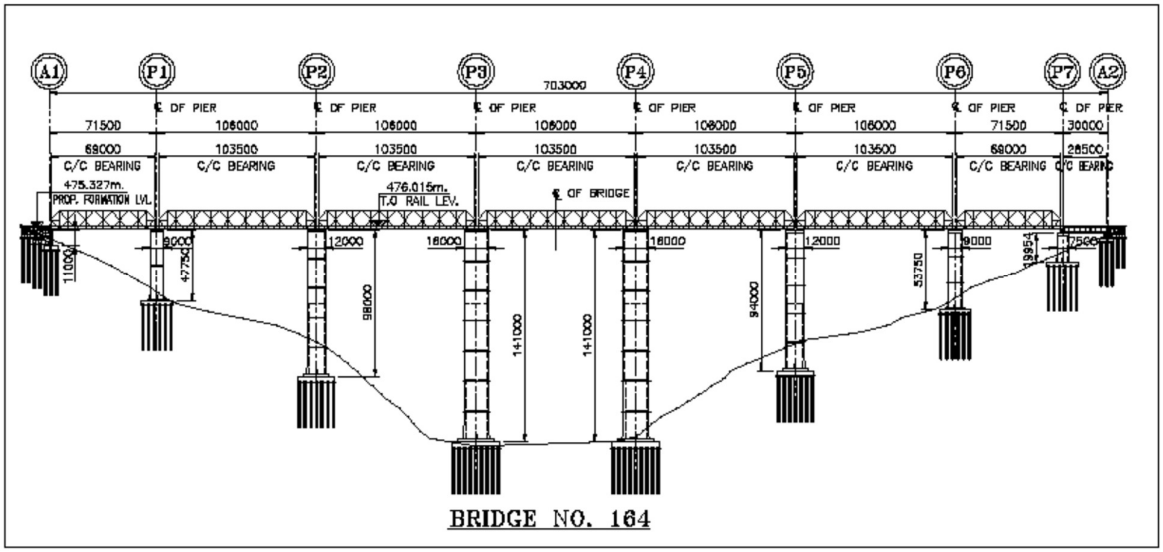

Fig. 1.1. Long span high level bridge (Bridge No. 164) located in Manipur

1.2. Response reduction factor (*R*) of large diameter hollow circular section

1.2.1. Response reduction factor (*R*)

The civil engineering structures are designed elastically for permanent loads like self weight of the structures, transient load like live load and occasional load like wind load where frequency of occurrence of the design load is high. However, in case of seismic load where the frequency of occurrence of the design seismic is low, the structures are designed inelastically taking into account the available ductility of the structure in addition to the reserve strength factor resulting from the additional reserve strength of structure over and above the design strength. *R* is thus the reduction factor with which the strength of the structure may be reduced compared to the strength, had the structure been designed elastically for the design seismic force. The basic idea is, as the structure has a very limited chance of experiencing the design seismic, the structure is allowed to go beyond its elastic limit during design seismic by using the reduction factor *R* in such a way so that the structure has the adequate capacity to sustain the rotation demand at its maximum moment location where the plastic hinge is allowed to form. This phenomena of inelastic behaviour

of the structure will not allow the structure to collapse during the design seismic occurrence and will also keep the cost of the structure low.

Ductility of a structure can be evaluated from the moment *vs* curvature (M-ϕ curve) relation. M-ϕ curve varies with respect to the following parameters: Stress-strain relation of concrete, stress-strain relation of steel, grade of concrete (f_{ck}) and grade of steel (f_y), axial load (P/Af_{ck}), main steel ratio (ρ_{cc}), transverse steel ratio (ρ_s), spacing of transverse steel (S_h). With the use of most widely used stress-strain relation of concrete and steel, parametric study of R value with respect to the other depending parameters as mentioned above can be done.

1.2.2. Concrete stress-strain relation

Various model of concrete stress-strain relation is available depending on the grade of concrete, namely, Kent & Park (1971), Mander *et al.*(1988), Saatcioglu (1992), Cusson (1995) and Hoshikuma *et al.* (1997). While all the above models excluding the model proposed by Cusson (1995) is based on grade of concrete up to M50, the model of Cusson (1995) is based on high performance concrete of grade between M60 and M120.

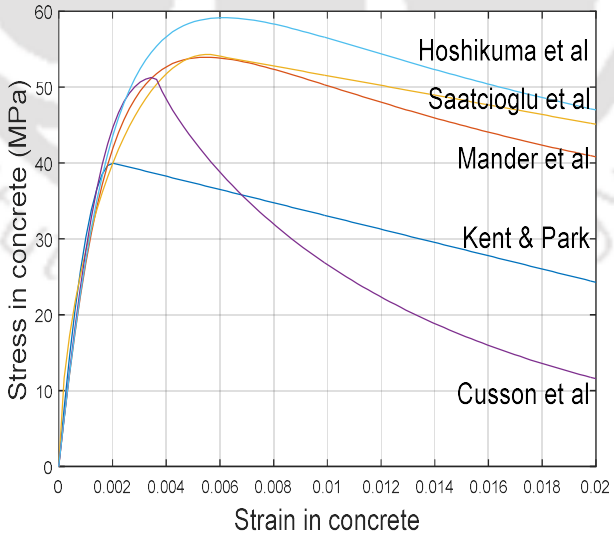

Fig. 1.2. Comparative Stress-strain relation of M40 grade concrete as per different models (Transverse steel ratio 1%)

Fig. 1.2 shows a comparative stress-strain relation of concrete proposed in the above models. The model proposed by Mander *et al.* (1988) is based on both rectangular and circular section which is thus most appropriate for study of circular pier section. There is no model available which has been generated with respect to hollow section.

1.2.3. Estimation of *R*

Moment curvature relation (M-ϕ curve) based on stress strain relation of concrete as per Mander *et al.* (1988) may be generated for different large cross section of hollow circular pier. The coefficient of effective confinement coefficient (k_e) prescribed in the model of Mander *et al.* (1988) for solid circular and rectangular RCC section needs modification in order to apply it in hollow circular section. Ultimate strain in concrete plays an important role in the ultimate curvature value sustained by any structural section. This ultimate strain may be estimated from strain energy balance principle as per Mander *et al.* (1988). The deflection ductility can be estimated by directly calculating the area under M-ϕ curve and the moment of the area about the cantilever end of a cantilever bridge pier structure. The average length of plastic hinge is an alternate approach towards estimation of ductility but the same has some limitation of adoption due to the fact that the M-ϕ curvature relationship is not linear due to the presence of axial force in pier. Consideration of effective moment of inertia of a cantilever pier is important over cracked moment of inertia as over the plastic hinge formation length, in between two successive cracked section, the un-cracked section property gives stiffening effect which influences the M-ϕ curve. Contribution of P-Δ effect is important in estimation of ultimate curvature in order to avoid post yield negative stiffness. Effect of slenderness plays an important role in the M-ϕ curve and depending on value of slenderness ratio the ultimate curvature reduces. As per the established theory, yield reduction factor is same as deflection ductility when the structure is flexible. Thus, for flexible structure the R value may be considered as deflection ductility multiplied by reserve strength factor which is the factor of safety remains in the standard design of the structure.

1.2.4. *R* of large diameter hollow circular pier

It was found that the Response reduction factor (*R*) for large diameter hollow circular section is not adequately covered in the different standards. There is lack of uniformity in the recommendations of the value of *R* in different standards for different members of structure. In general it has been found that the single value of *R* has been recommended in all the standards rather than defining it as a function of various influencing parameters like axial force, transverse reinforcement ratio etc. Moreover, literature study reveals that the value of *R* has been studied by many researchers for solid and hollow circular RCC pier section, and small diameter hollow circular section, but none on large diameter hollow circular section. With these shortcomings in mind, a study has been undertaken to assess the value of *R* in large diameter hollow circular section as a function of various depending parameters. The effect of opening in the wall of the hollow circular pier has also been studied.

1.3. Asynchronous motion and its effect on response of tall pier railway bridge

1.3.1. Asynchronous ground motion

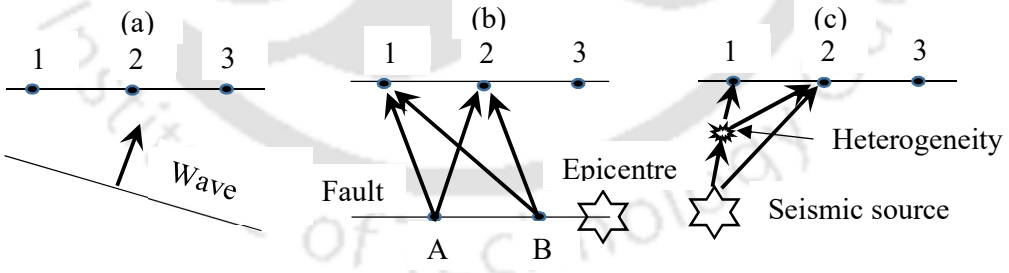

Fig. 1.3. . Sources of incoherence ground motion: (a) Wave passage effect causes inclined wave front to reach locations 1, 2 & 3 at different times; (b) Extended source effect causes waves due to rupture at A and B to reach points 1 & 2 at different times; (c) Scattering of waves by heterogeneity causes different waves to arrive at different locations at different times [Kramer (1996)].

The spectral properties of ground motion get altered because of (a) wave passage effects which is due to the time shifts in the arrival of the seismic waves at the supports, Adanur *et al.* (2017); (b) the incoherence effect which is due to extended source effect in which different frequencies in the relative geometry of the source and site produce different time shift, Zerva and Zerva, (2002), Konakli and Kiureghian, (2012); (c) the local soil effect which causes scattering (reflection, refraction etc.) of waves by inhomogeneity along the travel path. Fig. 1.3 depicts the above different causes of asynchronous motion diagrammatically.

Incoherence effect can be given by the two factors. One is spatial correlation function which is a function of distance between the two points of measurement of ground acceleration, shear wave velocity of the soil medium through which the wave is propagating and frequency of vibration and coherence parameter, which also depend on the soil medium. The other one is Power Spectral Density function (PSD). There are various spatial correlation functions are available which have been suggested by various researchers. Amongst them the model suggested by Fenton (1991), is the most widely used for the purpose. The PSD is given by Kanai (1957) and Tajimi (1960) which was later modified by Clough and Penzien (1975).

1.3.2. Effect of asynchronous motion on railway bridge structures

Indian railway code has recommended that spatially varying ground acceleration is necessarily to be considered in analysis for long span structures of total length more than 700m. However, in case of structures with varying height of pier, which occurs for bridges in hilly terrain, the structural behaviour is complicated and its effect on track movement may be critical even if the overall length of bridge is less than 700m. Literature review suggests that the considerable amount of research has been done to understand the effect of asynchronous ground motion in long span road bridges, however very little work has been done for the long span and high level railway bridges and the final effect on the continuous track which is important for the safe movement of the train during seismic. For this purpose, different time histories with proper scaling to ensure the target spectrum compatibility and with the due variation in ground motion at different pier points against asysnchronous

behaviour need to be considered and the track movement to be studied in view of safe movement of the train during seismic.

In case the local soil is uniform all along the bridge length, effect of wave passage and incoherence effect, these two parameters may be considered to generate asynchronous motion. Local soil effect changing the frequency content does not affect the study then. In order to undertake the analysis with asynchronous motion, soil structure interaction effect should be considered with modelling of soil elements as nonlinear spring all along the depth of the pile foundation.

1.4. Tuned Mass Damper (TMD) and its effect on vertical response of long span steel through type girder during train movement

1.4.1. Coefficient of Dynamic Augmentation (*CDA*)

The effect of seismic load on pier from supesrtructure depends on the mass of the superstructure. The mass of superstructure in turn depends on the LL and its dynamic effect. Coefficient of Dynamic Augmentation (*CDA*) recommended in IRS Bridge Rules (2014) is defined as the percentage of increase in LL due to its dynamic nature. The value is inversely proportional to span length and is applicable up to velocity of train 160 kmph. The application of *TMD* may reduce the CDA which in tun may reduce the mass of superstructure.

1.4.2. Vehicle Bridge Interaction (VBI)

VBI along with track roughness gives the actual behaviour of the structure during movement of the train. Multiple degrees of freedom vehicle may be modeled and analysis can be done to get the dynamic response of the structure. *CDA* recommended in IRS is not based on detailed analysis of behaviour of the structure involving *VBI* and track irregularity.

1.4.3. TMD parameters

Parameters on which the effect of *TMD* on the response of the structure depends are the mass m, stiffness k and the damping c of the *TMD*. The mass of *TMD* may be considered

as a fraction of the total mass of the superstructure. It cannot be very high as the same will enhance static response of the structure. The value is generally considered between 0.5% to 2%. The damping ratio of the *TMD* is generally considered to be varying between 2% to 10%. The frequency ratio is kept between 0.995 to 1.05 as the effect of *TMD* is maximum for this frequency ratio range. Optimisation of these parameters can be done by using any optimisation algorithm. Further, long span superstructure predominantly vibrates in first mode under dynamic behaviour of LL and hence only single *TMD* may be considered at mid span.

1.4.4. Application of *TMD* in long span superstructure

There are studies available on the effect of *TMD* on the dynamic bahaviour due to Live Load for small span superstructures. However, the same effect on long span railway bridge is not available. The Indian Railway Standard recommends the value of *CDA* as a function of span length of the structure and is proportional to the speed of the train. However, *CDA* is basically a function of flexibility of the structure, the proximity of the self frequency of the structure to the frequency of occurrence of the load. The effect of *TMD* on the *CDA* ie on the midspan deflection and strains at various members of the truss may cause reduction in the response.

1.5. Objectives of research

In view of the hereinbefore discussion, following topics have been selected for further study so that the behaviour of the long span high level railway bridge structure under seismic load can be understood better:

A. Response reduction factor of large hollow circular section
B. Asynchronous motion and its effect on response of tall pier railway bridges
C. Tuned Mass Damper (TMD) and its effect on reduction in vertical response of long span open web steel girder bridge during train movement.

A typical long span high level railway bridge as shown in Fig. 1.1. has been considered for this purpose. The study of value of *R* for large diameter hollow pier has been done keeping in mind the behaviour of actual hollow pier structure under construction as shown in Fig. 1.1. The asynchronous motion and its effect on the railway track and subsequently on the

safe movement of train and the effect of TMD on the dynamic response of the structure has also been done keeping in mind the superstructure under construction as shown in Fig.1.1

The present study covers the above topics in detail with the intended objectives of enhancing the understanding of design of long tall pier railway bridges in seismically active zones.

1.6. Scope of research

In view of the hereinbefore discussion, the detailed scope of work to achieve the objective of the research is as below:

Response reduction factor of large hollow circular section

- To find out the most suitable stress-strain model of concrete applicable for hollow circular section (Model of Mander *et al.* (1988) has been used as the same is based on both rectangular and circular cross section)
- To prepare the suitable modification in the stress strain relation of concrete to include the effect of hollow section (Modification in the value of effective confinement coefficient which is available for solid section)
- To justify the modification by FE analysis
- To prepare the M-ϕ curve of large diameter hollow circular pier with varying P/Af_{ck}, ρ_{cc}, and ρ_s for tall piers of large diameter hollow circular section varying from outer diameter 4m to 16m with wall thickness varying from 0.5m to 2 m
- To find out ultimate concrete strain based on strain energy principle at which the confining reinforcement fails.
- To find out the deflection ductility and reserve strength factor from the M-ϕ curve.
- To do the parametric study of R value of large diameter hollow circular tall pier
- To study the effect of inspection door opening in the hollow pier on R

Asynchronous motion and its effect on response of tall pier railway bridges

- To study the generation of asynchronous motion taking in to consideration the wave passage effect and incoherence effect
- To select the suitable ground acceleration time history recorded in rocky strata and medium soil strata (The soil strata in north-eastern states where the bridges are under construction and are under the present study is of rocky strata) which are used for generation of asynchronous motion
- To prepare the soil structure interaction model of bridge under study
- To prepare the ground displacement time history for asynchronous ground motion input in the analysis of the structure
- To find out the transverse track deflection under different time instances to get the most critical track curvature
- To compare the effect of critical curvature and the corresponding safe speed of train for synchronous and asynchronous ground acceleration.

Tuned Mass Damper (TMD) and its effect on reduction in vertical response of long span open web girder (OWG) bridge of steel construction during train movement

- To prepare the *VBI* model along with track irregularity of the bridge under study
- To introduce the single TMD parameters at the midspan of the VBI model of the structure (As the predominant vibration of the structure under movement of LL is in first fundamental mode in vertical direction, more than one TMD will not enhance the effect and hence single TMD has been considered. In three dimensional model of the open web through type steel girder under study, two TMD, one at the midspan of each open web girder is considered)
- To study the effect of TMD on controlling the vehicle induced vibration response .

1.7. Organisation of thesis

The thesis mainly focusses on the estimation of *R* value for large diameter hollow circular tall pier section; effect of synchronous and asynchronous seismic ground acceleration on railway track movement and its effect on the safe movement of train; and lastly on the effect

of *TMD* on the dynamic response of the long span open web through type steel girder during movement of the train. The thesis has been organised in the following way:

Chapter 1 introduces the study which has been undertaken in this thesis. It speaks on the general concept of *R* and what are the different influencing parameters on which *R* depends. Stress-strain relations of concrete which is the basic parameter on which the *R* value depends are shown. General concept of how *R* is estimated has been discussed and also the specific scope of the present study on *R* is furnished. The general concept of asynchronous ground motion and its possible effects in railway bridges has been discussed. The exact scope of effect of asynchronous motion in track movement of railway bridge undertaken in the present study has also been furnished. The general concept of *VBI* model along with the *TMD* parameters which may affect the dynamic deflection during train movement has been discussed. The exact scope of the present study on the effect of *TMD* on long span steel through type railway bridge has also been furnished.

Chapter 2 discusses on the literature review on the specific topic under study. It shows that how the *R* value suggested in different study by the different researchers concludes that they are not in line with the recommended *R* value in various standards. It shows the inadequacy in the available study of value of *R* in large diameter hollow pier section. The effect of asynchronous motion in different type of bridge structure that has been studied by various authors has been discussed. The inadequacy in the available study on the movement of railway track of long span tall railway bridges during synchronous and asynchronous ground moment has been shown. Available study on the effect of TMD on dynamic response during movement of LL in various types of bridge structure has been discussed. The inadequacy in the available study on the effect of TMD on long span open web through type girder railway bridges has been shown.

Chapter 3 discusses on specific topic on response reduction factor I of large diameter hollow circular section of tall pier. It describes the methodology adopted in the estimation of *R*, the comparative discussion of different stress strain relation proposed by various authors, the stress strain relation of reinforcement steel. The effective confinement coefficient applicable for solid rectangular and circular section has been discussed. The

effective confinement coefficient for hollow circular section that has been proposed in the present study has been discussed along with the FE analysis done in in Abaqus which justifies the adopted value. Ultimate concrete strain up to which the stress-strain relation of concrete to be considered and how the value has been adopted has been discussed. Ultimate curvature considered for the estimation of *R* has been discussed for which avoiding the negative stiffness effect in post yield behaviour can be ascertained. Finally, a parametric representation of *R* has been furnished recommending the value of *R* that should be considered for the design of large diameter hollow circular tall pier section.

Chapter 4 discusses on the asynchronous ground motion and its response of tall railway bridge and particularly its effect on the track displacement to ascertain the safe movement of train. It discusses on general theory of generation of asynchronous motion, wave passage effect, incoherence effect, reflection and refraction of wave due to local soil effect and various parameters that has been considered under present study for generation of asynchronous motion. The soil structure interaction model has been discussed with different pile springs like end bearing spring, lateral passive resistance spring and vertical friction spring. Finally, the effect of synchronous and asynchronous seismic ground acceleration on long span railway bridge structure has been discussed with specific focus on the effect of transverse track displacement and corresponding safe movement of train.

Chapter 5 discusses on TMD and its effect on vertical response of long span steel through type girder during train movement. It discusses on how the VBI model along with the track roughness has been generated for the open web through type steel long span girder. The TMD parameters that has been used and how the parameters have been introduced in the VBI model using the governing equations of TMD has been discussed. The critical velocities for different number of bogie load, single and multiple has been discussed. Finally, the effect of TMD on the dynamic response of the girder during train movement at different speed has been discussed. The dynamic response includes the midspan deflection, strain in central top chord, central bottom chord and in the end diagonal.

Chapter 6 concludes with a summary of the results and set of conclusions addressing the significance of the findings in the study. Finally, the scope of future work has been identified.

Chapter 2

Literature review

2.1. General

The values of response reduction factor *R* has been suggested in various codes for solid RCC section to be used in different components of structure. Literature study has been done to understand the extent of research undertaken to find out the value of *R* in different type of sections and structural components. Further, for tall railway bridges having long length of bridge, the track deflection in transverse direction is important for safe movement of train. Literature study has been done to understand the extent of work on the behaviour of bridge structures under synchronous and asynchronous ground motion. Vehicle induced vibration response on the long span structure may be controlled by the use of TMD, which may reduce the quantity of steel of superstructure leading to reduced seismic response due to reduction in self-weight of superstructure. Literature study has been done to find out the extent of work that has been done on the use of TMD in controlling the vehicle induced vibration response of bridge superstructure. The present chapter discusses in detail on the literature review in connection with the above three topics and identifies the gap in research to arrive at the motivation in choosing the objectives of the present work.

2.2. Response reduction factor *R*

General approach of seismic design of structure is response spectrum method, which is a simplified indirect method of analysis accounting for non-linear behaviour of the structure. The response reduction factor *R* applied in this method for designing of various components of the structure are available in various codes/ standards.

Effect of confinement on the stress-strain relationship of concrete has been studied by Saatcioglu *et al.* (1992) and Cusson *et al.* (1995). In their paper Saatcioglu *et al.* (1992) has shown the effect of confining reinforcement on circular, square and rectangular section of concrete grade varying between M20 to M32. They have shown the enhancement of ultimate strength, corresponding strain and enhancement of ductility with respect to the

confinement steel stress. The generalized stress-strain relation proposed by them has been shown in Fig. 3.4. Cusson *et al.* (1995) has shown effect of confining reinforcement on square section of high strength concrete of grade varying between M60 to M120. The generalized stress-strain relation proposed by them has been shown in Fig. 3.5. Kent and Park (1971) has shown the effect of confining reinforcement up to the grade of M55 causes enhancement in the ductility of the behaviour of concrete without increasing the strength (Refer Fig. 3.2).

Miranda and Bertero (1994) reviewed the work done on the strength reduction factor carried out in the period of 30 years between 1964 and 1994. The evaluation of the results indicates that the *R* value primarily depends on the maximum tolerable displacement ductility demand, the period of the system and soil condition of the site and the overstrength factors. The response reduction factors prescribed in the codes (till 1994) primarily accounted for damping, energy dissipation capacity of the sections and the overstrength. However, the values are mainly based on the performance of the different structural systems in previous strong earthqaukes. There remains thus lack of rationality in the values suggested in the codes. The paper concluded that the use of ductility, period and site dependent strength reduction factors like those presented in the paper together with estimates of the overstrength of structure and ductility demand can lead to a more rational and transparent seismic design approach than the approach used in seismic codes till 1994.

Constantinou and Quarshie (1998) studied non-linear behaviour of seismically isolated and non-isolated bridges under seismic excitation characterised by AASHTO ground motion spectra. The study investigated the displacement ductility demand in the substructure of seismically isolated bridges and compares it with that of seismically non-isolated bridges. The paper concludes that the *R* value of the substructure of seismically isolated bridges is less than that of sesismically non-isolated bridges. This is mainly because of elastic or nearly elastic behaviour of the substructure is necessary for proper behaviour of the isolation system and the isolated bridges exhibit more sensitivity in non-elastic behaviour of the substructure due to variability of seismic vibration of ground.

The Indian Road Congress codes also recommend that for design of pier, the value of *R* of bridges with neoprene bearing should be half of that of for bridges with fixed type of bearing.

Kappos (1999) derived Bahaviour factor *q* or Response reduction factor *R* for some catastrophic EQ happened in Greece. The paper suggests that the ductility dependent *R* characterised by features of the structure are not adequately covered in the codes particularly in European seismic code EC8. The paper has concluded that *R* in rock sites is significantly in lower side in the code whereas the same in alluvial soil or soft soil is in higher side. The overstrength component of *R* as suggested in the paper is in higher side for low rise frame compared to the high rise frame. It also concludes that the values of *R* obtained are in higher side than that is given in the standards particularly for the structures with high and intermediate frequency structure.

Yeh *et al.* (2002**),** experimentally studied the behaviour of hollow rectangular pier section of 1.5mx1.5m size with 300mm wall thickness. Few studies were done on performance of hollow bridge columns are by Hoshikuma and Priestley (2000), Maekawa *et al.* (2001), Ranzo and Priestley (2001), and Mo *et al.* (2003).

Paraskeva *et al.* (2006) focused on application of modal pushover analysis (MPA) in long bridge as an extension of standard pushover analysis (SPA) or non-linear static (pushover) analysis and compared the result with non-linear time history analysis (NL-THA). Response spectrum analysis is a very useful tool for designing structure but it cannot predict the failure mechanism or redistribution of force after formation of plastic hinge during strong ground motion. SPA can predict the same. However, SPA identifies the plastic hinge and predicts the force distribution and the target displacement range under the first fundamental mode only by means of monotonically increasing the lateral forces with an invariant spatial distribution. Force distribution and the target displacement range may differ for higher modes which cannot be predicted by SPA. Non-liner time history (NL-THA) can predict the actual force distribution in structure under inelastic range. MPA is an alternate to the NL-THA and is comparatively less involving. Separate pushover curves are generated for each mode. Pushover analysis has been carried out separately for each mode.

Contribution of each mode to calculate the response is carried out using appropriate combination rule (SRSS or CQC). Although this combination is not permitted as the modes under inelastic range is not uncoupled anymore, the result compared to NL-THA has been found does not vary widely. In another method called incremental response spectrum analysis (IRSA) each time a new hinge forms in the structure elastic modal spectrum analysis is performed considering the changes in the dynamic properties of the structure. In the study of Paraskeva *et al.* (2006) the method for the analysis has been suggested and the same has been applied at some specific cases. However, the general applicability needs more case studies.

Kim *et al.* (2012) tested hollow bridge columns under constant axial load and a pseudo static, cyclically reversed horizontal load and the effect of ductility and dissipated energy were investigated. Analysis has been done by them using nonlinear finite element programme and the results were compared with the test results. They considered RCC hollow square column of over all size 400mm x 400mm with wall thickness 100mm and PSC hollow circular section of outer diameter 800mm and wall thickness 220mm. The grade of concrete considered was between M30 and M40. In their paper Kim *et al.* (2012) studied the RCC hollow square column of overall size 400mm x 400mm with wall thickness 100mm and PSC hollow circular section of outer diameter 800mm and wall thickness 220mm.

Kappos *et al.* (2013) estimated response reduction factor for bridge piers from corresponding pushover curves of the sections by considering both overstrength factor and ductility factor and the values obtained thus has been compared with the code specified values (Eurocode 8 and AASHTO) which turns out to be always in safer side. The paper dealt with two different cases of bridge, one is without bearing in superstructure where the piers will behave inelastically at its failure mode and non-linear static pushover curve has been used and the other is with bearing. The R factor or the q factor (Behaviour factor) of the piers in bridges thus obtained from the product of two components, the overstrength factor (q_s) defined as the ratio of yield strength to the design base shear and the ductility factor (q_u) derived from the available displacement ductility of the bridge. They observed that many researchers worked on either on the single pier of the bridge or have considered

only the ductility factor in their study of generation of *R* or *q* factor of the bridge. They considered in their study the direction of EQ in any arbitrary direction to the axis of the bridge and the *R* factor or *q* factor has been derived accordingly. It has been concluded that the effect of EQ in any arbitrary direction is bounded by the effect in two main orthogonal direction ie in longitudinal and transverse direction.

Mondal *et al.* (2013) developed *R* in RC moment resistant framed structures, designed and detailed following Indian Standards, from different accepted performance limits. Two different performance limits has been considered in the study, one is story drift limit and the other is member rotation limit as per ATC 40. The study has been done on component-wise computation of *R*, consideration of performance based limit both from member wise aspect and structure as whole aspect, modelling of RC section behaviour, effects of various analysis and design consideration on *R*. The paper concludes that the computed *R* value is in lower side than that suggested in Indian standards which suggests that the Indian standards are not in conservative side and may lead to potential hazardous situation in reality. The study is based on specifically zone IV.

Cardone (2014), investigated the displacement limits of piers, abutments, joints and bearing devices. As response spectrum method does not provide any idea of actual collapse mechanism, inelastic deformed shape and ductility demand of the structure, simplified non-linear displacement-based method for the seismic assessment of existing structures are being developed for the last two decades. All the methods combine pushover analysis (POA) of a nonlinear MDOF model of the structure with response spectrum analysis of an equivalent SDOF system to provide an estimation of the global displacement response of structures for a given peak ground acceleration (PGA). Antonious *et al.* (2004) proposed displacement adaptive pushover (DAP) procedure in which loading vector of lateral displacement is applied to the structure and continuously updated during the analysis, according to the modal shapes and participation factors at each analysis step. The Direct Displacement based seismic assessment (DDBA) derives the inelastic deformed shape of the bridge through effective modal analysis (EMA). The displacement capacity of the structure then compared with displacement demand produced by a given EQ. In his paper Cardone (2014) proposed the procedure for DDBA for definition of the so-called

performance displacement profile (PDP) of the bridges. The displacement limits associated to different displacement shapes of piers, abutments, joints, bearing devices have been defined and discussed. It also examined the different approaches for the definition of Performance Displacement Profile including Adaptive Pushover Analysis, Effective Modal Analysis or rational analysis of simplified bridge model.

Liang *et al.* (2018) studied effect of confinement in circular hollow concrete columns. They showed that with wall thickness ratio 0.1 (wall thickness/diameter) one layer of transverse reinforcement provides satisfactory confinement whereas for wall thickness ratio up to 0.2, two layers of reinforcement connected with cross ties are more appropriate to get satisfactory confinement. However in practice two layers of reinforcement is necessary as unreinforced concrete surface is not recommendable. Kulkarni (2016) studied seismic performance of bridge with tall piers in connection with Indian railway's construction of bridges in north-eastern hilly terrain and suggested the value of *R* recommended in Indian codes gives satisfactory performance of tall bridges.

There are single values of *R* recommended in different codes and standards corresponding to various components of structures. In IS 13920 (2016), the special confining reinforcement or transverse reinforcement (ρ_s) has been recommended as a function of dimension of the section of the structural element, grade of concrete (f_{ck}) and grade of reinforcement (f_y). In IRC 112 (2020), the special confining reinforcement has been recommended based on the same factors as IS code has suggested in addition to axial force (P/Af_{ck}) and main steel ratio (ρ_{cc}).

2.3. Asynchronous motion and its effect on long span bridges

Asynchronous motion of ground hits different foundations of long span bridges owing to the following effects. The spectral properties of ground motion get altered because of (a) wave passage effects which is due to the time shifts in the arrival of the seismic waves at the supports, Adanur *et al.* (2017); (b) the incoherence effect which is due to extended source effect in which different frequencies in the relative geometry of the source and site produce different time shift, Zerva & Zerva (2002), Konakli & Der Kiureghian (2012); (c)

the local soil effect which causes scattering (reflection, refraction etc.) of waves by inhomogeneity along the travel path.

The asynchronous ground motions were started being analysed after the installation of dense instrument arrays since 1979 with El Centro differential arrays. Before this, the spatial variation of the motions was attributed to the wave propagation effect only [Bogdanoff JL *et al.* (1965)], [Nelson I *et al.* (1977)], [Sandi H. (1970)]. Numerous researchers have done work on spatial variation of seismic ground motion and its application on long span structures. In general, the spatial variations of seismic ground motions are evaluated from data recorded at dense instrument arrays.

The behaviour of the structure during synchronous and asynchronous ground movement depends on the modelling of the structure considering soil structure interaction. Soil modelling was initiated by considering linear stiffness of soil for near field soil and it was however observed to give erroneous results. Subsequently, non-linear idealisation of near field soil was introduced by API (2008). It was observed to provide more reliable results, where the near field soils undergo non-linear behaviour for small lateral strains. Three types of non-linear soil springs are considered to represent different interactions as Tip bearing using *Q-z* curves, shaft skin friction using *t-z* curves and lateral resistance of soil on pile using *P-y* curves. In the case of *Q-z* curves concerning cohesionless soil, the tip soil resistance continues to increase with the settlement of pile and 10% of pile diameter settlement is required for full mobilization of tip bearing capacity of the pile as proposed by Reese *et al*. (2006) and API (2008). The modelling of shaft frictional force with a pile for cohesionless soil is carried out by computation of maximum mobilised skin friction at various depths given by FEMA 356, (2000). Further API (2008) recommended a relation for a *t-z* curve to be bilinear in cohesion less soil. In modelling of *P-y* curves for sand, the ultimate resistance is calculated from the recommendations given by Matlock *et al*. (1980), which is a Hyperbolic formulation and observed to be the best fit from the experimental results. The same recommendation for *P-y* curves was adopted by API (2008).

The Far-field soil spring constant is linear, independent of pile diameter and varies linearly with depth as per Martin, (1995), for both cohesive and cohesionless soil.

When a pile-supported bridge is located in an earthquake-prone area, the seismic performance evaluation of the bridge including the soil structure interaction (SSI) effects should be included in the analysis. The effect of SSI has been considered as significant particularly in the case of tall pier bridges. There are several such cases where the failure of the structure is due to neglecting the SSI effects. Extensive numerical modelling were carried out by researchers and observed that the non-consideration of SSI as one of the reasons for the failure of Hanshin Expressway in 1995 under the action of Kobe earthquake. Therefore, understanding the SSI and its numerical modelling with respect to the soil on which structure rest is considered as highly important.

When an earthquake occurs, the soil supporting a structure vibrates and induces vibration in the structure. The vibration of the structure further affects the vibration of the surrounding soil and this mutual interaction of structure and soil is called Soil-Structure Interaction (SSI). SSI is classified into two types as follows:

- The displacement caused by earthquake ground motion in the soil where no structural components present is called free-field motion. The presence of the foundation elements in the soil causes the foundation motion to deviate from the free field motion called the Kinematic Interaction. Kinematic interaction has three primary causes i.e., presence of stiff foundation elements, variation of ground motion with depth and scattering of waves at corners and edges.
- Inertial interaction describes how the inertial response of a structure cause base shear and moments that cause displacement of foundation relative to the free-field motion. This causes additional rotations and displacements in the structure thereby changing the fundamental frequency.

There are two broad approaches for the introduction of SSI in the analysis. One is the Substructure method and the other is the Direct method. In substructure method, the piles are modelled up to its depth of fixity depending on the stiffness of soil and pile and the analysis is done. In Direct method both soil and structure are integrated in a single model with the help of finite element. The modelling of SSI can be done by Beam on Winkler foundation (BWF), where soil elements are modelled as discrete non-linear springs as per API (2008). BWF combines the Near field and Far-field behaviour through a series of

springs. The idealisation of soil using one dimensional uncoupled soil springs however may not be the best possible solution for addressing SSI. A three dimensional continuum model is certainly a better choice for dynamic analysis of SSI system. However, the introduction of continuum soil model for large structural system is practically not feasible due to increase in degree of freedom of the system. Hetenyi *et al.* (1946) demonstrated that the error caused by using the Winkler model and elastic continuum model is very small for realistic scenarios involving flexible beams. So, the approach of considering the soil springs to represent the soil modelling may be considered as acceptable.

Zerva *et al.* (2002) studied the estimation of coherency from the recorded data and discussed on its interpretation. Some empirical and semi-empirical coherency models based on the recorded data, their validity and limitations and the effect of coherency on the seismic response of extended structures has also been studied by them.

In the case of a simply supported bridges, asynchronous ground motion can excite the two pier supports of the same span of the bridge with a difference in time of arrival, resulting in unequal and not in phase support movement. This may in turn result in large difference in displacements along the traffic direction of the bridge between two supporting piers leading to unseating of girder from the bearing which was seen during the 1995 Kobe earthquake [Burdette *et al*. (2008)]. In the lateral direction, this simply supported bridge acts as a continuous one and a significant increase in the bending moments at the base of piers were reported by Lupoi *et al*. (2005) for synchronous *vs* asynchronous motion.

Lavorato *et al.* (2017) studied the nonsynchronous seismic ground motion generated at different foundation point of a long span bridge structure. The recorded seismic ground motion was available at two different points at 422m apart. They have used two different procedures to generate asynchronous seismic ground motions at various points using general coherence model. In first procedure, they generated asynchronous ground motions at the foundation points from the recorded data. In second procedure, they generated the ground movement at the rock level by the method of deconvolution using the recorded surface ground motion. Using first procedure they generated the rock level ground motion at various points below the foundations which then by the method of convolution brought

back to the surface ground motion. The method of deconvolution and convolution/ amplification needs soil parameters like damping ratio and shear wave velocity through which wave propagates. The data generated through these two procedures were compared and studied by them.

Basu *et al.* (2017) developed a framework which accounts for both phase variability and amplitude variability of spatially varying ground motion. For the purpose of assessment, a definition of target spectrum based on the direction of arrival was explored. The effect of choice of coherency model on the simulated spatially varying ground motion was investigated.

Seismic response analysis of structures subject to multi-support excitation has been carried out by various methods like modal analysis [Berrah, (1993)], modified response spectrum method [Kiureghian and Neuenhofer, (1992)], random vibration analysis [Zhang *et al*. (2009)], Monte Carlo simulation [Mirzabozorg *et al*. (2013)], modal analysis using Ritz vectors [Balamonica *et al*. (2015)] etc.

Balamonica *et al.* (2020) used deterministic approach using proper orthogonal decomposition vector (POD) or proper orthogonal mode to analyse response of the structure subject multi support excitation. POD is sometimes termed as principal component analysis (PCA). The difference in vertical movement of mid span between synchronous and asynchronous ground motion has been obtained by them. The difference in rotational movement of mid span between synchronous and asynchronous ground motion has also been obtained by them. Logically the mid span vertical deflection and the flexural rotation was found higher in asynchronous motion compared to synchronous one.

2.4. Vehicle Bridge Interaction (VBI) and Tuned Mass Damper (TMD)

The design of bridges are done following the guideline of various codes and standards which generally considers the vehicular load as equivalent static load instead of dynamic load. This assumption simplifies the design procedure, however it does not include the actual dynamic response of the superstructure. Studies have been done on road bridges considering basic dynamic analysis adopting simplified models of beams and the vehicles done by Inbanthan *et al*. (1987) and Gree *et al*. (1997). Adopting Vehicle bridge interaction

(VBI) for railway bridges were first started by Fryba *et al*. (1996), Delgado *et al*. (1997) and later it was done by Zhang *et al*. (2003), Zambrano *et al*. (2008) and Salcher *et al*. (2019). The actual dynamic analysis considering VBI gives the high deflection response of the superstructure which is generally taken care in the design by enhancing the strength of superstructure. However, it has been found from established theory that the use of energy dissipation devices may reduce the dynamic response considerably when the structure goes into resonance, ie when the external force frequency matches with the fundamental frequency of the superstructure in vertical direction. The proponent of energy dissipation device to reduce the dynamic response was Frahm (1909). Amongst the passive energy dissipation devices, most widely used device are Tuned Mass damper (TMD). The use of vibration absorber by means of passive energy dissipation devices like viscous fluid dampers, viscoelastic dampers, friction damper, metallic yield dampers has been discussed in detail in the paper of Soong *et al.* (1997).

The basic concept of TMD is given in Chopra (1995). The attached system in the Fig. 2.1 and the corresponding governing equations (Eq. 2.1 to Eq. 2.3) show that, if external frequency ω matches with frequency of the main system of mass m_1, which is $\sqrt{k_1/m_1}$, then without the secondary mass m_2, resonance will occur. However, with the secondary mass and the spring, the movement of the main mass m_1 can be brought to near zero, as the secondary mass is producing exactly same force to m_1 but in opposite direction as per Eq. 2.4. The value of the mass will depend on how much the deflection of the secondary mass is allowed.

$$\omega_1^* = \sqrt{k_1/m_1};\ \omega_2^* = \sqrt{k_2/m_2};\ \mu = m_2/m_1 \tag{2.1}$$

$$u_{10} = \frac{p_0}{k_1}.\frac{1-(\omega/\omega_2^*)^2}{[1+\mu(\omega_2^*/\omega_1^*)^2-(\omega/\omega_1^*)^2][1-(\omega/\omega_2^*)^2]-\mu(\omega_2^*/\omega_1^*)^2} \tag{2.2}$$

$$u_{20} = \frac{p_0}{k_1}.\frac{1}{[1+\mu(\omega_2^*/\omega_1^*)^2-(\omega/\omega_1^*)^2][1-(\omega/\omega_2^*)^2]-\mu(\omega_2^*/\omega_1^*)^2} \tag{2.3}$$

$$u_{20} = -\frac{p_0}{k_2};\ k_2.u_{20} = -p_0 \tag{2.4}$$

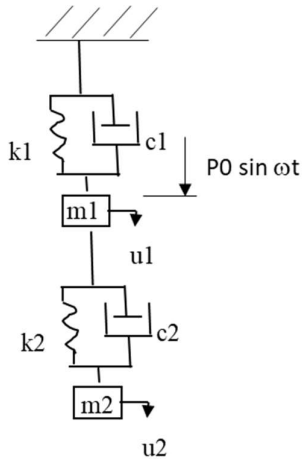

Fig. 2.1. Vibration absorber m_2 attached to a SDF system m_1

Kwon *et al*. (1998) used a 3x40m span continuous RCC box superstructure with TGV high speed train to study the effect of TMD. They considered a moving mass model of 2 DOF system in vertical direction consisting of wheel and body. Single TMD was applied at the middle of the central span of the model. They found that the TMD can reduce the vehicle induced displacement response at midspan of the structure.

Wang *et al*. (2003) worked on vibration suppression in high-speed railway bridges using tuned mass dampers. A railway bridge was modelled as a Euler–Bernouli beam. To simulate the train, series of moving forces, moving masses or moving suspension masses were considered. The resonance occurred once the train load frequency matches with the fundamental frequency of the bridge. A single TMD system was then designed to alter the bridge dynamic characteristics to reduce the vehicle induced vibration. Simply supported bridges of Taiwan High-Speed Railway (THSR) under German I.C.E., Japanese S.K.S. and French T.G.V. trains was modelled and the results showed that the proposed TMD is a useful vibration control device in reducing vehicle induced vibration response like acceleration and displacement.

Li *et al.* (2005) worked on vibration control of railway bridges under high-speed trains using multiple tuned mass dampers (MTMD). The bridges are of 15m and 30m concrete box girder. Optimisation has been done to get the effectiveness of MTMDs on reducing the vehicle induced vibration at resonance. The results showed that the use of the MTMD could

reduce the displacement and acceleration responses of railway bridges significantly at the resonance speed.

Jianzihong *et al*. (2005) worked on vibration control of railway bridge under high speed train using MTMD. They considered two RCC box girder bridge of 15m and 30m span. The vehicle considered by them was having minimum wheel spacing of 2.5m and maximum wheel spacing of 15m. They got significant reduction in the vehicle induced vibration response by using MTMD under resonance condition, ie under condition when the frequency of occurrence of load matches with the fundamental frequency of the structure in vertical direction.

Heydar (2015) studied vibration control of a high speed railway bridge using single TMD and MTMD in his Master's degree thesis work. In his study he considered one existing railway bridge of 40m span, composite ballasted girder and performed FEA of the bridge to understand the train induced vibration. The vertical acceleration due to train induced vibration exceeded the permissible limit of 3.5 m/s^2 for a speed range of 220-240 kmph. He studied the bridge with single TMD attached at mid span and with five parallel TMD uniformly spreaded on the span to get the extent of reduction in vibration. He plotted the train induced vibration response (midspan acceleration and displacment). Through the graph he showed that over a speed range close to the specific speed where the train induced vibration response is maximum under no TMD condition, the effect of TMD is maximum. At the specific speed where the response is maximum under no TMD condition, the reduction of response is maximum. At other speeds beyond the speed range referred above, the effect of TMD is significantly low and in some cases it was negative.

Kahya *et al*. (2017) used series TMD in a simply supported beam to suppress high displacement due to closeness with resonant frequency. High speed train was considered as vehicular load. They studied the effect of series multiple tuned mass dampers (STMDs) on the vehicle induced vibration during resonance. A STMD device consisting of two spring-mass-damper units connected each other in series was installed on the bridge. The bridge was modelled as a simply-supported Euler-Bernoulli beam with constant cross-section. The vehicle was simulated as a series of moving forces with constant speed. The

midspan deflection has been considered as the objective function for optimisation. The results showed that STMDs are effective in bridge vibration suppression.

Miguel et al. (2021) used a 1x17m span, 10m wide, RCC road bridge for optimisation of multiple tuned mass dampers (MTMD) taking into account VBI, random pavement roughness and uncertainties. They use a single tuned mass damper placed at the centre spam of the model, and 3 TMD uniformly spreaded near the midspan. They have shown that reduction in vertical response using TMD is about 50%. The effect of sigle TMD and MTMD are almost similar.

2.5. Concluding Remarks

From the above review in respect of Response reduction factor, following points may be concluded:

- The three of the papers suggested two contradictory conclusion. One suggests that the *R* obtained for bridge piers are in higher side than that suggested in Eurocode 8 and AASHTO. Other paper suggested that *R* obtained for framed structure designed as per Indian standards are less than that of suggested values in IS codes. This needs a wider range of study to conclude and suggest the necessary changes in the various standards.
- Vast amount of study has been done on inelastic spectra considering various EQ occurred in the past but in evaluation of equivalent value of *R* for bridge structure is still need focus.
- The hollow RCC section so far studied have small dimensions like 400mm square or 800mm diameter with wall thickness between 100mm to 250mm.
- Assessment of *R* or *q* factor for RCC large diameter hollow circular tall piers section and particularly the effect of special confining reinforcement in the section and how the same improves the ductility of the bridge needs further focus.
- Effect of opening in the hollow circular section on R has not been studied by any researcher. As inspection opening is essential in the tall piers, this study is extremely important.

- Stress strain curve for concrete is available of solid circular or rectangular section. Application of the same on hollow circular section needs special focus.

In line with the above findings, it is apparent that more study is needed to understand the value of response reduction factor *R* for large diameter hollow circular pier. The stress strain relation of concrete for solid rectangular and circular section is available. However, the use of this relation in hollow circular section needs some special study so that the same can be used for generation of *R* for large diameter hollow circular section. The value of *R* recommended in various codes and standards are single valued which does not show the relation of *R* with respect to various depending parameters. This unique value of *R* may cause over safe design in some cases or inadequate design in some other cases. The inspection opening is essential in tall piers and thus the study of effect of the opening on the value of R is extremely important. With this focus in mind the present study on *R* of large hollow circular section has been done.

In reference to the literature review in connection with Asynchronous motion, it was found that there are adequate studies available on relative effect of synchronous and asynchronous ground motion on bridge structures using soil structure interaction and adopting asynchronous motion from various coherence model. However little study is available on relative effect of synchronous and asynchronous ground motion on tall railway bridge movement at the superstructure level. The deflection of track during transverse seismic is important in view of the safe train movement and as such no study is available so far on this. With this focus in mind, the present study on asynchronous motion and its effect on response of tall railway bridges has been undertaken.

In reference to the literature review in connection with VBI and TMD, it is found that the dynamic analysis of railway bridges and the effect of TMD in reducing the vehicle induced vibration of superstructure has been done by many researchers but most of them are related to small span ballasted superstructure of RCC construction where the mass of the structure is high. However, the similar analysis of vibration control using TMD considering VBI model for long span OWG of steel construction having light mass has not been done yet.

With this focus in mind the present study has been undertaken to understand the effect of TMD in train induced vibration control for long span steel OWG bridges.

Chapter 3

Response reduction factor of large hollow circular section

3.1. Introduction

The seismic behaviour of hollow circular section has been studied by various authors. However, the effect of various parameters on large diameter hollow circular section with or without opening has not been studied yet. Thus, the aim of this work is to do the estimation of response reduction factor R of tall pier having large hollow circular section. Parametric study has been done and has been shown how the value of R varies with axial load (P/Af_{ck}), main steel ratio (ρ_{cc}), transverse steel ratio (ρ_s), spacing of transverse steel (S_h), grade of concrete (f_{ck}) and grade of steel (f_y). Study has been done for varying outer diameter of hollow pier between 4m and 16m and varying wall thickness between 0.5m and 2m. In practice, door opening is needed for inspection purpose of the piers. Effect of such opening in the section varying between 0 and 16 degree (opening size subtending angle at the centre of the pier) has also been considered. Recommended value of R for hollow circular section of diameter 4m to 16m, grade of concrete M40 and reinforcement steel with grade Fe 500 has been presented for various values of ρ_s, P/Af_{ck} and ρ_{cc}.

3.2. Methodology adopted

Moment-curvature relationship (M-ϕ curve) for hollow circular section with prescribed stress-strain relationship of concrete and reinforcement steel has been generated for different size of the section. Concrete stress-strain relation has been adopted from the model given in Mander *et al.* (1988) as this model is based on experimental results of both circular and rectangular section behaviour. It also considers both enhancement of strength and ductility due to confinement of concrete. Caltrans (2013) uses this model of stress strain of concrete to obtain available ductility in confined concrete under seismic load.

Expression for Confinement effective coefficient (k_e) is given in Mander *et al.* (1988) for both circular and rectangular solid section. Based on this model, value of the k_e for hollow circular section has been proposed and adopted in the present study.

Ultimate strain in concrete has been estimated from strain energy balance approach of the concrete section at which first fracture occurs at confining steels as suggested in Mander *et al.* (1988). This is also compared with other established simplified formulae of ultimate concrete longitudinal strain given by Priestly *et al*. (1996) and Wei and Wu (2014). The basic concept of the approach of Mander *et al.* (1988) is that the additional ductility in concrete section under confinement is due to the energy stored in the transverse reinforcement. Thus, the value primarily depends on the transverse reinforcement ratio. The other factors on which this value depends are percentage of main steel, grade of concrete and grade of steel.

From the M-ϕ curve, yield curvature and ultimate curvature have been obtained, from which curvature ductility and deflection ductility values have been calculated by directly calculating the area under the curve and the moment of the area about the cantilever end of a cantilever pier. This has been done instead of calculating ductility of the section from average length of plastic hinge as because under axial load, the M-ϕ relation is not linear even up to the yielding of tension steel unlike section with no axial load. Initially when moment is less, effect of axial load is predominant and the non-linearity prevails. With higher value of moment, the graph becomes linear. The effect has been discussed in detail in section 3.4.6.

The deflection calculation at the cantilever tip of the pier under consideration has been done with respect to the cracked moment of inertia of section. However, the section in between two cracked section will have un-cracked moment of inertia and concrete will impart some stiffening effect. The effect of the same has been studied by using effective moment of inertia. Established formula of effective moment of inertia which is a function of cracked and gross moment of inertia and actual moment on the section has been considered for this purpose.

Reserve strength factor has been introduced which is estimated from the ratio of yield moment, i.e. where the extreme main bar yields, to the working moment, i.e. where the extreme main bar is having 0.55 times yield stress (Refer Note 1 of Table 22, IS 456, 2000). The value of reserve strength factor has been found ranging between 1.16 to 1.54 depending on the main steel ratio and axial load on the section.

While estimating ultimate curvature and corresponding ultimate moment, contribution of moment due to *P-Δ* effect has been considered. For this purpose, appropriate C/G of load is used. Superstructure C/G is considered at top of pier and substructure C/G is considered at mid height of the pier. Deflection at mid height is considered half of the top deflection. The period of vibration of the structure and effect of post yield stiffness is estimated considering this *P-Δ* effect. The structure under consideration for the present study has slenderness ratio less than 50, and it is found that corresponding to the ultimate curvature of the section capacity, this post yield stiffness is non-negative. In case the slenderness ratio is more than 50, the ultimate curvature capacity of the section may lead to negative post yield stiffness and thus *R* value shall be less as the same is to be obtained from less ultimate curvature value in order to avoid negative stiffness effect.

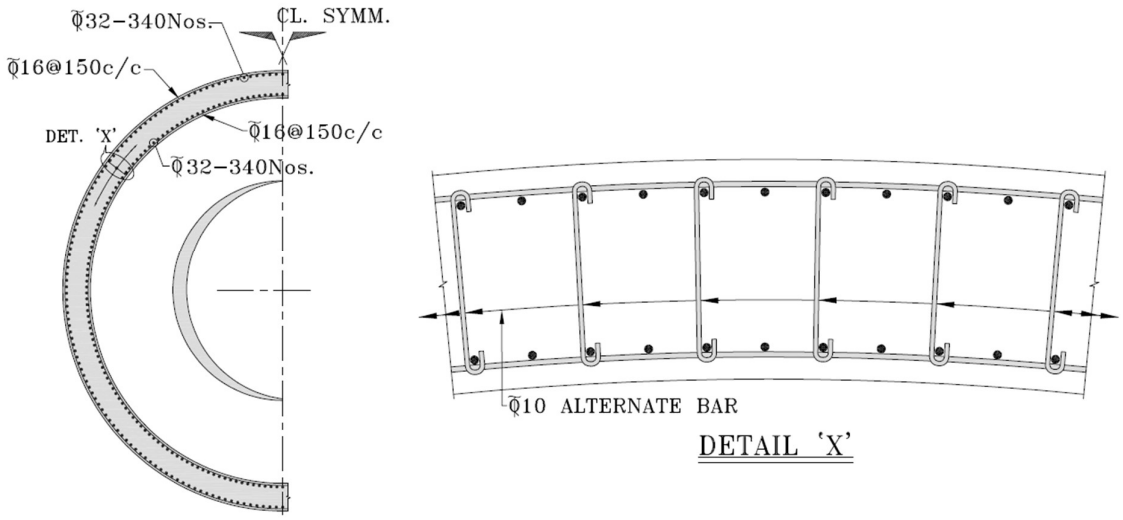

Fig. 3.1. Configuration of the hollow circular section used for analysis showing outer and inner row of main steel, outer and inner circular transverse steel and transverse ties connecting the main bars.

As per established theory, yield reduction factor value is same as deflection ductility when the natural period of the structure is high. Thus, response reduction factor has been calculated by multiplying deflection ductility with reserve strength factor.

3.3. Example problems considered

A 141m tall pier with outer diameter (D_o) 16m, inner diameter (D_i) 14m, i.e. wall thickness of 1m and confining width of 0.85m, grade of concrete M40 and grade of steel f_y = 500MPa with f_{su} = 700MPa has been studied for various transverse steel ratio (ρ_s), main steel ratio (ρ_{cc}) and axial load (P/Af_{ck}). Standard value of stirrup spacing of 100mm has been considered as recommended for special confining zone in different codes/ guidelines.

Three different $P/A\,f_{ck}$ values (0.1, 0.2 & 0.3), four different ρ_{cc} values (1%, 2%, 3% & 4%) and five different ρ_s values (0.2%, 0.4%, 0.6%, 0.8% & 1%) have been considered. Thus, total 3x4x5 = 60 analyses have been done to get value of R for different parameters. Fig. 3.1 shows the actual configuration of hollow circular section that has been used for analysis.

In addition to outer diameter of section 16m and wall thickness 1m, three more wall thicknesses of 0.5m, 1.5m and 2.0m have been considered to understand the effect of confining effective width on R. In practice, generally hollow pier starts with 4m diameter with 500mm wall thickness. Pier diameter less than 4m is preferably made solid to avoid maintenance of inner surface of the pier, but with diameter 4m or above hollow section is preferable to reduce mass of the structure. Study has also been done to understand the value of R for pier diameter 4m. Further a section size of outer diameter 10m has also been considered, where wall thicknesses are 0.5m, 1.0m and 1.5m and ρ_s = 0.6%, ρ_{cc} = 1%, P/Af_{ck} = 0.1 to understand the effect of effective confining coefficient. Thus, the value of R recommended in this study is valid for section diameter varying between 4m and 16m with wall thickness varying between 0.5m and 2.0m.

Door opening is needed for inspection purpose of the hollow piers. Generally, the size of door opening varies between 1m to 2m depending on the diameter of the pier. The angular dimension of opening may vary from 8 degree in large diameter pier to 16 degree in small diameter pier, where the angle is measured by the size of opening subtending to the centre

of the circle. The value of *R* has been studied for this angular dimension of opening in the section sizes described earlier.

Effect of grade of steel on *R* has been studied with Fe 500 and tensile strength (*TS*) or ultimate strength as 700MPa. Effect of grade of concrete has been studied considering M40 grade.

3.4. Considerations for evaluation of R

3.4.1. Concrete stress-strain characteristic

Various models of stress-strain relation of concrete are available. Some of the popular models that has been discussed here are by Kent and Park (1971), Mander *et al.* (1988), Saatcioglu *et al.* (1992), Cusson *et al.* (1995) and Hoshikuma *et al.* (1997).

The stress-strain relation of concrete proposed by Kent & Park (1971) was developed for maximum grade of concrete up to M55. This curve proposes no enhancement of strength with the confinement of concrete but enhancement in strain capacity which depends on transverse steel ratio (ρ_s), confinement width measured to outside of hoops (b'') and spacing of stirrup (s_h). This enhancement is estimated from the shift of strain capacity at 50% of yield strength after yield (ε_{50h}), which is a function of transverse confining reinforcement ratio, width of confinement and spacing of reinforcement.

The model considers that the maximum strain at which the strength of concrete is achieved (ε_{co}) is at 0.002. Fig. 3.2 shows the stress-strain graph based on this model corresponding to the parameters b''=0.85m, s_h =0.1m and different values of ρ_s.

Rising branch AB:

$$f_c = f'_c\left[\frac{2\varepsilon_c}{.002} - \left(\frac{\varepsilon_c}{.002}\right)^2\right] \tag{3.1}$$

Falling branch BC:

$$f_c = f'_c[1 - Z(\varepsilon_c - .002)] \tag{3.2}$$

$$\text{Region CD: } f_c = 0.2f'_c \tag{3.3}$$

Where,

$$Z = \frac{0.5}{\varepsilon_{50u}+\varepsilon_{50h}-.002}; \tag{3.4}$$

$$\varepsilon_{50u} = \frac{3+.002 f_c'.}{f_c'-1000} \tag{3.5}$$

and horizontal shift of strain

$$\varepsilon_{50h} = \frac{3}{4}.\rho_s\sqrt{\frac{b''}{sh}} \tag{3.6}$$

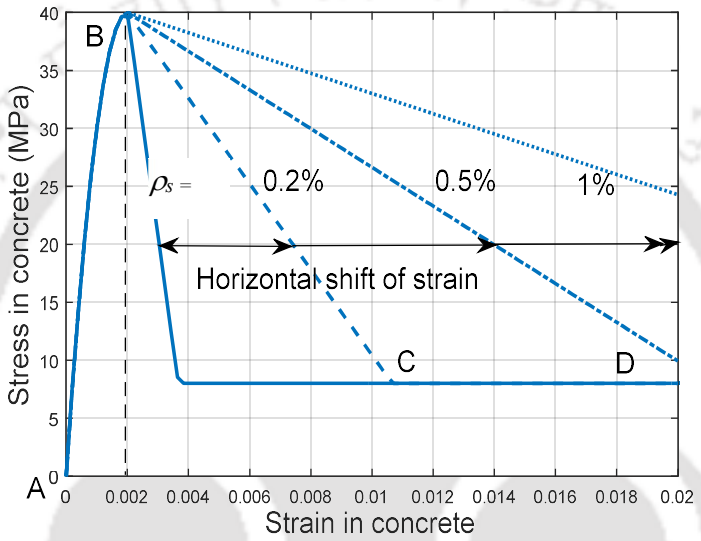

Fig. 3.2. Stress-strain curve of concrete for different ρ_s as per Kent & Park (1971)

Stress-strain relation by Mander *et al.* (1988) is based on both circular and rectangular section. Both enhancement of strength and ductility is proposed in the model. Stress-strain relation depends on ρ_s, S_h, d_s, fy, ρ_{cc}, Ec or f_{ck}. Fig. 3.3 shows the stress-strain graph based on this model corresponding to the parameters $\rho_s = 1\%$, $S_h = 0.1$m, $d_s = 0.85$m, $fy = 500$MPa, $\rho_{cc} = 1\%$, $f_{ck} = 40$MPa and the same graph for unconfined concrete.

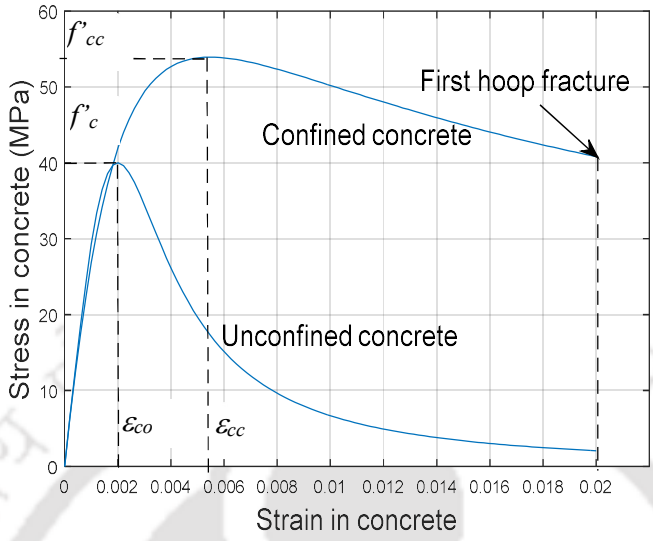

Fig. 3.3. Stress-strain relation of concrete as per Mander *et al.* (1988)

$$f'_{cc} = f'_c[-1.254 + 2.254\sqrt{1 + \frac{7.94f'_l}{f'_c}} - \frac{2f'_l}{f'_c}] \tag{3.7}$$

$$f'_l = \frac{1}{2}.k_e\rho_s f_{yh}; \text{ where } k_e = \frac{\left(1-\frac{s'}{2d_s}\right)^2}{1-\rho_{cc}} \tag{3.8}$$

$$\varepsilon_{cc} = \varepsilon_{co}[1 + 5\left(\frac{f'cc}{f'c} - 1\right)] \tag{3.9}$$

$$f_c = f'_{cc}\frac{n\left(\frac{\varepsilon_c}{\varepsilon_{cc}}\right)}{(n-1) + \left(\frac{\varepsilon_c}{\varepsilon_{cc}}\right)^n} \tag{3.10}$$

$$n = \frac{E_c}{E_c - E_{sec}}; \tag{3.11}$$

$$E_c = 5000\sqrt{f'_c} \tag{3.12}$$

$$E_{sec} = \frac{f'cc}{\varepsilon_{cc}} \tag{3.13}$$

Stress-strain relation by Saatcioglu *et al.* (1992) is based on the effect of confining reinforcement on circular, square and rectangular section of concrete grade varying between M20 to M32. This curve proposes enhancement of strength up to 65% in addition to the enhancement in strain capacity. Both the enhancement of strength (f'_{cc}) and corresponding strain capacity (ε_{cc}) is given in terms of volumetric ratio of transverse

reinforcement (ρ_s), strength (f'_c) and corresponding strain capacity (ε_{c0}) of the unconfined concrete. The strength capacity after yield is given by the strain against 85% of the yield strength (ε_{85}) which is a function of ρ_s, ε_l and strain corresponding to 85% strength after yield of unconfined concrete (ε_{085}) which is considered as 0.0038 in absence of any other experimental result. The falling branch of the graph is a straight line. Fig. 3.4 shows the stress-strain graph based on this model corresponding to the parameters ρ_s =1%, S_h =0.1m, d_s = 0.85m, fy = 500MPa, ρ_{cc} = 1%, f_{ck} = 40MPa and the corresponding graph for unconfined concrete.

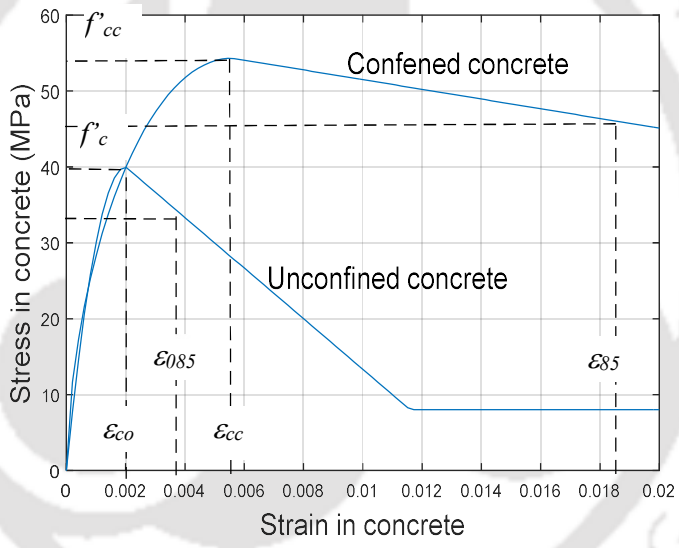

Fig. 3.4. Stress-strain relation of concrete as per Saatcioglu *et al.* (1992)

$$f'_{cc} = f'_c + k_1 f_l \tag{3.14}$$

$$k_1 = 6.7 f_l^{-0.17} \tag{3.15}$$

$$f_l = \frac{1}{2} \cdot \rho_s f_{yh} \tag{3.16}$$

$$\varepsilon_{cc} = \varepsilon_{co}[1 + 5K] \tag{3.17}$$

$$K = \frac{k_1 f_l}{k_e f'_c} \tag{3.18}$$

Ascending curve:

$$f_c = f'_{cc}\left[\frac{2\varepsilon_c}{\varepsilon_{co}} - \left(\frac{\varepsilon_c}{\varepsilon_{co}}\right)^2\right]^n \quad (3.19)$$

$$n = \frac{1}{1+2K} \quad (3.20)$$

$$\varepsilon_{85} = 260\rho_s\varepsilon_{cc} + \varepsilon_{085} \quad (3.21)$$

$$\varepsilon_{085} = 0.0038 \quad (3.22)$$

Falling branch is a straight line passes through the point (ε_{c50c}, 0.5 f'_{cc}).

Stress-strain relation by Cusson *et al.* (1995) is based on the effect of confining reinforcement on square section of high-grade concrete varying between M60 to M120. The descending curve follows an exponential pattern. This descending curve is obtained from the strain against 50% of the yield strength (ε_{C50C}) which is a function of ρ_s, strength of unconfined concrete and ε_{C50U} which is considered as 0.004 in absence of any other experimental data. Fig. 3.5 shows the stress-strain graph based on this model corresponding to the parameters ρ_s =1%, S_h =0.1m, d_s = 0.85m, fy = 500MPa, ρ_{cc} = 1%, f_{ck} = 40MPa and the corresponding graph for unconfined concrete.

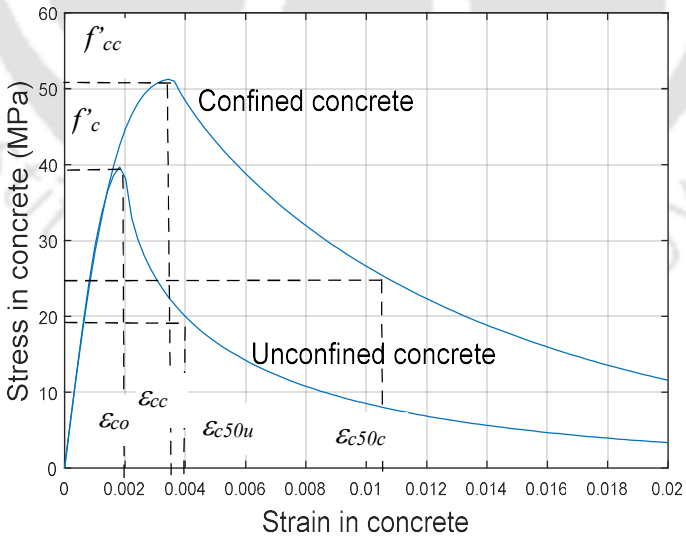

Fig. 3.5. Stress-strain relation of concrete as per Cusson *et al.* (1995)

$$f'_{cc} = f'_c[1.0 + 2.1\left(\frac{f'_l}{f'_c}\right)^{0.7}] \tag{3.23}$$

$$\varepsilon_{cc} = \varepsilon_{c0} + 0.21\left(\frac{f'_l}{f'_c}\right)^{1.7} \tag{3.24}$$

$$f'_l = \frac{1}{2}.k_e\rho_s f_{yh} \tag{3.25}$$

$$k_e = \frac{\left(1 - \frac{s'}{2d_s}\right)^2}{1 - \rho_{cc}} \tag{3.26}$$

Ascending curve:

$$f_c = f'_{cc}\frac{n\left(\frac{\varepsilon_c}{\varepsilon_{cc}}\right)}{(n-1)+\left(\frac{\varepsilon_c}{\varepsilon_{cc}}\right)^n} \tag{3.27}$$

$$n = \frac{E_c}{E_c - E_{sec}} \tag{3.28}$$

$$E_{sec} = \frac{f'_{cc}}{\varepsilon_{cc}} \tag{3.29}$$

Descending curve:

$$f_c = f'_{cc}\exp[k1.(\varepsilon_c - \varepsilon_{cc})^{k2}] \tag{3.30}$$

$$k1 = \frac{ln0.5}{(\varepsilon_{c50c} - \varepsilon_{cc})^{k2}}; \tag{3.31}$$

$$k2 = 0.58 + 16\left(\frac{f'_l}{f'_c}\right)^{1.4} \tag{3.32}$$

$$\varepsilon_{c50c} = \varepsilon_{c50u} + 0.15\left(\frac{f'_l}{f'_c}\right)^{1.1} \tag{3.33}$$

In absence of any experimental data,

$$\varepsilon_{c50u} = .004 \tag{3.34}$$

Stress-strain relation by Hoshikuma *et al*. (1997) is different for circular and rectangular section.

For circular section:

$$f'_{cc} = f'_c\left(1 + \frac{3.83\rho_s f_{yh}}{f'_c}\right) \tag{3.35}$$

$$\varepsilon_{cc} = 0.00218 + \frac{0.0332\rho_s f_{yh}}{f'_c} \tag{3.36}$$

For rectangular section:

$$f'_{cc} = f'_c\left(1 + \frac{0.73\rho_s f_{yh}}{f'_c}\right) \tag{3.37}$$

$$\varepsilon_{cc} = 0.00245 + \frac{0.0122\rho_s f_{yh}}{f'_c} \tag{3.38}$$

All the above stress-strain relations are based on few common features. The concrete stress-strain relation shows the strength of unconfined concrete (f'_c) reaches at a strain (ε_{co}) value and the stress falls beyond this strain. The enhanced strength of confined concrete (f'_{cc}) depends on the transverse steel ratio (ρ_s) and the effective confinement coefficient (k_e) which in turn depends on size of the section (b'') and the spacing of transverse steel (S_h). This enhanced strength corresponds to an enhanced strain value (ε_{cc}) which is more than ε_{co}.

In the model of Kent and Park (1971) this enhancement of strength has not been considered. The ascending graph is curvilinear and its equation is same for both Kent & Park (1971) and Saatcioglu (1992) and is as originally proposed by Popovics (1973). The falling branch is straight line for both the models. For Mander *et al.* (1988) and Cusson *et al.* (1995), the ascending branch is curvilinear and their equation is also same. For Mander *et al.* (1988) one single equation is valid for the falling branch also whereas for Cusson (1995) different curve has been proposed for falling branch. Effect of spacing of transverse steel (S_h) in the form of effective confinement coefficient (k_e) has been considered in both Mander *et al.* (1988) and Cusson *et al.* (1995). The effect of transverse steel (S_h) has direct effect in the model of Kent & Park (1991). In the model of Hoshikuma *et al.* (1997) the effect of spacing

of transverse steel has been considered by providing separate parameters for circular and rectangular section.

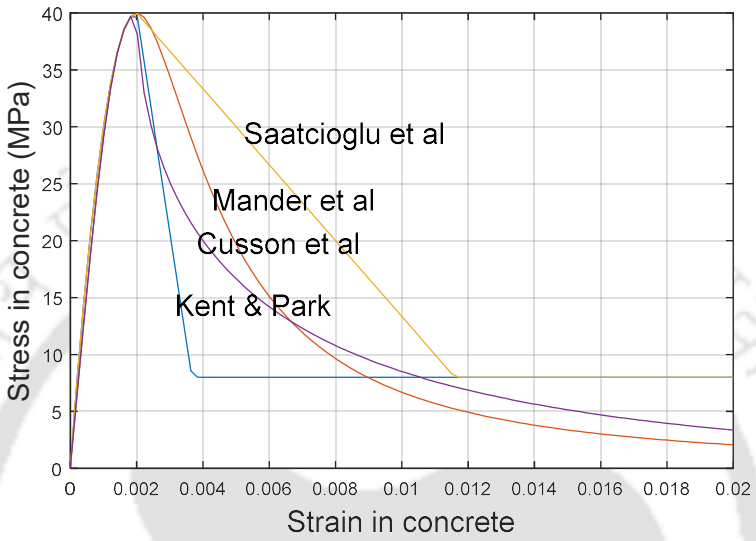

Fig. 3.6. Comparative Stress-strain relation of concrete as per different models (Transverse steel ratio 0% - unconfined)

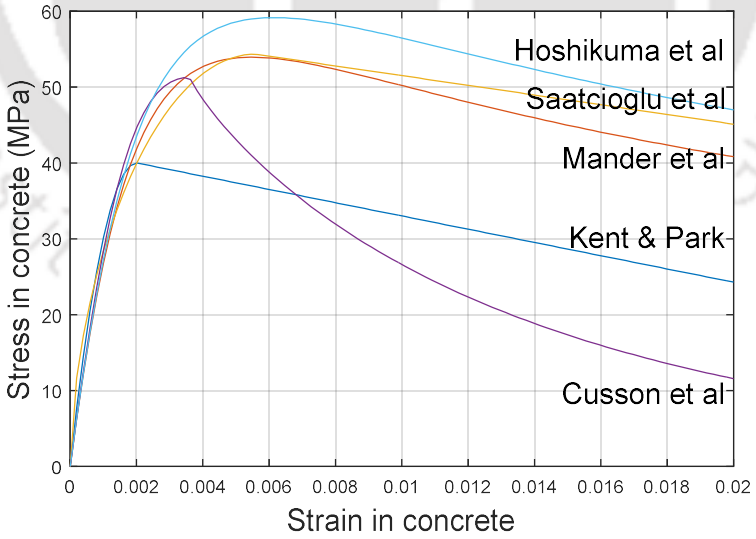

Fig. 3.7. Comparative Stress-strain relation of concrete as per different models (Transverse steel ratio 1%)

Fig. 3.6 and Fig. 3.7 show the comparative stress strain relation of concrete as per all the above models discussed. Fig. 3.6 corresponds to the unconfined concrete and Fig. 3.7 corresponds to transverse steel ratio 1%. From these comparative graphs it is found that the relation given by Mander *et al.* (1988), Saatciouglu *et al.* (1992) and Hoshikuma *et al.* (1997) show results very close to each other. The strength enhancement and corresponding strain in Mander and Saatcioglu are very close whereas that of in Hoshikuma is little higher.

All these three models are based on low grade of concrete and may be considered as applicable for standard concrete grade which means grade of concrete up to M50. In case of high-performance concrete of grade beyond M50 these relations will not be applicable as the ductility of the high-performance concrete is less. As the model given by Cusson *et al.* (1995) is based on high performance concrete of grade between M60 and M120, this curve will be applicable for these higher grades of concrete. In the present study model proposed by Mander *et al.* (1988) has been used as the same is based on both solid rectangular and solid circular concrete section.

Model of Mander *et al.* (1988) is based on circular and rectangular section. While adopting the same model in the hollow circular section the basic assumption is that any small slice of the hollow circular section (Fig. 3.11) is similar in shape of a rectangular section (Fig. 3.10) and thus the applicability of the stress-strain curve in hollow circular section is acceptable. The calculation of transverse steel ratio of rectangular section and hollow circular section also are similar in nature and as the transverse steel is uniformly distributed in the hollow circular section, the overall ratio is representative of any small equivalent rectangular section. Thus, the model of Mander *et al.* (1988) has been assumed to be applicable in hollow circular section similar to its applicability in rectangular section.

In addition to the previous discussion in favour of selecting the model of Mander *et. al.* (1988), the expression of lateral hoop stress (f'_l) for hollow circular section is needed to be established similar to the expression for solid circular section. Eq. 3.8 shows the relation between lateral hoop stress (f'_l) on the confining reinforcements/ transverse steel and ratio of transverse steel (ρ_s), yield stress of transverse steel (f_{yh}) for solid circular section.

A comparative force equilibrium for solid circular section and hollow circular section is shown below:

The relation of lateral confining pressure in concrete (f_l) with the yield stress of transverse steel (f_{yh}) and ratio of transverse steel (ρ_s) in hollow circular section can be established as follows.

From the Fig. 3.7A, the force equilibrium equation can be written as

$$f_l d_s s = 2A_{sp} f_{yh} \quad \text{.....(a)}$$

As the ratio of hoop transverse reinforcement,

$$\rho_s = \frac{2A_{sp}}{d_s s} \quad \text{..... (b)}$$

From Eq. (a) and (b) it can be said that

$$f_l = \rho_s f_{yh}; \text{ ....(c)}$$

Including the term k_e finally it can be written that

$$f'_l = k_e \rho_s f_{yh}; \text{ ....(d)}$$

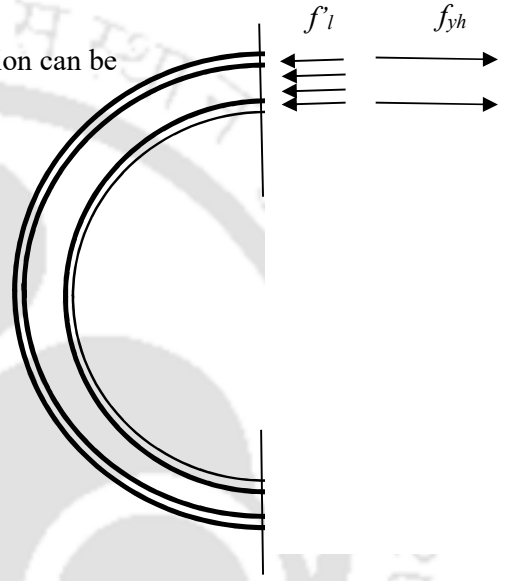

Fig. 3.7A. Force equilibrium diagram for hollow circular pier - relation of f_l with f_{yh} and ρ_s

Comparing Eq. (3.8) and (d), it can be said that the value of f'_l for solid circular section is ½ of that in hollow circular section for the same circumferential hoop transverse steel ratio ρ_s. However, in hollow circular section in addition to the circumferential hoop reinforcement, cross ties connecting the outer layer of main reinforcement with the inner layer of main reinforcement is necessary in order to get effective confinement of concrete. This reinforcement contributes almost same volume of the hoop transverse reinforcement and thus actual transverse steel ratio in hollow circular section is double of the value being used in Eq. (d). Thus, if including the volume of cross ties, the total transverse steel ratio is calculated then, the same Eq. (3.8) which is applicable for solid circular section can be used for hollow circular section also and the same has been considered in the present study.

3.4.2. Stress-strain relation of reinforcement steel

The standard stress-strain graph of steel reinforcement has been obtained as shown in the Fig. 3.8. The strain hardening part CD of the curve is similar to that used by Burns and Siess (1962).

Region AB: $\varepsilon_s \leq \varepsilon_y$,

$$f_s = \varepsilon_s E_s \tag{3.39}$$

Region BC: $\varepsilon_y \leq \varepsilon_s \leq \varepsilon_{sh}$,

$$f_s = f_y \tag{3.40}$$

Region CD: $\varepsilon_{sh} \leq \varepsilon_s \leq \varepsilon_{su}$,

$$f_s = f_y\left[\frac{m(\varepsilon_s-\varepsilon_{sh})+2}{60(\varepsilon_s-\varepsilon_{sh})+2} + \frac{(\varepsilon_s-\varepsilon_{sh})(60-m)}{2(30r+1)^2}\right] \tag{3.41}$$

$$m = \frac{\left(\frac{f_{su}}{f_y}\right)(30r+1)^2 - 60r - 1}{15r^2} \tag{3.42}$$

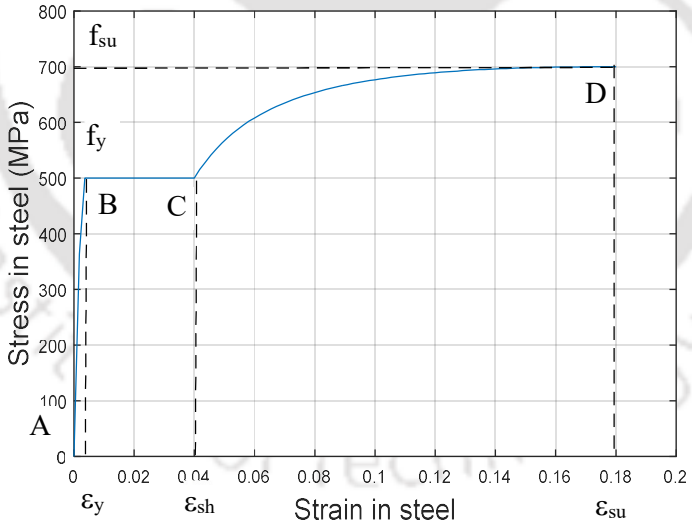

Fig. 3.8. Stress-strain curve of reinforcement steel as per Burns and Siess (1962)

3.4.3. Confinement effective coefficient (k_e)

3.4.3.1. Circular and rectangular section

It is a parameter that is used to find the effective confinement stress on concrete due to confinement steel and is a function of area of core concrete that is effectively confined within the confining steel.

For circular section due to the effect of hoop tension in the transverse steel surrounding the concrete, the entire area within the transverse steel is considered as confined. However, in between two parallel transverse steel, the part of concrete near cover is unconfined as shown in Fig. 3.9. For rectangular section, part of area between two successive main bars are not confined as the straight transverse steel will bend due to lateral pressure. In addition, in between two parallel transverse steel, the part of concrete near cover is unconfined like circular section. The effect is shown in Fig. 3.10.

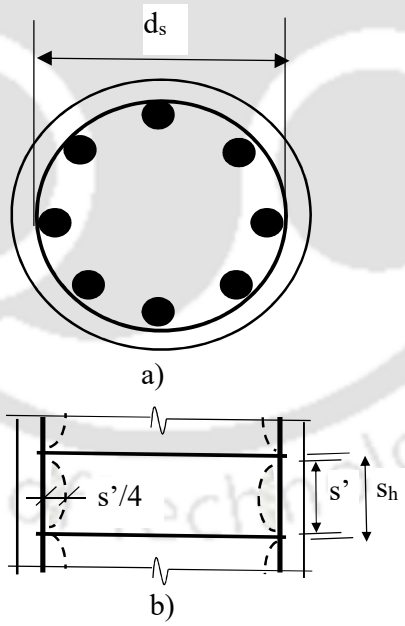

Fig. 3.9. Effect of confinement in circular section: a) Cross section, b) Elevation. Shaded area shows the unconfined zones.

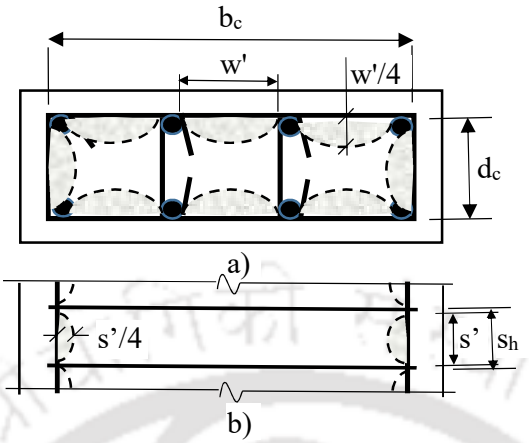

Fig. 3.10. Effect of confinement in rectangular section: a) Cross section, b) Elevation. Shaded area shows the unconfined zones.

Thus, for circular section the effective area of confined concrete is calculated by deducting the unconfined area shown in of Fig. 3.9, b). i.e.

$$A_e = \frac{\pi}{4}.\left(d_s - \frac{s'}{2}\right)^2 = \frac{\pi}{4}d_s^2.\left(1 - \frac{s'}{2d_s}\right)^2 \tag{3.43}$$

Core concrete area:

$$A_{cc} = \frac{\pi}{4}d_s^2.(1-\rho_c) \tag{3.44}$$

Hence the confinement effective coefficient for circular section

$$k_e = \frac{A_e}{A_{cc}} = \frac{\left(1 - \frac{s'}{2d_s}\right)^2}{1-\rho_c} \tag{3.45}$$

For rectangular section the effective area of confined concrete is calculated by deducting the unconfined area shown in of Fig. 3.10, a) & b). i.e.

$$A_e = \left(b_c d_c - \sum_{i=1}^{n} \frac{((w_i'))^2}{6}\right)\left(1 - \frac{s'}{2b_c}\right)\left(1 - \frac{s'}{2d_c}\right) \tag{3.46}$$

$$\text{Core concrete area: } A_{cc} = b_c d_c.(1-\rho_c) \tag{3.47}$$

Hence the confinement effective coefficient for rectangular section

$$k_e = \frac{\left(1-\sum_{i=1}^{n}\frac{\left(w_i'\right)^2}{6b_cd_c}\right)\left(1-\frac{s'}{2b_c}\right)\left(1-\frac{s'}{2d_c}\right)}{1-\rho_c} \tag{3.48}$$

where n is number of unconfined zones as in Fig. 3.10.

3.4.3.2. Hollow circular section

In case of hollow circular section, the behaviour of the transverse steel in confining the concrete is not similar to that of solid circular or rectangular section. Hollow circular sections, as shown in Fig. 3.11 are provided with two layers of transverse steel, one at the outer periphery of the section wall and the other at the inner periphery of the section wall. In addition, cross tie transverse steels are provided to radially tie the outer and inner periphery longitudinal steel. The outer periphery transverse steel is in hoop tension and confines the concrete fully like solid circular section. Inner periphery transverse steel is not necessarily in hoop tension and ignoring the arch action of the bar while under lateral pressure from concrete, the unconfined effect will be similar to rectangular section as shown in Fig. 3.11. Thus, the confinement effective coefficient for hollow circular section may be given as

$$k_e = \frac{\left(1-\sum_{i=1}^{n}\frac{\left(w_i'\right)^2}{6b_cd_c}\right)\left(1-\frac{s'}{2d_c}\right)}{1-\rho_c} \tag{3.49}$$

where n is number of unconfined zones within b_c as in Fig. 3.11.

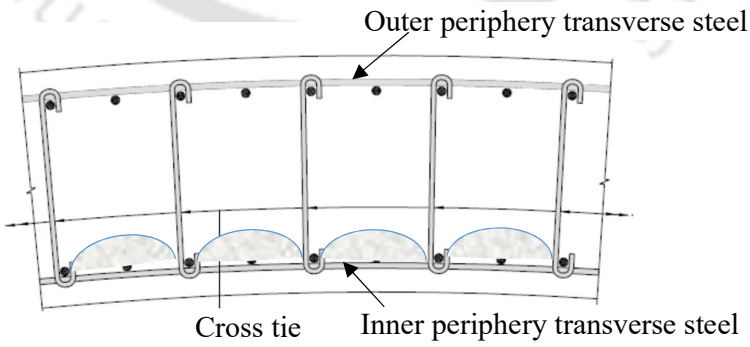

Fig. 3.11. Effect of confinement in hollow circular section

A hollow circular section has been analysed in Abaqus using CDP model of concrete and compared the stress-strain relation generated by the model with the theoretical curve proposed by Mander *et al.* (1988) using the value of k_e as obtained from the formula adopted for hollow circular section and it has been found that there is good closeness of the two. The results obtained in the model studied in Abaqus has been shown in Section 3.4.4. This suggests that the formula adopted is acceptable.

With the above consideration if the value of k_e is calculated for both solid circular section and hollow circular section, it has been found that if main steel percentage, spacing of transverse steel are same for both the sections, and the spacing of main steel for the hollow circular section is in the range of 150mm, with the core width of the wall of the hollow circular section same as the core width of the solid circular section, the values of k_e are close to each other with the value being little higher for hollow circular one. For example, with 1m thick wall of hollow circular section and 1m diameter solid circular section, with 100mm spacing and 16mm diameter of transverse steel, 1% main steel, 75mm clear cover, the value of k_e for solid circular section is 0.91 and that of for hollow circular section is to the tune of 0.93. This closeness reduces as the width of the wall and the diameter of the circular section reduces. With 500mm thick wall for hollow section and 500mm diameter solid section, the value is 0.77 for solid circular section and 0.84 for hollow circular section. Hence although the value of k_e can be calculated for hollow circular section applying the Eq. 3.49, the value is calculated from solid circular section as it gives similar result and remains in safer side.

3.4.4. Authentication of proposed k_e of circular hollow section through FEA

Three-Dimensional Non-Linear Finite Element Analysis of concrete columns confined with transverse and longitudinal reinforcement under concentric axial compressive loading have been carried out utilizing the general-purpose finite element software Abaqus/CAE 2021.

A set of concrete columns having different cross-section were analysed for evaluation of column behaviours under uniform compression. The effects of confining pressure from varying transverse reinforcement ratios have been studied in details on stress-strain

behaviours of unconfined and confined concrete along with radial stress variations in columns with different cross-sections.

3.4.4.1 Material Models in Abaqus

Reinforced concrete is a complicated material to be modelled within finite element framework. A proper material model is required in order to be capable of representing both elastic and plastic behavior of concrete in both compression and tension. The complete compressive behavior should include both elastic and inelastic behavior of concrete including the strain softening regimes. Simulation of entire behavior under tension should include tension softening, tension stiffening and local bond effects in concrete elements.

Concrete Damaged Plasticity model [Abaqus, 2018] provides a general capability for modelling concrete in all types of RC structures. It uses the concepts of isotropic damaged elasticity in combination with isotropic tensile and compression plasticity to represent the inelastic behavior of concrete. It is intended primarily for the analysis of reinforced concrete structures, but can also be used for plain concrete.

Application extends to monotonic, cyclic, and dynamic loading under low confining pressures. It consists of the combination of non-associated multi-hardening plasticity and scalar (isotropic) damaged elasticity to describe the irreversible damage that occurs during fracture under compressive loading. It is susceptible to application of strain rate, and precautions must be measured and evaluated before evaluating a comparative study. This model is a continuum, plasticity-based, damage model for concrete. It assumes two main failure mechanisms, cracking under tension loading while crushing of concrete under compression loading. The evolution of yield surface which in terms is the failure surface is controlled with two hardening variables [Abaqus, 2018], $\varepsilon_t^{\sim pl}$under tension and $\varepsilon_c^{\sim pl}$ under compression. The advantage of CDP model is based on its parameters, which have an explicit physical interpretation. The following table contains the default values provided by Abaqus in the material definition.

Concrete strength under uniaxial compression or tension, differs radically from the one determined with complex states of stress, as concrete under biaxial compression reaches

higher strength between ten to twenty percent higher than its uniaxial state while in the hydro-static state (uniform triaxial compression) its strength is theoretically undefined.

Table 3.1. Concrete Damage Plasticity Parameters for FE Analysis

Parameters	Dilation angle	Eccentricity	$\frac{f_{bo}}{f_{co}}$	K_C	Viscosity
Values	32	0.1	1.16	0.66	0.0001

- Dilation angle**:** Inclination angle of the failure surface towards the hydrostatic axis, measured in the meridional plane, physically interpreted as concrete's internal angle of friction
- *Eccentricity:* Ratio of tensile strength of concrete to that of its compressive strength
- *Kc:* Ratio of the distances between the hydrostatic axis to the compression and tension meridian in the deviatoric cross section respectively.

Stress-strain behaviour under Uniaxial Compression:

The stress-strain relation for a given concrete can most accurately be described on the basis of its uniaxial compression tests. The theoretical stress-strain curve for a given grade of concrete is defined as the sum of elastic and inelastic segments for material definition in CDP model. Elastic region is defined with Young's Modules of unconfined concrete(E_0) and poison's ratio (μ). Although such non-linear behavior occurs from the beginning of stress-strain curves in experimental results. While transforming total strain into elastic and inelastic strains, one must consider an initial elastic segment as isotropic and the inelastic segment where the nonlinear behaviour of concrete initiates. Fig. 3.12 represents the CDP model under uniaxial compression in Abaqus.

$$\varepsilon_c{}^{\sim in} = \varepsilon_c - \varepsilon_{0c}{}^{\sim el} \tag{3.50}$$

$$\varepsilon_{0c}{}^{\sim el} = \left(\frac{f_c}{E_0}\right) \tag{3.51}$$

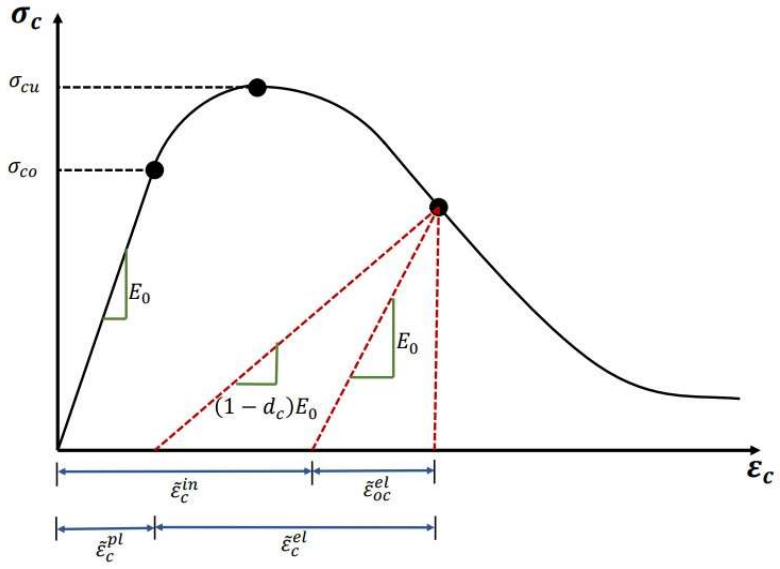

Fig. 3.12. Stress-strain Model for Uniaxial Compression

$$\varepsilon_c{}^{\sim pl} = \varepsilon_c{}^{\sim in} - \left(\frac{d_c}{1-d_c}\right)\frac{\sigma_c}{E_0} \tag{3.52}$$

$$\sigma_c = (1-d_c)E_0\left(\varepsilon_c - \varepsilon_{0c}{}^{\sim pl}\right) \tag{3.53}$$

$$\overline{\sigma_c} = \left(\frac{\sigma_c}{1-d_c}\right) \tag{3.54}$$

After defining the yield stress and corresponding inelastic strain, damage parameter d_c and d_t are defined, where its values range from 0 for an undamaged material to 1 for the total loss of load-bearing capacity. Using the Eq. 3.55 to 3.57, CDP model allowed us to determine the plastic strain $\varepsilon_c{}^{\sim pl}$in the analysis, although the plastic strain is calculated by Abaqus.

In the above equations, E_o, σ_c and $\overline{\sigma_c}$ represents initial modulus of elasticity for undamaged material in compression, uniaxial compression, and effective uniaxial compression. If a user fails to define damage parameters, then Abaqus will consider the defined concrete continuum as plastic and generating higher stress results compared to models with damage parameter.

Stress-strain behaviour under Uniaxial Tension:

Cracking strain $\varepsilon_t^{\sim ck}$ is used in CDP model for definition of concrete behavior in tension. The main objective is to account the phenomenon of tension stiffening. Concrete under tension not regarded as a brittle elastic body and phenomena such as aggregate interlocking in a crack and concrete to steel adhesion between cracks are to consider. This assumption is valid when crack patterns are fuzzy. Cracking strain is defined as the difference between total strain and elastic strain for the undamaged material as mentioned. Fig. 3.13 represents the CDP model under uniaxial tension in Abaqus.

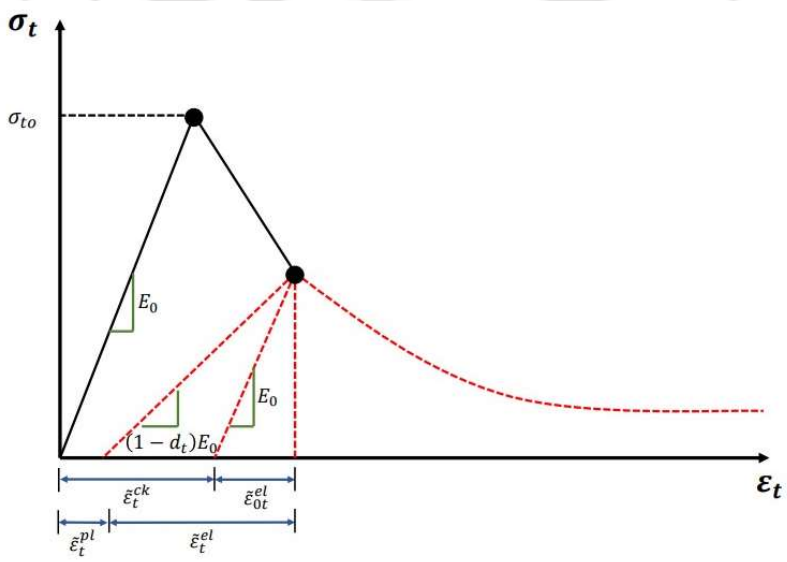

Fig. 3.13. Stress-strain Model for Uniaxial Tension

$$\varepsilon_t{}^{\sim ck} = \varepsilon_t - \varepsilon_{0t}{}^{\sim el} \tag{3.55}$$

$$\varepsilon_{0t}{}^{\sim el} = \left(\frac{f_t}{E_0}\right) \tag{3.56}$$

$$\varepsilon_t{}^{\sim pl} = \varepsilon_t{}^{\sim ck} - \left(\frac{d_t}{1-d_t}\right)\frac{\sigma_t}{E_0} \tag{3.57}$$

In the above equations, $\varepsilon_t{}^{\sim ck}$, d_t and E_t represents concrete cracking strain, damage parameter in tension and initial modulus of elasticity for undamaged material in tension.

Reinforcement Definition:

Rebar in Abaqus is used to define layers of uniaxial reinforcement in membrane, shell, and surface elements in FE Models [Abaqus, 2018], It can also be used to add discrete axial reinforcement in beam elements or coupled with temperature or in displacement control analysis, which do not contribute to the thermal conductivity and specific heat.

Longitudinal and transverse reinforcement in FE Models were defined as elastic perfectly plastic stress strain behavior. Plastic segment is defined with yield stress versus plastic strain values as represented in Table 3.2 and the elastic segment with Young's Modulus of 200 GPa and Poison's ratio (μ) as 0.3.

Table 3.2. Reinforcement Definitions for FE Analysis

Material	Elastic Region	Plastic Region	
		Compressive behaviour	Tensile behaviour
Steel	Young's Modulus (E_s)	Yield Stress: f_s	Yield Stress: f_s
	Poison's Ratio (μ)	Plastic Strain: $\varepsilon_s - \left(\frac{f_s}{E_s}\right)$	Plastic Strain: $\varepsilon_s - \left(\frac{f_s}{E_s}\right)$

3.4.4.2 Unconfined Concrete model by Mander et al. (1988)

Damage behaviour for confined and unconfined concrete is different [Liang *et al*. (2018)]. However, confinement effect of transverse reinforcements is automatically implemented and considered in the algorithm as concrete columns experiencing dilation in failure zone

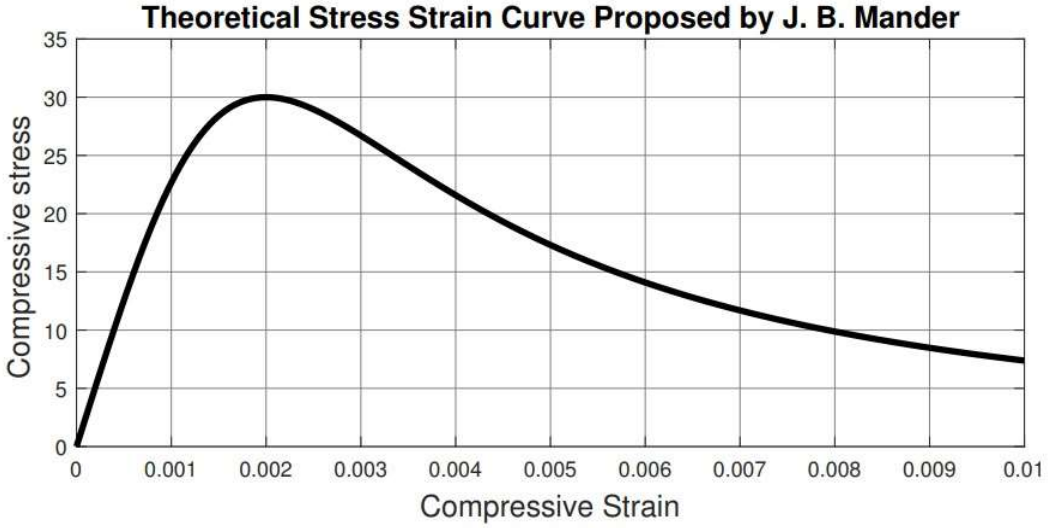

induces the lateral confining pressure from transverse steel within the FE Model [Aboulai *et al.* (2019)]. Keeping in view of the above conditions, concrete elements have been defined as unconfined concrete. The model of Mander *et al.* (1988) (Eq. 3.7 to 3.13) for unconfined concrete becomes the input. As a single equation defines both the ascending and descending branch of concrete behaviour, any abrupt and discontinuous change in stress values after peak strength leads to convergence warnings in FE Analysis.

Fig. 3.14. Stress-strain Model for Unconfined Concrete (Mander *et al*. (1988))

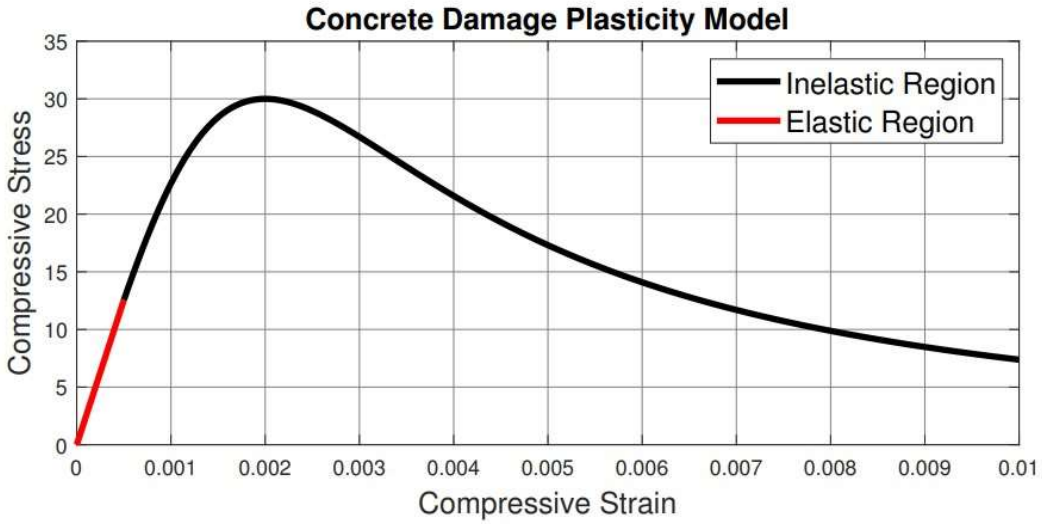

Fig. 3.15. Conversion of Mander's Stress-strain Model to CDP Model for Unconfined Concrete

To define the stress-strain behaviour of unconfined concrete, total strain ε_c is considered in the range varying from 0 to 0.01, where ε_{co} in 0.002. Fig. 3.14 represents unconfined stress strain model for M30 grade of concrete, which has been provided as input in the analysis.

Elastic region in the CDP model is defined with Elastic Modulus for unconfined concrete (E_o) and poison's ratio (μ) as 0.2. In CDP model, concrete stress-strain model will continue up to a stress value as mentioned in Eq. 3.58 for defining the elastic region and the rest of curve was obtained by removing elastic strains $\varepsilon_{oc}^{\sim el}$ from total strain ε_c while keeping compressive stress values undisturbed.

$$f_c = E_c \varepsilon_c \ , \qquad f_c < 0.4 f_{co} \tag{3.58}$$

$$f_c = \left(\frac{f_{co} x r}{r - 1 + x^r}\right), \qquad \varepsilon_{oc}^{\sim el} \leq \varepsilon_c \leq 0.01 \tag{3.59}$$

$$d_c = \left(1 - \frac{f_c}{f_{co}}\right), \qquad d_t = \left(1 - \frac{f_t}{f_{to}}\right) \tag{3.60}$$

Compression damage (d_c) and tension damage (d_t) [Cao *et al.* 2013] are defined with Eq. 3.60. Damage parameter d_t and d_c introduce damage in the CDP model after peak stress is achieved. Abaqus/CAE [Abaqus, 2018] recommends to defined these parameters in concrete model without which concrete exhibit a plastic behaviour which will inflate the resultant stress strain curve. Fig. 3.15 represents the converted stress-strain model input in Abaqus/CAE 2019. Table 3.3 represents the concrete behaviour in tension. Tensile strength [Rashid *et al.* 2002] of unconfined concrete is defined with Eq. 3.61.

$$f_{to} = 0.47 (f_{co})^{0.56} \tag{3.61}$$

Table 3.3. Tensile behaviour of Unconfined Concrete for CDP Model

Tensile Stress	Damage Variable (d_t)	Cracking Strain
f_{to}	0	0
$0.8 f_{to}$	0.2	0.008

3.4.4.3 Model Formulation

Concrete in Finite Element Models has been modelled with C3D8R solid (continuum) element (Fig. 3.16) and rebars, which included both longitudinal and transverse reinforcement were modelled with T3D2 (Fig. 3.17) elements. C3D8R element is a continuum three-dimensional (3D) eight-noded solid element with three translational degrees of freedom at every node with reduced integration including hourglass effect, whereas T3D2 elements are three-dimensional two noded linear displacement element.

Three-Dimensional Solid Continuum Element:

Solid (continuum) elements are standard volume elements in Abaqus. It doesn't include structural elements such as beams, shells, membranes, or trusses and it can be composed of

a single homogeneous material or several layers of different materials for analysis of composite solids. In this study a single homogeneous material for the concrete section was assigned with C3D8R (Fig. 3.16).

Abaqus solid element library includes first order (linear) interpolation elements and second-order (quadratic) interpolation elements for three dimensional elements. Triangles and quadrilaterals are available for two dimensions whereas tetrahedral, triangular prisms, and hexahedra (bricks) are provided in three dimensions. Abaqus recommends avoiding first order triangular and tetrahedral elements in stress analysis problems as it may overlay a stiff behaviour and exhibit slow convergence with mesh refinement.

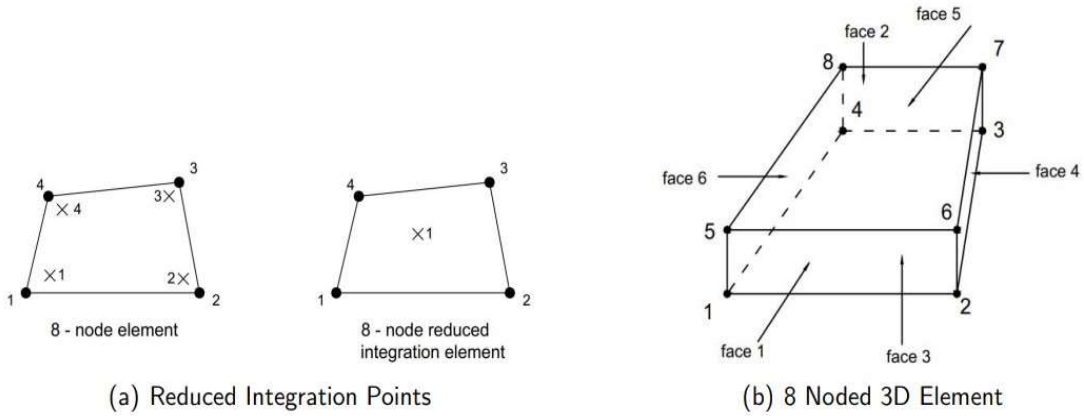

Fig. 3.16. Solid Continuum Discretization with C3D8R

Three-Dimensional Truss Element:

Truss elements are long, slender structural members that are capable of transmitting axial force only. Two noded three-dimensional truss element is used for modelling reinforcing rebar in reinforced concrete structures. Fig. 3.17 represents the Truss element used in the FE Analysis.

Embedded Constraint:

Embedded constraint definition is used to specify a set of elements that are physically embedded inside host elements. Embedded constraint is defined for both longitudinal and transverse reinforcements while making solid concrete continuum as host. The mechanism involves the nodes of an embedded element lying within a host element, there translational

degrees of freedom are constrained to the interpolated values that correspond to degrees of freedom of host element. Fig. 3.18 represents the constraint definition in FE Models.

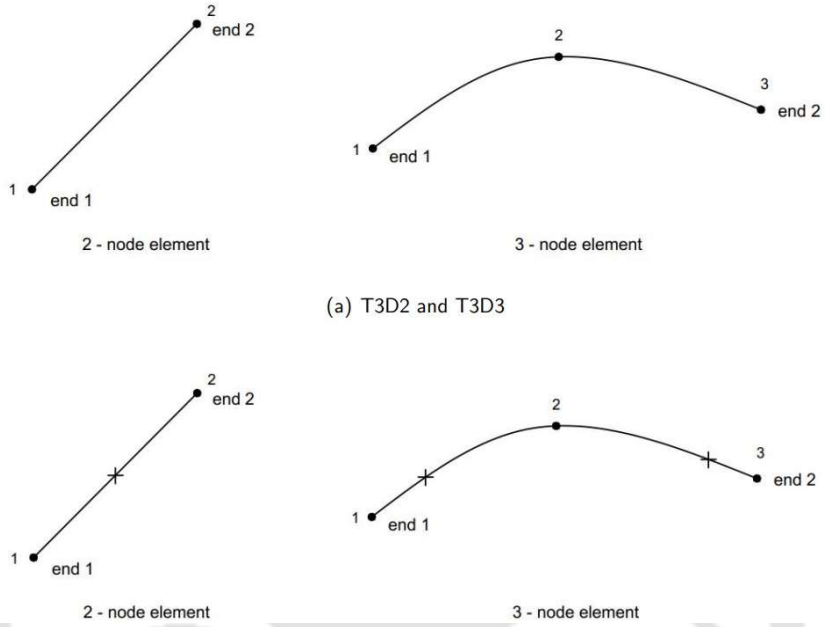

Fig. 3.17. Three Dimensional Truss Elements

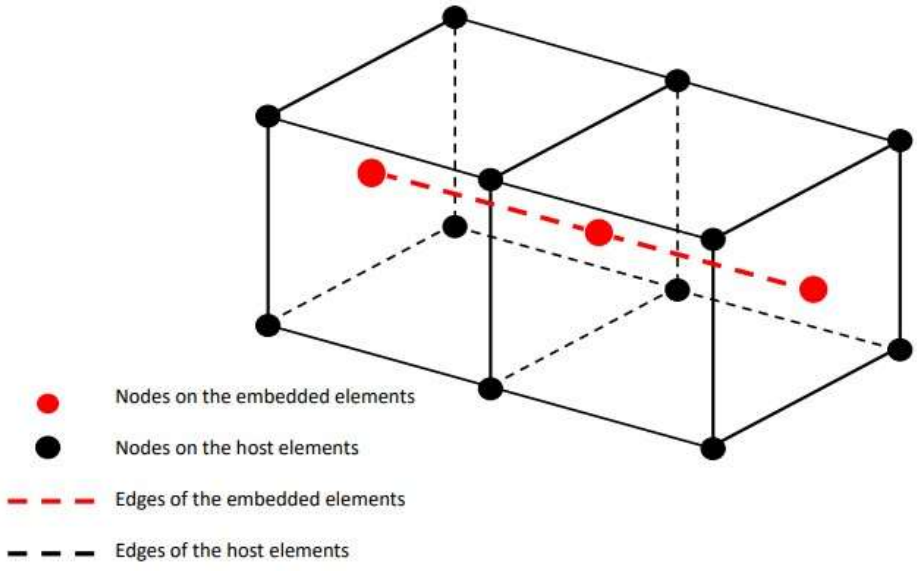

Fig. 3.18. Embedded Elements in Host Elements

Boundary and Loading Conditions:

The uniaxial concrete compression was achieved by imposing the boundary conditions as described by Liang *et al.* (2018), where one end of the columns was restricted in all the degrees of freedom while a uniform compression in Z direction was applied keeping the translational degrees of freedom X and Y direction restricted on the applied surface. The above boundary conditions resulted in a uniaxial confined compressive failure in the FE model along the column height away from the boundary surfaces.

Convergence Criteria:

Finite Element Analyses were carried out on the FE model of RC columns with solid and hollow Section. The specimen experienced large deformation, which will invoke the non-linear behaviour embedded with the CDP Model which represents the unconfined concrete. The objective of this study is to analyse the comparative effects of the confinement for different sections with varying reinforcement ratios. Table 3.4 represents the Converging parameters that were used for obtaining converging results in the analysis. These parameters play a key role during analysis as Abaqus default converging parameters are too strict. As a result, unanticipated warnings might generate. Caution should be taken as most of the analysis will be analysed without any warnings with these parametric values, but a warning free analysis is finalized after checking the warning messages in the log file as Abaqus doesn't report the warning messages if it predicts a converging solution on approaching steps. I_o represents the number of consecutive equilibrium iterations, after which check is made whether residuals are increasing in two consecutive iterations while I_R represents the number of consecutive equilibrium iterations at which logarithmic rate of convergence begins. Abaqus/CAE [Abaqus, 2018] recommends parametric values to be used to avoid any premature cutback in the analysis time. R_n^α and C_n^α represents convergence criterion for a ratio of largest residual to corresponding average flux norm for convergence and convergence criterion for a ratio of largest solution correction to the largest corresponding incremental solution value respectively.

Table 3.4. Solution Control Parameters for Converging Results

Parameters	R_n^α	C_n^α	ε^α	I_o	I_R
Values	0.02	2	0.0001	8	10

3.4.4.4 Validation Using Solid Circular Section

Validation of the computational approach was first done with experimental test results obtained from Mander *et al.* (1988). The original dimension of columns used by Mander *et al*. (1988b) for experimental investigation has been used for analysis of present study. Table 3.5 presents the detailed dimension with material definitions used for the FE Model for simulation in Abaqus/CAE 2021. In Table 3.5, N represents the number of longitudinal reinforcement bars, f_y, f_{yh} and f_{co} represent yield stress of longitudinal and transverse reinforcement, unconfined concrete strength respectively. In FE Analysis circular hoop reinforcement were used in place of the spiral reinforcement for convenience as the model proposed by Mander *et al.* (1988b) holds good for both spiral and circular reinforcements.

Table 3.5. Detailing of Circular Columns

Column no.	Longitudinal Reinforcement		Transverse Reinforcement		Material Strength		
	N	Diameter	Diameter	Spacing	f_{co}	f_y	f_{yh}
C1	12	16	12	41	29	295	340
C2	12	16	12	69	29	295	340
C3	12	16	12	103	29	295	340

Boundary conditions mentioned earlier along with the uniaxial compression loading in Z direction, while restricting *X* and *Y* degrees of freedom on the loading face was applied in the FE Models for every reinforced concrete column mentioned in the Table 3.5. As FE Analysis are sensitive to domain discretization and the application of strain rate, analysis was carried out on all the columns keeping identical mesh sizes and strain rate for comparison of results. While the computation of analysis warnings which included excessive distortion and creep convergence algorithm failures were encountered, but these warnings were eliminated with convergence criteria mentioned before. A sensitivity

analysis was carried on column $C1$ and based on the result a uniform mesh size was selected for FE model of solid sections.

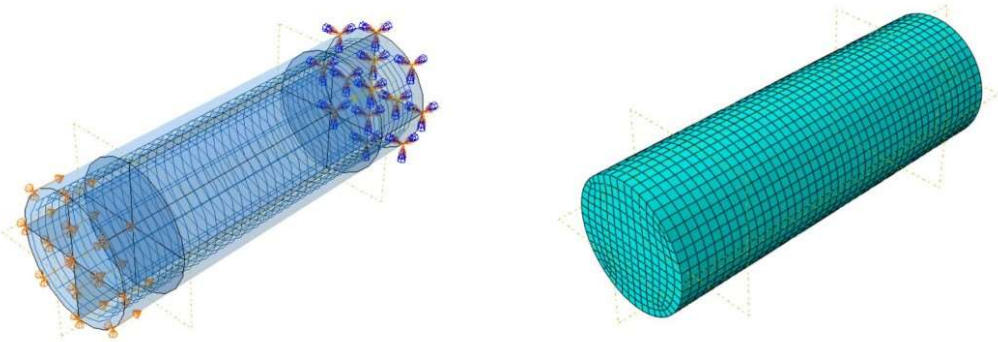

Fig. 3.19. Finite Element Modelling of Circular Column in Abaqus

Dilation of concrete occurred at the central region in the column, as shown in Fig. 3.20 and referred as the failure zone in this study. A similar approach was followed by Mander *et al.* (1988) in their experiment on a short column with a higher confinement ratio at the top and bottom of the columns resulted in a compressive failure at mid height. Experimental columns were tested with a DARTEC machine [Mander *et al.* (1988)], where monotonic compressive loading was applied. Keeping in view of the results mentioned above, similar trend was observed in FE Analysis.

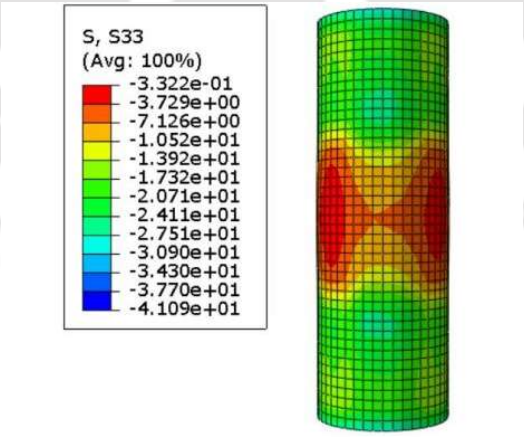

Axial Stress variation of Column C1

Fig. 3.20. Failure zone of Circular Section

Table 3.6 summarizes the parameters, which were used to determine the peak stress and peak strain for the columns based on theoretical model by Mander *et al.* (1988). Table 3.7

presents the effect of mesh refinement in the analysis of model shown in Fig. 3.20. With increase in mesh refinement, FE response for column C1 were matching with the theoretical result as predicted. However, mesh refinement increased the analysis time and hence for all the subsequent analyses, 40mm mesh size was adopted for somewhat reduced computational time requirement.

Table 3.6. Reinforcement Detailing of solid Circular Columns

Column	Longitudinal Steel Ratio (ρ_{cc})	Transverse Steel Ratio (ρ_S)	Confinement Effectiveness (k_e)	Max. Unconfined Strain (ε_{co})
C1	0.016	0.025	0.9501	0.0015
C2	0.016	0.015	0.8883	0.0015
C3	0.016	0.010	0.8161	0.0015

Table 3.7. Sensitivity Analysis for Column C1

Sl. No.	Mesh Size (mm)	Unconfined Strength (in Mpa)	Confined Strength (in Mpa)	
			Theoretical	FEA
1	45	30	50.5364	48.7476
2	40	30	50.5364	49.1165
3	35	30	50.5364	49.3285
4	30	30	50.5364	50.0686
5	25	30	50.5364	50.3430

Fig. 3.21 represents the FE Responses for cylindrical columns C1, C2 and C3 obtained at the central Node 1 in between two consecutive transverse reinforcements in the failure zone as shown in Fig. 3.20 and the same results were compared with corresponding proposed theoretical stress-strain model by Mander *et al.* (1988). Stress-strain Curves observed from the FEA matched with the theoretical model. This observation confirmed that the modelling approach and the material model satisfactorily characterized the confinement effect in terms of enhanced strength and ductility characteristics of confined concrete section.

All FE responses were recorded in between the transverse stirrup level for every analysed column. This approach was adopted as the concrete dilation was maximum between the

transverse stirrup level at mid-height in the columns. Uniform axial compression resulted in the concrete elements to dilate radially.

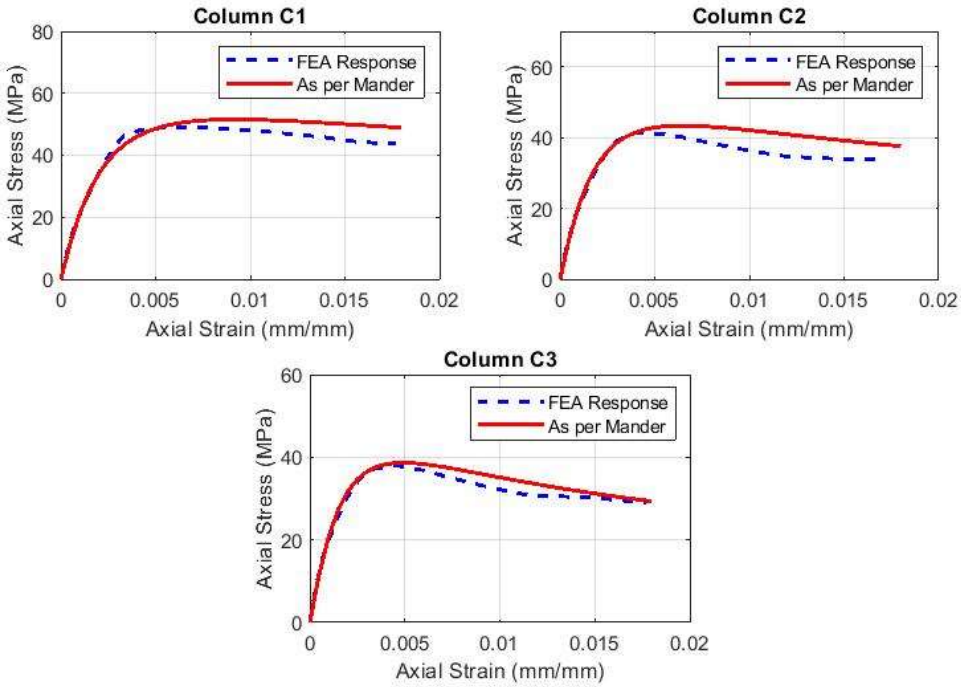

Fig. 3.21. Comparisons of computational axial stress-strain responses of confined solid concrete columns with those obtained from Mander *et al.* (1988).

3.4.4.5 Circular Hollow Section

Finite element formulation for Circular Hollow Section as shown in Fig. 3.1 was carried out. Due to the symmetry of column sections about *X* and *Y* direction, 1/4th section of the column was analysed in the FE Model. Lower end of the hollow section was restrained in all degrees of freedom, while *X* and *Y* symmetric constraint were applied on surfaces perpendicular to *X* and *Y* axis, respectively. Aspect ratio (Height of column/ diameter) ratio of 3 was maintained for all the models considered. Fig. 3.22 shows the details of models with 1/4th section as well as full section.

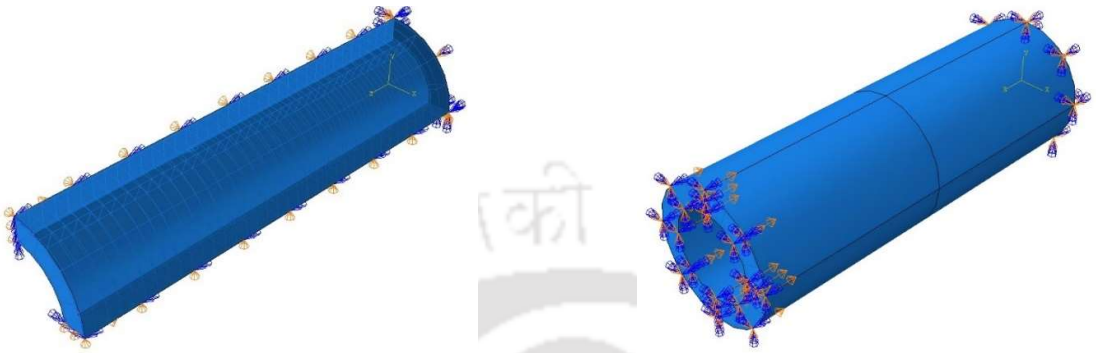

Fig. 3.22. Part and Whole Model of Circular Hollow Section

To check the confinement effect in hollow circular piers, 4 columns were analysed using FE method in Abaqus. These sections were taken from the existing bridge between Khongsang and Noney under new BG rail line construction between Jiribam and Tupul (Imphal), India. Table 3.8 shows the detail of the columns considered for the present study.

Table 3.8. Detailing of Circular Hollow Column Section

Column	Outer Diameter (mm)	Inner Diameter (mm)	Longitudinal Reinforcement		Transverse Reinforcement	
			No. of bar on one face	Diameter of bar (mm)	Diameter of bar (mm)	Spacing (mm)
P1	7500	6500	188	32	16	150
P2	9000	8000	235	25	16	150
P3	12000	10500	215	32	16	150
P4	16000	14000	340	32	16	150

The inner and outer hoops are connected using cross ties. These cross ties are provided on alternate longitudinal bars.

A door is provided at the bottom in a hollow pier. It serves as an access point to the interior of the pier. This is for the purpose of inspection, maintenance, or other activities that require entry into the hollow pier. The effect of such openings on the confining effect has been studied. It should be ensured that due to this opening the load carrying capacity and the confined strength of the pier should not get significantly affected.

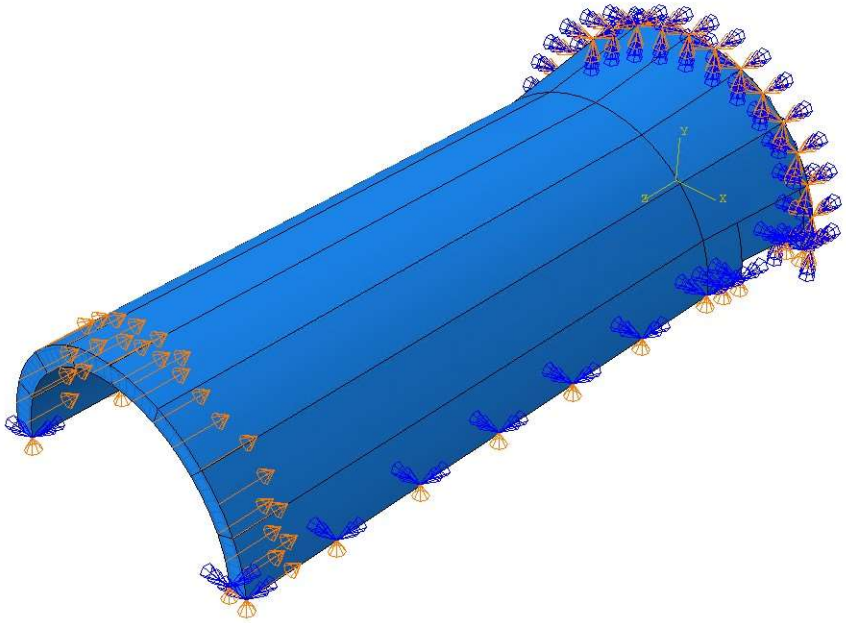

Fig. 3.23. Model of Circular Hollow Section with opening at bottom

Analysis of a long hollow circular column with an opening at bottom is done and it is compared with the performance of the same column without an opening. Finite element model of circular hollow section with opening is shown in Fig. 3.23. The column with opening is symmetric about one axis and hence one-half section of the column was modelled and analysed using FE method. The door opening dimension is 1000 x 2100.

Generally, hollow column is preferred over a solid column when the outer diameter of a column section exceeds 4.0m. Hollow section becomes more economical than solid section in such cases. Keeping this point in mind, a hollow section with outer diameter of 4m was considered for the parametric study.

To check the validity of using FE model with1/4th section for analysis, the part and whole model for hollow circular section were analysed (Table 3.9). Fig. 3.24 confirms that the results obtained from part model matches well with that of whole model. In addition to this, confined concrete stress-strain curve as obtained from Mander *et el*. (1998) by calculating the confinement effectiveness coefficient using a modified formula given in section 3.4.3. This observation confirmed that the modelling approach gives satisfactorily results for confinement effect in terms of enhanced strength.

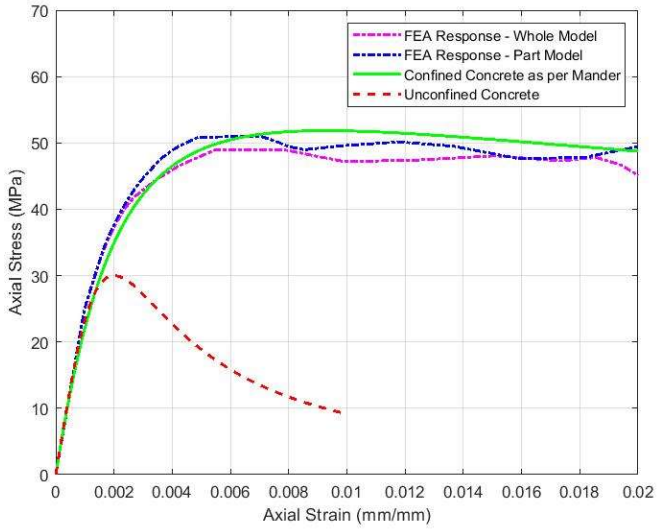

Fig. 3.24. Comparisons of computational axial stress-strain responses of confined hollow concrete columns with those obtained from Mander *et al.* (1988) model

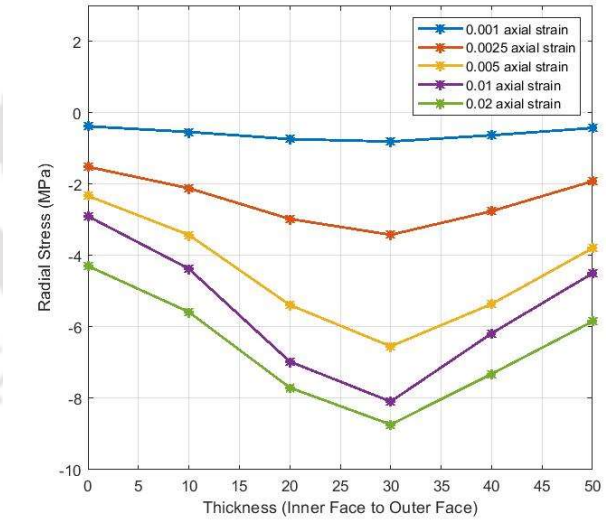

Fig. 3.25. Radial Stress Variation along thickness for Hollow Column HC

Table 3.9. Detailing of Circular Hollow Column Section

Column	Outer Diameter (mm)	Inner Diameter (mm)	Longitudinal Reinforcement		Transverse Reinforcement	
			No. of bar	Area of bar (mm^2)	Area of bar (mm^2)	Spacing (mm)
HC	304.8	203.2	16	31.669	14.862	25.4

Under the application of uniform axial compression, concrete crushing was observed on the inner face. Compressive demand generated on the inner face was transferred radially outward under the influence of crossties which underwent tension due to concrete dilating outwards. Fig. 3.25 shows the variation in radial stress throughout the load application, where outer concrete elements have more radial stress compared to inner face. This result corroborates the consideration of lesser confinement effect at inner face of concrete compared to outer face based on which the expression of k_e for hollow circular pier section has been proposed as given in Eq. 3.49.

Table 3.10. The reinforcement detailing of hollow circular sections, their confinement effectiveness coefficient using the proposed formula (Eq. 3.49) and comparison between the confined compressive strength as obtained from theoretical and the FE model

Column	Longitudinal steel ratio (ρ_{cc})	Transverse steel ratio (ρ_s)	Confinement Effectiveness Coefficient (k_e)	Unconfined compressive strength (f_{co})	Confined compressive strength (f'_{cc})		Numerical/ Theoretical
					As per above proposed formula (MPa)	From FEA Response (MPa)	
P1	0.04117	0.0080	0.5704	40	47.43	45.81	0.966
P2	0.0260	0.0080	0.5497	40	47.17	46.64	0.989
P3	0.0165	0.0046	0.6489	40	44.94	44.31	0.986
P4	0.0139	0.0032	0.7895	40	44.24	41.85	0.946

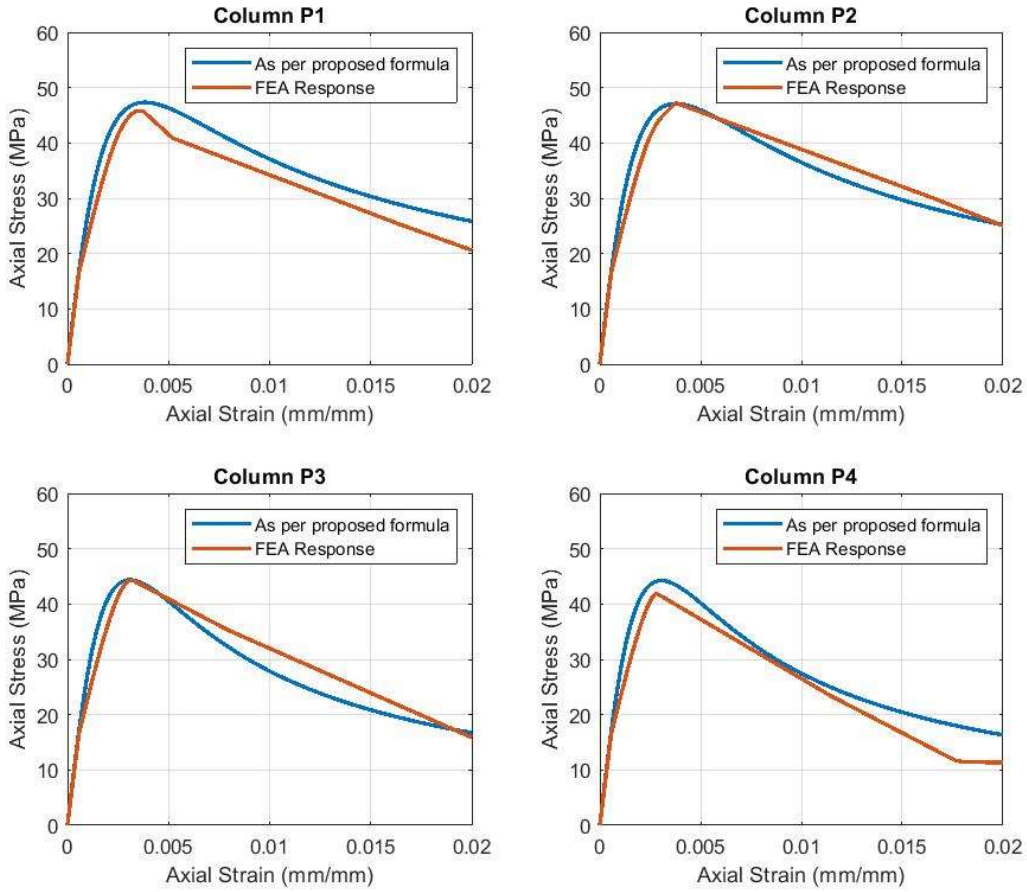

Fig. 3.26. Comparisons of computational axial stress-strain responses of confined hollow concrete columns with those obtained from the proposed formula.

The hollow circular columns as detailed in Table 3.8 has been analysed using FE method in Abaqus. Load applied to the model was displacement controlled. The rate of application of displacement was 10mm/sec to make sure that the loading is gradual and not sudden. The time increment step was restricted to 0.01 to avoid strain increment warning in FEA. Table 3.10 and Fig. 3.26 show that the confined compressive strength and the stress-strain graphs obtained from FEA and that is obtained from the proposed formula as shown in Eq. 3.49 are very close to each other.

Circular hollow section with opening in the wall corresponding to the Column P4 (Refer Table 3.8) has been analysed. The FE model is shown in Fig. 3.23. The stress-strain plot of concrete near the opening zone as obtained from the finite element analysis and the same as per Mander *et al*. (1988) using the proposed k_e have been plotted along with the same without any opening in the wall of the hollow circular column and are shown in Fig. 3.27. From Fig. 3.27, it is found that there is some reduction in the maximum strength of the section, which is logical. Further, the section with opening could sustain strain up to 0.01 in comparison to 0.02 for section with no opening as may be observed from Fig. 3.26 and 3.27. The proposed response reduction factor for hollow circular section with wall opening has thus been estimated in such a way that strain capacity remains within 0.01 in the stress-strain relation of concrete.

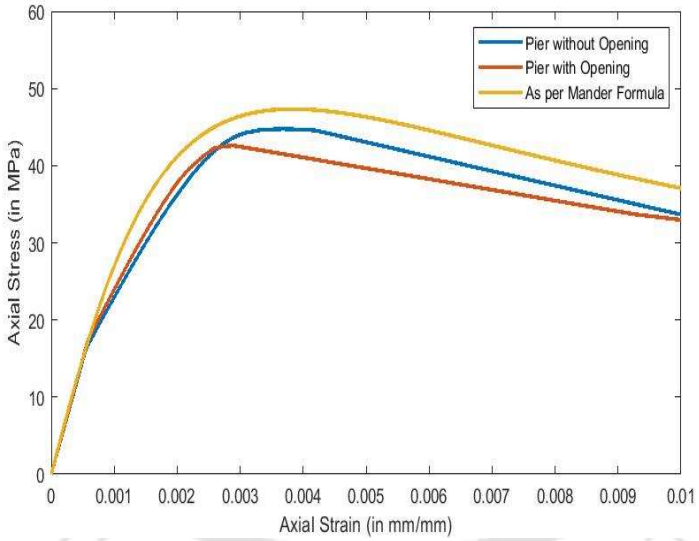

Fig. 3.27. Comparison of computational axial stress-strain responses of confined concrete columns with and without opening with those obtained from the model of Mander et al. (1988) with proposed k_e

3.4.5. Ultimate strain in concrete

Ultimate strain in concrete has been estimated from strain energy of the concrete section of confined concrete, confining steel and the main steel at which first fracture occurs at confining steels as suggested by Mander *et al.* (1988). The value depends on the various parameters namely confining steel ratio (ρ_s), main steel ratio (ρ_{cc}), grade of concrete (f_{ck}),

grade of steel (f_y), spacing of confining steel (s') and dimension of the confined section (b'').

The basic principle is that the difference in strain energy between confined and unconfined concrete is considered to be imparted by the strain energy of the confining steel. Longitudinal steel also undergo strain and thus this is also considered in the energy equation. The energy stored in unconfined and confined concrete is basically the area under corresponding stress-strain curve as shown in the Fig. 3.6 and Fig. 3.7 respectively. Confined curve shall be considered up to the ultimate strain ε_{cu} in concrete where the first fracture occurs in confining/ transverse steel. Thus, the difference in energy stored in confined and unconfined concrete plus the energy stored in the longitudinal steel can be equated to the strain energy stored in transverse steel. As energy stored in confined concrete and in longitudinal steel is a function of ε_{cu}, the value of ε_{cu} is calculated numerically by means of iteration. The above strain energy principle expressed in the Eq. 3.62 is as per Mander *et al.* (1988). The left term of the equation is the strain energy of transverse steel, the first right term is the strain energy of the confined concrete, second right term is the strain energy in longitudinal steel and third right term is the strain energy in the unconfined concrete.

$$\rho_s A_{cc} \int_0^{\varepsilon_{sf}} f_s d\varepsilon_s = A_{cc} \int_0^{\varepsilon_{cu}} f_c d\varepsilon_c + \rho_{cc} A_{cc} \int_0^{\varepsilon_{cu}} f_{sl} d\varepsilon_c - A_{cc} \int_0^{\varepsilon_{sp}} f_c d\varepsilon_c \qquad (3.62)$$

Table 3.11 shows the ultimate concrete strain calculated numerically by iteration as per Mander *et al.* (1988) for section with Grade of concrete M40, Grade of steel Fe500, Confining steel spacing 100mm, width of confinement 850mm, i.e. the section being used in the present study. From Table 3.11 it is found that the maximum concrete strain may go beyond 0.02 depending on the transverse steel ratio. However, in the moment *vs* curvature graph, the maximum concrete strain has been restricted to 0.02.

The ultimate strain in concrete as per Mander *et al.* (1988) depends on various factors. If the spacing of stirrup is increased, the ultimate strain reduces because the transverse steel ratio reduces and thus the energy stored in the transverse steel also reduces.

With increase in grade of concrete the ultimate strain reduces. This happens because with increase in grade of concrete the area under stress-strain curve increases at same strain level. As the transverse reinforcement ratio remains same, the total strain energy of the transverse reinforcement at failure is also same. To equate this unchanged strain energy of transverse reinforcement with the strain energy of concrete and main reinforcement, the ultimate strain in concrete reduces.

With increase in grade of steel, ultimate strain in concrete reduces. This is because increased grade of steel contributes higher strain energy in main steel and to equate with the strain energy in transverse steel, strain energy in concrete need to be reduced which causes reduction in ultimate strain in concrete.

A simplified relationship between ultimate concrete strain and confining steel, ultimate strain in transverse steel and grade of concrete has been given by Priestly *et al.* (1996) and subsequently modified by Wei and Wu (2014). The relation is given as below:

$$\frac{\varepsilon_{cu}}{\varepsilon_{co}} = 1.75 + 900\varepsilon_{sf}\left(\frac{f'_l}{f'_c}\right) \tag{3.63}$$

Table 3.11. Ultimate strain in concrete estimated from strain energy of the concrete section at which first fracture occurs at confining steels as per Mander *et al.* (1988) for different ρ_s and ρ_{cc}

Ratio of transverse steel (ρ_s)	Ratio of main steel (ρ_{cc})			
	1%	2%	3%	4%
0.2%	0.0090	0.0079	0.0071	0.0065
0.4%	0.0137	0.0121	0.0109	0.0100
0.6%	0.0178	0.0158	0.0143	0.0131
0.8%	0.0214	0.0191	0.0174	0.0160
1.0%	0.0247	0.0222	0.0202	0.0186

Table 3.12. Ultimate strain in concrete estimated as per Wei and Wu (2014) for different ρ_s and ρ_{cc}

Ratio of transverse steel (ρ_s)	Ratio of main steel (ρ_{cc})			
	1%	2%	3%	4%
0.2%	0.0075	0.0076	0.0076	0.0077
0.4%	0.0116	0.0116	0.0117	0.0118
0.6%	0.0156	0.0157	0.0158	0.0160
0.8%	0.0196	0.0198	0.0199	0.0201
1.0%	0.0236	0.0238	0.0240	0.0243

Table 3.12 shows the ultimate concrete strain calculated as per Wei and Wu (2014). The comparison between the values shown in Table 3.11 and Table 3.12 as per the two methods shows that the value of the ε_{cu} is 5% to 17% less as per the method of Wei and Wu (2014) for main steel ratio 1%. However, the basic difference between the two methods lies in the impact on the main steel ratio. In the method of Mander *et al.* (1988), the ε_{cu} largely depends on main steel ratio and with higher percentage of main steel, ε_{cu} reduces as because amount of strain energy stored in the main steel reduces the strain energy stored in the concrete to balance the total energy, which is equal to the strain energy in the transverse steel at first fracture failure. In the method of Wei and Wu (2014) the main steel ratio nominally influences the f'_l value on which ε_{cu} linearly depends and in contrary to the method of Mander *et al.* (1988), the value of ε_{cu} increases with main steel ratio but the increase is negligible. As a result, for higher ratio of main steel (ρ_{cc} equals to 2% with ρ_s more than 0.6% and ρ_{cc} equals to 3% & 4%), the value of ε_{cu} is higher in case of Wei and Wu (2014) method. As such it appears that method given by Mander *et al.* (1988) is more realistic. The same is apparent from the findings by Munir *et al.* (2019) through their experimental result. As per Munir *et al.* (2019), the maximum difference of value of ε_{cu} is about 31% and the value is higher compared to the experimental result. As per Table 3.11 and Table 3.12**,** similar maximum difference is observed between the value as per Mander *et al.* (1988) and as per Wei and Wu (2014).

3.4.6. Yield deflection

During the calculation of deflection ductility, yield deflection and ultimate deflection are calculated first. Yield deflection is generally calculated from the height *vs* curvature plot (curvature along the height of the cantilever pier) with curvature corresponding to yield moment at base of cantilever and with the consideration that curvature linearly varying along the height of pier. This linear relation is applicable for beam member where axial load is zero. However, the relation is not linear for pier due to the influence of axial load even up to the yield moment. Un-cracked section shows kink at the moment *vs* curvature graph when the first crack occurs, but in the present case this effect has been ignored as cracked section property has been considered all through.

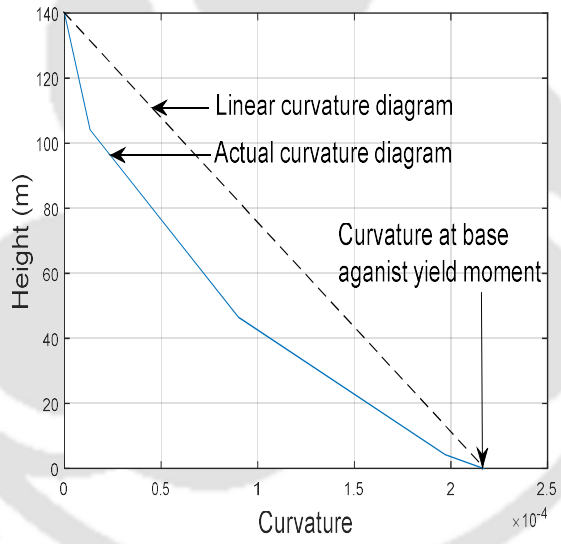

Fig. 3.28. Curvature *vs* height diagram up to yield moment at base of a pier (actual curve will be a smooth curve, in absence of multiple point this curve is piece wise straight line)

In order to understand the effect, the same 141m tall pier has been considered. Fig. 3.28 shows the height *vs* curvature graph of a section with main steel = 1%, *P/Afck* = 0.1, transverse steel = 0.2% and yield moment occurring at the base of pier. From the figure it is found that the area under the curve is 33% lesser than the same area considering linear relation between height and curvature i.e. the yield deflection is 33% less. In the present

study, both yield deflection and ultimate deflection have been calculated from the height *vs* curvature curve directly which gives more accurate results of deflection ductility.

3.4.7. Gross and cracked moment of inertia of section

Deflection of structure depends on the effective moment of inertia of section. In the present case, cracked moment of inertia has been used to get the deflection of the cantilever tip of pier i.e. from the moment *vs* curvature relation of cracked section at the base of the pier. The effective moment of inertia is function of cracked as well as gross moment of inertia and actual moment on the section. Standard formula has been used to evaluate the effective moment of inertia of the section. In this section, the effect on deflection ductility for the use of cracked section instead of effective section property is shown.

The standard relation between effective section property *vs* gross section property and cracked section property can be given as below:

$$I_e = \left(\frac{M_{cr}}{M_a}\right)^3 I_{gr} + [1 - \left(\frac{M_{cr}}{M_a}\right)^3] I_{cr} \tag{3.64}$$

where, I_e = Effective section moment of inertia; I_{cr} = Cracked section moment of inertia; I_{gr} = Gross section moment of inertia; M_{cr} = Moment at which first cracking in concrete occurs and M_a = Moment at base of cantilever pier for which effective section property is being calculated.

If maximum moment considerably exceeds the cracking moment, the stiffening effect of concrete tension capacity in between the cracks has much less significance and thus cracked section value I_{cr} can be used for calculation with little error. The formula of effective moment of inertia also suggests the same i.e. if M_a is much higher than M_{cr} then I_e will be close to I_{cr}. An analysis has been done to understand this effect from the problem dealt in the present case. With 16m outer diameter and 14m inner diameter of hollow pier, M40 grade of concrete, modulous of rupture 0.7(fck)^0.5, i.e. 4.427 MPa, the cracking moment comes about 74,000 tm ($M_{cr} = Z\sigma_{ct} = \frac{\pi}{64}\frac{16^4-14^4}{\frac{16}{2}} 4.427 = 73{,}668$ tm).

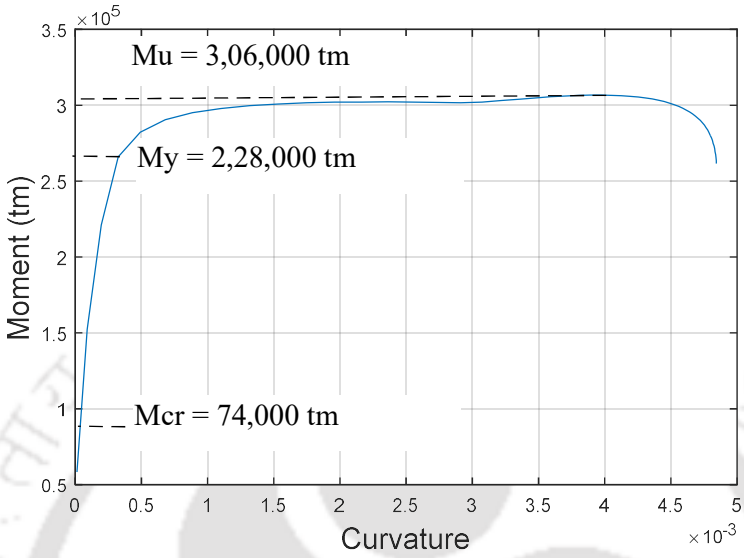

Fig. 3.29. Moment *vs* curvature curve for section property D_o = 16m, D_i = 14m, f_{ck} = 40Mpa, f_y = 500Mpa, ρ_{cc} = 1.0035%, ρ_s = 0.2% *b"* = 0.85m, S_h = 0.1m, P = 0.1 f_{ck}A

From the Moment-curvature analysis of section with ρ_{cc} = 1%, $P/A\,f_{ck}$ = 0.1 and ρ_s = 0.2%, yield moment capacity M_y of the section is 2,28,000 tm and ultimate moment capacity M_u is 3,06,000 tm (Refer Fig. 3.29). I_{cr}/I_{gr} for the same section is 0.32.

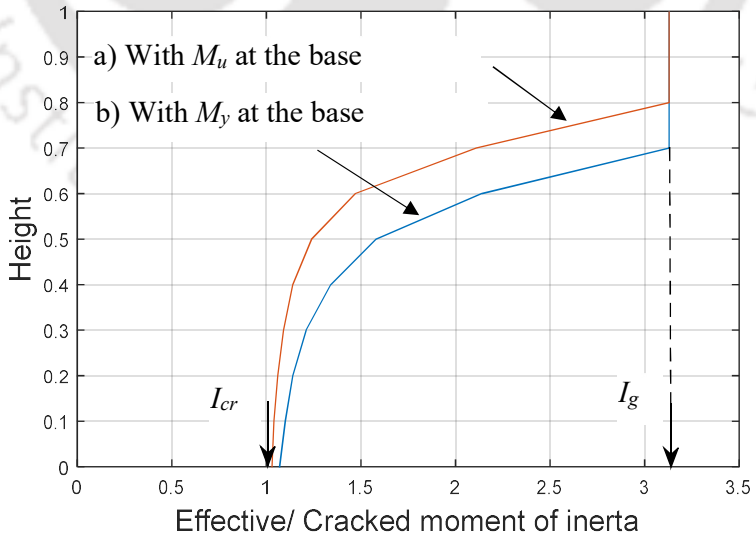

Fig. 3.30. Effective moment of inertia distribution of pier section along height of pier for two cases, a) With M_u at the base & b) With M_y at the base of pier

Table 3.13. Effective moment of inertia distribution along height of pier for yield moment at base and for ultimate moment at base (M_{cr} = 74,000 tm, M_y = 2,28,000 tm, M_u = 3,06,000 tm)

L	M_1 (M_y at base)	$\left(\frac{M_{cr}}{M_1}\right)^3$	$1-\left(\frac{M_{cr}}{M_1}\right)^3$	$\frac{I_{eff}}{I_{cr}}$	M_2 (Mu at base)	$\left(\frac{M_{cr}}{M_2}\right)^3$	$1-\left(\frac{M_{cr}}{M_2}\right)^3$	$\frac{I_{eff}}{I_{cr}}$
1.0				3.13				3.13
0.9	22,800	1.000	0.000	3.13	30,600	1.000	0.000	3.13
0.8	45,600	1.000	0.000	3.13	61,200	1.000	0.000	3.13
0.7	68,400	1.000	0.000	3.13	91,800	0.524	0.476	2.11
0.6	91,200	0.534	0.466	2.14	1,22,400	0.221	0.779	1.47
0.5	1,14,000	0.274	0.726	1.58	1,53,000	0.113	0.887	1.24
0.4	1,36,800	0.158	0.842	1.34	1,83,600	0.065	0.935	1.14
0.3	1,59,600	0.100	0.900	1.21	2,14,200	0.041	0.959	1.09
0.2	1,82,400	0.067	0.933	1.14	2,44,800	0.028	0.972	1.06
0.1	2,05,200	0.047	0.953	1.10	2,75,400	0.019	0.981	1.04
0.0	2,28,000	0.034	0.966	1.07	3.06,000	0.014	0.986	1.03

With the yield moment at the base of the pier, the effective moment of inertia distribution can be worked out and the same is shown in the tabular form Table 3.13 and graphically in Fig. 3.30. The calculated yield deflection is 1.052m from the height *vs* curvature curve based on moment *vs* curvature curve as shown in Fig. 3.29, which corresponds to cracked section property. If effective section property distribution along height of the pier is considered, as per stiffness approach, the deflection is found to be 16% less. In plastic zone effective section property is same as cracked section property and hence the plastic deflection calculated from the height-curvature curve will remain unchanged. Thus, the corrected yield deflection shall be 1.052m/1.16 = 0.9m. The ultimate deflection calculated from the height *vs* curvature is 3.586m, thus plastic deflection shall be 3.586-1.052 = 2.534m. Corrected ultimate deflection shall be 2.534m+0.9m = 3.434m. Deflection ductility without effective moment of inertia consideration is 3.586m/1.052m = 3.4. Corrected deflection ductility considering effective moment of inertia shall be 3.434m/0.9m = 3.815. Thus, the deflection ductility shall be 12% more if varying effective section property is used along the height of the pier. The percentage will be slightly more with higher transverse steel ratio.

3.4.8. Ultimate curvature – negative stiffness effect

For the sections where its property allows the ultimate strain to go to a high value like close to 0.02 or above, the large deflection at the top of cantilever may cause large additional moment due to *P-Δ* effect, which may lead to failure of the section causing post yield negative stiffness. In such cases, the ultimate strain shall be governed from this aspect and the value shall be restricted in such way that beyond that value only negative stiffness phenomena may occur. It has been found in general that if maximum ultimate strain is restricted to 0.02 then this phenomenon can be avoided.

3.4.9. Pounding due to deflection

In case of tall pier, large deflection may occur, which may cause pounding between the successive structures. After use of appropriate *R* value for designing the section, deflection need to be checked and adequate gap needs to be provided between successive structures to avoid pounding. In case the deflection is large enough to accommodate, pier section needs to be redesigned for higher stiffness so that deflection can be reduced within the maximum practical gap that may be provided between the successive structures.

3.4.10. Opening in the wall of hollow circular pier

Openings are generally provided at the bottom of the large diameter hollow pier for man entry purpose to enable inspection activity inside the pier. Due to the presence of the opening and depending on the size, the behaviour of the section changes. Moment-curvature curve changes depending on the size of the opening and as a result the deflection ductility also differs from that of the section having no opening. The effect of opening on *R* is discussed in more detail in next section.

3.5. Results obtained & discussion

In the following sections, effect of various parameters on *R* for large diameter hollow circular section with and without opening has been discussed as has been obtained from the analysis.

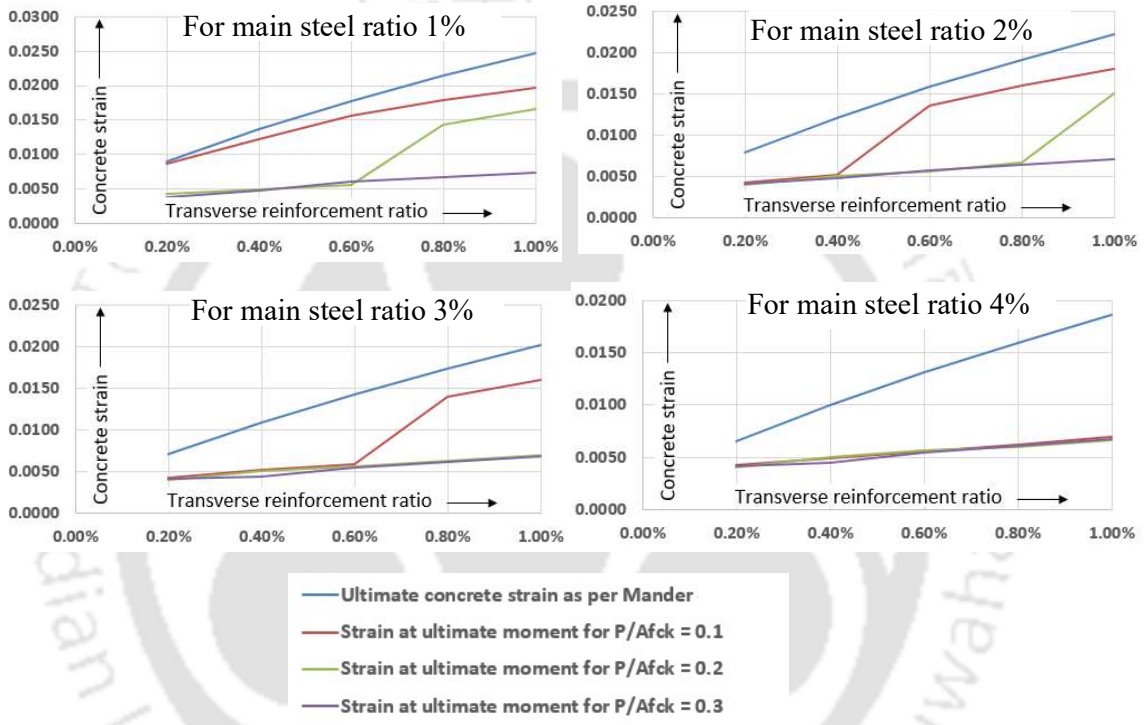

Fig. 3.31. Ultimate concrete strain *vs* transverse steel ratio

Ultimate concrete strain obtained from the energy principle as per Mander *et al.* (1988) has been found in general higher than the concrete strain corresponding to the ultimate moment capacity of the section. In general, it is found that the maximum deflection ductility of the section corresponds to the curvature at ultimate moment capacity. Fig. 3.31 shows graphically the gap between Ultimate longitudinal concrete strain at which transverse steel snaps (As shown in Section 3.4.5) as per Mander *et al.* (1988) and actual strain where section reaches ultimate moment.

3.5.1. Effect of spacing of stirrup on *R*

Effect of stirrup spacing on *R* has been studied. For two different stirrup spacings, 100mm and 150mm, keeping stirrup ratio i.e. percentage of transverse reinforcement same, the effect on *R* has been checked for the pier sections considered earlier. Fig. 3.32 shows the effect on stress-strain relation and Fig. 3.33 shows the effect on Moment-curvature curve for the hollow circular section with P/Af_{ck} = 0.1, ρ_s = 0.6%, ρ_{cc} = 1%, f_{ck} = 40MPa, fy = 500MPa .

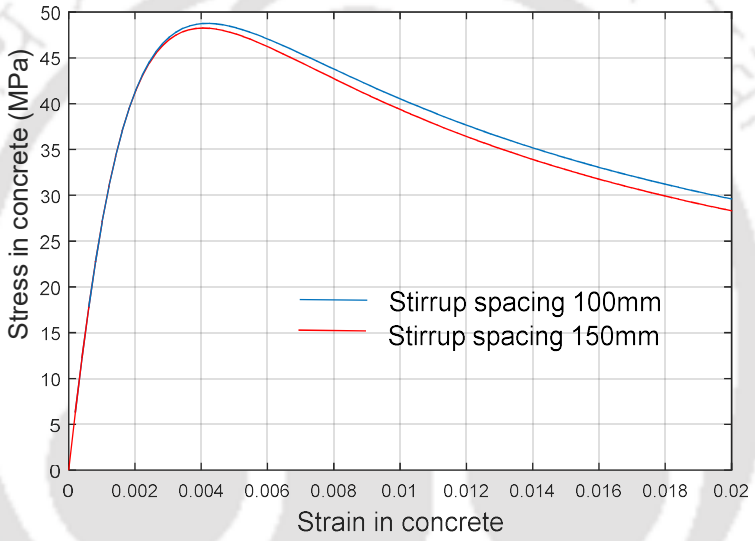

Fig. 3.32. Stress-strain curve for concrete as per Mander *et al.* (1988) for different stirrup spacing – ρ_s = 0.6%, d_s = 0.85m, ρ_{cc} = 1%, f_{ck} = 40MPa, fy = 500MPa

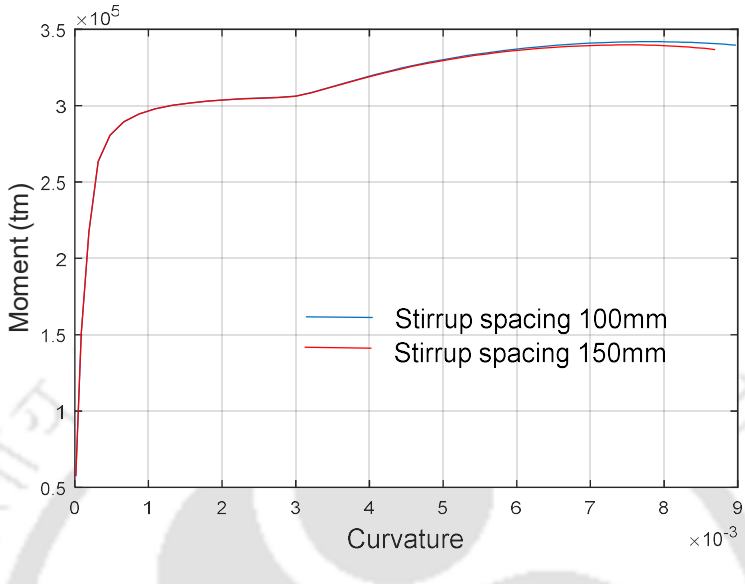

Fig. 3.33. Moment-curvature curve for circular hollow section for different stirrup spacing – D_o = 16m, D_i = 14m, P/Af_{ck} = 0.1, ρ_s = 0.6%, ρ_{cc} = 1%, f_{ck} = 40MPa, fy = 500MPa

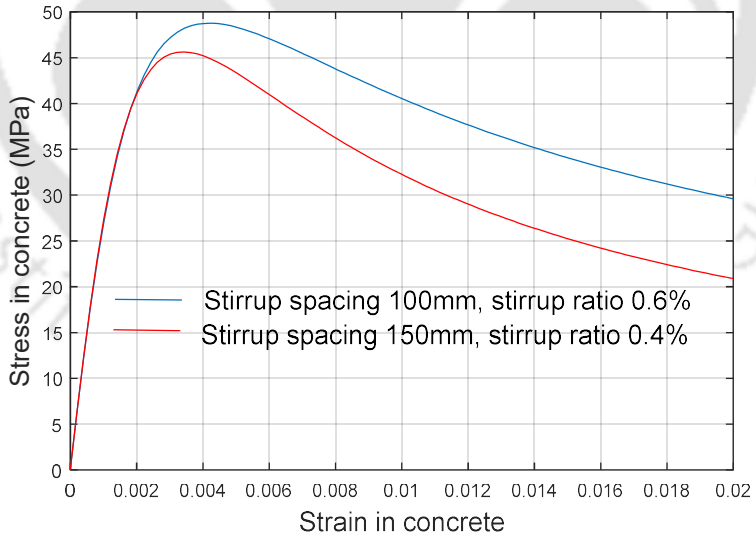

Fig. 3.34. Stress-strain curve for concrete as per Mander *et al.* (1988) for different stirrup spacing and stirrup ratio – D_o = 16m, D_i = 14m, ρ_{cc} = 1%, f_{ck} = 40MPa, fy = 500MPa

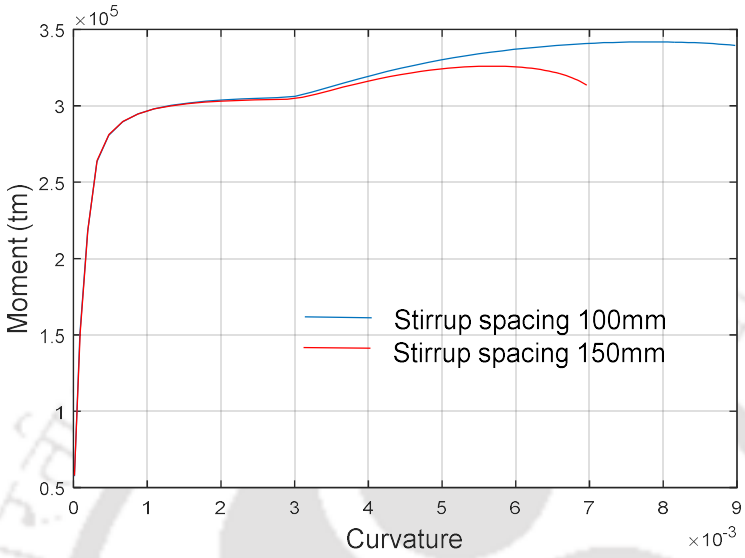

Fig. 3.35. Moment-curvature curve for circular hollow section for different stirrup spacing and stirrup ratio – D_o = 16m, D_i = 14m, P/Af_{ck} = 0.1, ρ_{cc} = 1%, f_{ck} = 40MPa, fy = 500MPa

In both the curves the difference is minor. The stress-strain curve shows that with higher stirrup spacing the area under the curve reduces and the ratio of the area is 0.975. From the Moment-curvature curve if deflection ductility is calculated, the value is lesser for the higher stirrup spacing and the ratio of the values is 0.95 (10.404/10.94). Thus, it can be concluded that effect of stirrup spacing, assuming the spacing will vary between 100mm to 150mm, keeping the percentage of stirrup unchanged, is to the tune of 5% and hence this parameter has been ignored for estimating the value of *R*.

The Stirrup spacing has been changed without changing the diameter of stirrup, i.e. the percentage of transverse reinforcement is also changed and accordingly the effect on *R* has been studied. The stirrup spacing has been considered 100mm and corresponding stirrup ratio 0.6%, changed stirrup spacing is 150mm and corresponding stirrup ratio reduces to 0.4%. Fig. 3.34 shows the effect on stress-strain relation and Fig. 3.35 shows the effect on Moment-curvature curve of the hollow circular section. In both the curves, the difference is considerably larger than the case where stirrup ratio has been kept unchanged. The stress-strain curve shows that with higher stirrup spacing and lower ratio, the area under the curve

reduces and the ratio of the area is 0.827. From the Moment-curvature curve, if deflection ductility is calculated, the value is lesser for the higher stirrup spacing and the ratio of the values is 0.65 (7.194/10.94). Thus, although the stirrup spacing has less effect on the value of *R* if percentage of transverse reinforcement is kept unchanged. But if the diameter of the stirrup is not changed while changing the stirrup spacing, it will have considerable impact on the value of *R*. It can be concluded that while changing the stirrup spacing, the stirrup ratio needs to be kept unchanged in order to get least impact on the *R* value.

3.5.2. Effect of confining effective width and diameter of stirrup on *R*

Effect of confining width on *R* has been studied. Section properties that has been considered for the present study has been discussed earlier**.** In addition to outer diameter of section 16m and wall thickness 1m, three more wall thickness of 0.5m, 1.5m and 2.0m have been considered to understand the effect of confining effective width on *R*. Table 3.14 shows the results of the analysis considering ρ_s = 0.6%, ρ_{cc} = 1%, P/Af_{ck} = 0.1, S_h = 100mm, f_{ck} = 40MPa, fy = 500MPa, f_{su} = 700MPa. It has been found from the results that although effective confining coefficient (k_e) increases with wall thickness, the value of *R* not necessarily enhances accordingly. The results are fluctuating but it remains within 87% of the value of *R* with wall thickness 1m.

In order to understand this effect for other general values of ρ_s and ρ_{cc}, analysis has been done for same section sizes with ρ_s = 0.8%, ρ_{cc} = 3%, results of which are shown in Table 3.15. Similar results have also been found and the variation is about 81% of the value of *R* with wall thickness 1m.

A section size of outer diameter 10m has been considered where wall thicknesses are 0.5m, 1.0m and 1.5m. With ρ_s = 0.6%, ρ_{cc} = 1%, P/Af_{ck} = 0.1 and other parameters unchanged, analyses have been done. The results are shown in Table 3.16. From this table also, it can be found that the value of *R* does not increase with increase in k_e value. The results are fluctuating but it remains within 84% of the value of *R* for wall thickness 1m.

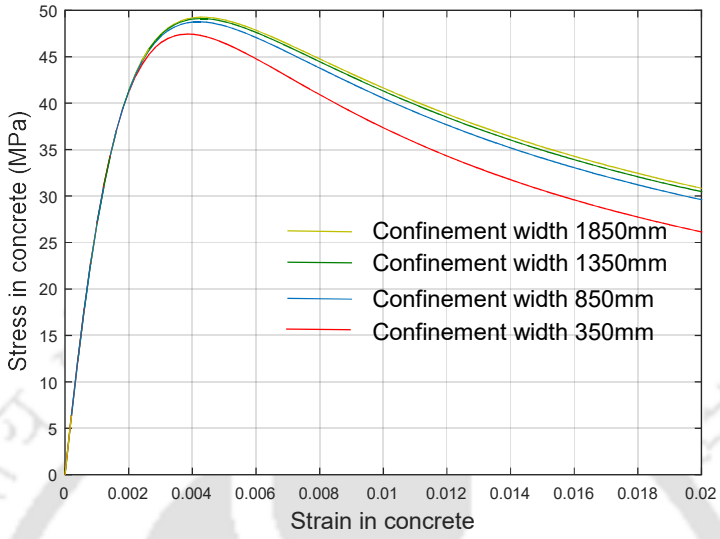

Fig. 3.36. Stress-strain curve for concrete as per Mander *et al.* (1988) for different confining width – $\rho_s = 0.6\%$, $S_h = 150$mm, $\rho_{cc} = 1\%$, $f_{ck} = 40$MPa, $fy = 500$ MPa

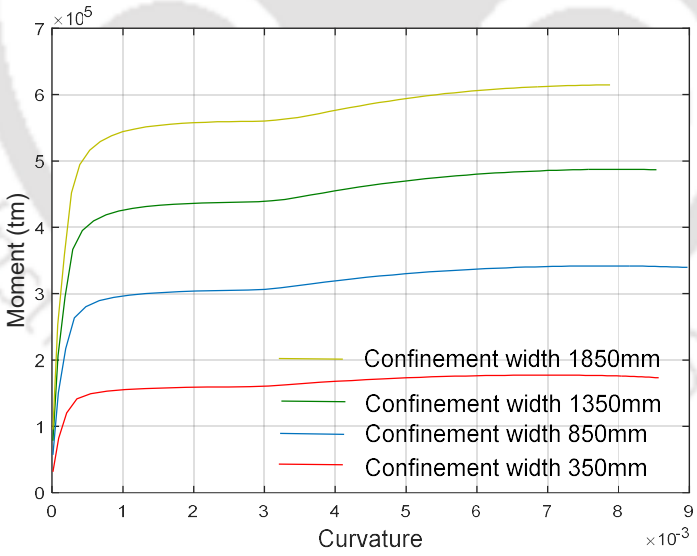

Fig. 3.37. Moment-curvature curve for circular hollow section for different confining width - $D_o = 16$m, $P/Af_{ck} = 0.1$, $\rho_s = 0.6\%$, $S_h = 100$mm, $\rho_{cc} = 1\%$, $f_{ck} = 40$ MPa, $fy =$ 500 MPa

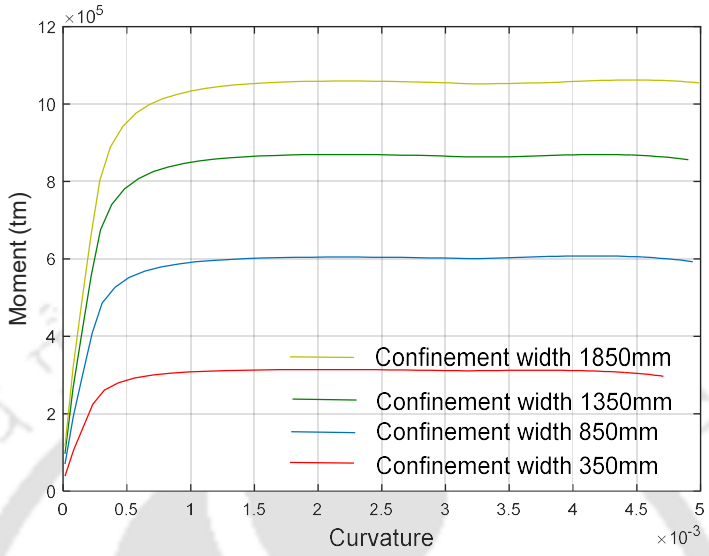

Fig. 3.38. Moment-curvature curve for circular hollow section for different confining width – D_o = 16m, P/Af_{ck} = 0.1, ρ_s = 0.8%, S_h = 100mm, ρ_{cc} = 3%, f_{ck} = 40Mpa, fy = 500MPa

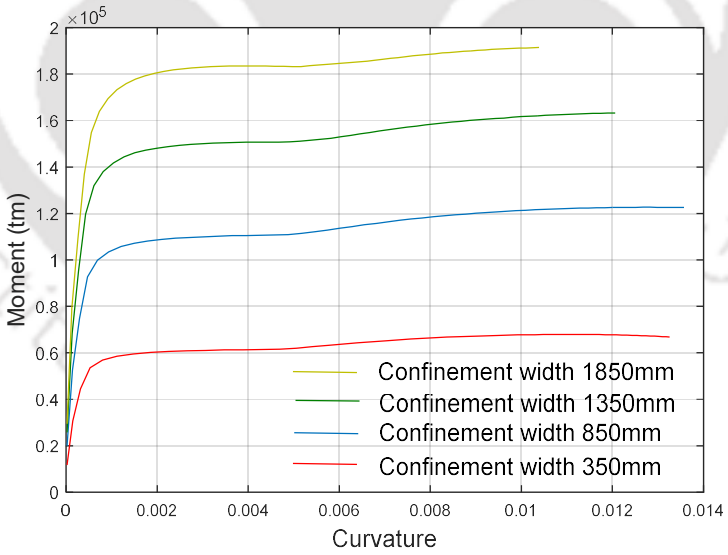

Fig. 3.39. Moment-curvature curve for circular hollow section for different confining width – D_o = 10m, P/Af_{ck} = 0.1, ρ_s = 0.6%, S_h = 100mm, ρ_{cc} = 1%, f_{ck} = 40Mpa, fy = 500MPa

Fig. 3.36 shows the effect on stress-strain relation and Fig. 3.37 to 3.39 show the Moment-curvature curves for the chosen parameters as presented in Table 3.14 to 3.16 respectively. From the curves also, it is clear that with increase in width of the wall of the hollow circular section with identical outer diameter, the moment capacity of the section increases but the curvature corresponding to the maximum moment of the section is highest for the section with wall thickness of 1m. As a result, the *R* value of the section with other wall thicknesses are less compared to that of for section with 1m wall thickness.

It has been found from the above results that the confining width value changes the *R* value of the section but there is no specific trend that can be found about its effect. In general, it is found that the values are varying between 80% and 100% for a wall thickness variation between 0.5m to 2.0m.

Table 3.14. Effect of confining width on value of deflection ductility with D_o = 16m, ρ_s = 0.6%, ρ_{cc} = 1%, P/Af_{ck} = 0.1, S_h = 100mm, f_{ck} = 40MPa, fy = 500MPa, f_{su} = 700 MPa (Ratio values calculated with respect to 1.0m wall thickness)

Wall Thickness (m)	Confined width (m)	k_e	Deflection ductility	Confined width ratio	k_e ratio	Deflection ductility ratio
0.5	0.338	0.764	9.783	0.4	0.84	0.89
1.0	0.834	0.911	10.935	1	1	1
1.5	1.330	0.950	10.539	1.59	1.04	0.96
2.0	1.828	0.967	9.500	2.19	1.06	0.87

Table 3.15. Effect of confining width on value of deflection ductility with D_o = 16m, ρ_s = 0.8%, ρ_{cc} = 3%, P/Af_{ck} = 0.1, S_h = 100mm, f_{ck} = 40MPa, fy = 500MPa, f_{su} = 700 MPa (Ratio values calculated with respect to 1.0m wall thickness)

Wall Thickness (m)	Confined width (m)	k_e	Deflection ductility	Confined width ratio	k_e ratio	Deflection ductility ratio
0.5	0.338	0.764	2.252	0.4	0.84	0.81
1.0	0.834	0.911	2.778	1	1	1
1.5	1.330	0.950	2.382	1.59	1.04	0.86
2.0	1.828	0.967	2.781	2.19	1.06	1.0

Table 3.16. Effect of confining width on value of deflection ductility with D_o = 10m, ρ_s = 0.6%, ρ_{cc} = 1%, P/Af_{ck} = 0.1, S_h = 100mm, f_{ck} = 40MPa, fy = 500MPa, f_{su} = 700 MPa (Ratio values calculated with respect to 1.0m wall thickness)

Wall Thickness (m)	Confined width (m)	k_e	Deflection ductility	Confined width ratio	k_e ratio	Deflection ductility ratio
0.5	0.338	0.764	9.604	0.4	0.84	0.93
1.0	0.834	0.911	10.316	1	1	1
1.5	1.330	0.950	8.68	1.59	1.04	0.84

In the two different sections analysed as mentioned hereinbefore, in order to keep ρ_s and S_h unchanged, diameter of the stirrup need to be reduced. The required reduction in diameter is about 50%. It has been studied that the difference in the k_e value for the change in diameter gives a ratio 0.98 (0.634/0.645) and difference in deflection ductility gives a ratio 0.999 (8.043/8.044). Thus, the effect of diameter of stirrup is almost nil.

3.5.3. Effect of grade of steel on *R*

Analysis has been done to find the effect of different grade of steel on *R*. Keeping yield strength (*YS*) as 500MPa, three different tensile strength (*TS*) or ultimate strength of value 565MPa. 625MPa and 700MPa have been considered for the analysis. The section property has been considered as defined earlier. Two different section conditions have been considered for this analysis. Both the sections are of D_o = 16m D_i = 14m, P/Af_{ck} = 0.1, S_h = 100mm, f_{ck} = 40MPa, fy = 500MPa. The variable parameters of the sections are ρ_s = 0.6%, ρ_{cc} = 1% for first section and ρ_s = 0.8%, ρ_{cc} = 3% for the second section. As per the calculation the *R* value with fsu = 700MPa for the first section is 10.935 and that of for the second section is 2.777, which suggests that first section has large ductility value. Comparative analysis has been done on these two sections for different *TS* value of steel. Fig. 3.40 and Fig. 3.41 show the moment-curvature curves for the two different sections under three different *TS* values. From Fig. 3.40 it can be seen that maximum moment for all the three *TS* values occurs corresponding to almost same curvature, however, due to higher moment capacity ductility value may differ widely. Whereas in Fig. 3.41 the curves differ very little which suggests that the ductility values for three different TS should not vary widely.

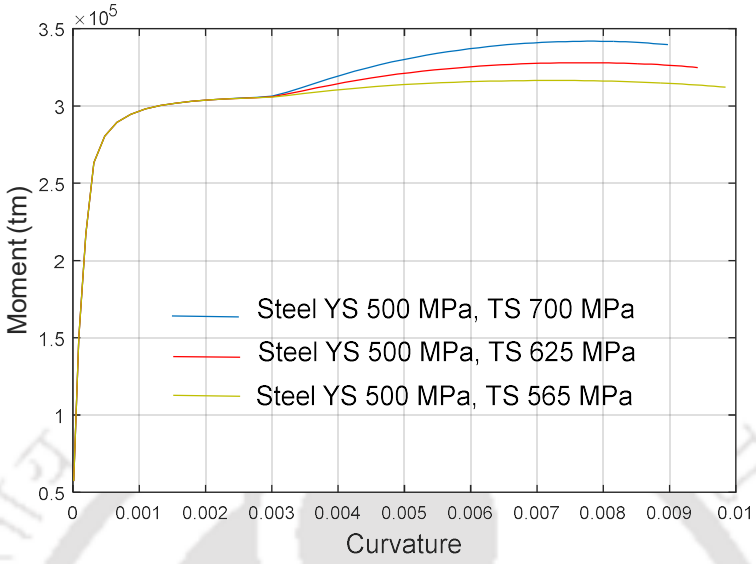

Fig. 3.40. Moment-curvature curve for circular hollow section for different grade of reinforcement steel – D_o = 16m_D_i = 14m, P/Af_{ck} = 0.1, ρ_s = 0.6%, S_h = 100mm, ρ_{cc} = 1%, f_{ck} = 40MPa, fy = 500MPa

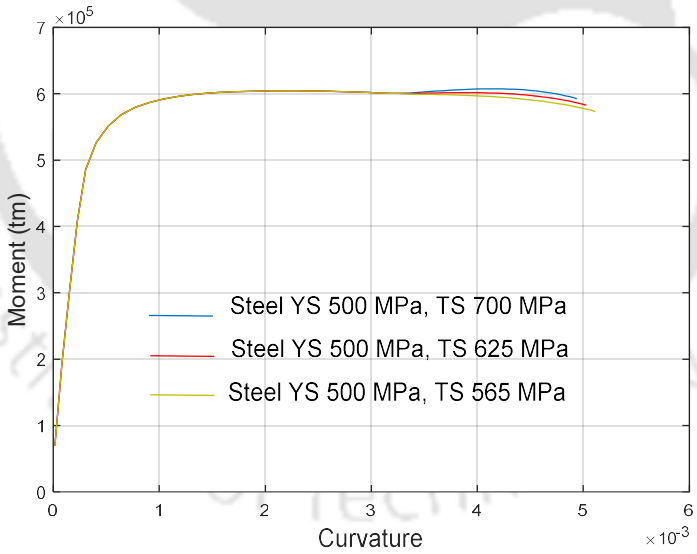

Fig. 3.41. Moment-curvature curve for circular hollow section for different grade of reinforcement steel – D_o = 16m_D_i = 14m, P/Af_{ck} = 0.1, ρ_s = 0.8%, S_h = 100mm, ρ_{cc} = 3%, f_{ck} = 40MPa, fy = 500MPa

From the analysis results, it is found that the three deflection ductility values for the first case is 10.935, 8.083 and 5.46 and for the second case it is 2.777, 2.364 & 2.363. The values vary widely in case of first section whereas it varies less in the second case. The ratio is

0.50 (5.46/10.935) for the first case and 0.85 (2.363/2.777) for the second case. Thus, it can be said that the effect of variable *TS* for grade fy500 steel may go as high as 50%.

3.5.4. Effect of grade of concrete on *R*

Analysis has been done with different grade of concrete to find the effect on *R*. In addition to M40 grade, M60 grade of concrete has been studied. Fig. 3.42 shows the stress-strain curve for concrete for two different grades and for two different ρ_s values, 0.2% and 1.0%. The ordinate shows the stress/strength ratio so that the curves can be compared. From the curves it is understood that for the falling branch, strain capacity of lower grade of concrete is higher. Fig. 3.43 shows the moment-curvature curves for five different ρ_s values, 0.2%, 0.4%, 0.6%, 0.8% and 1% and all for two different grades of concrete, M40 and M60. Table 3.17 shows the deflection ductility and *R* for different cases.

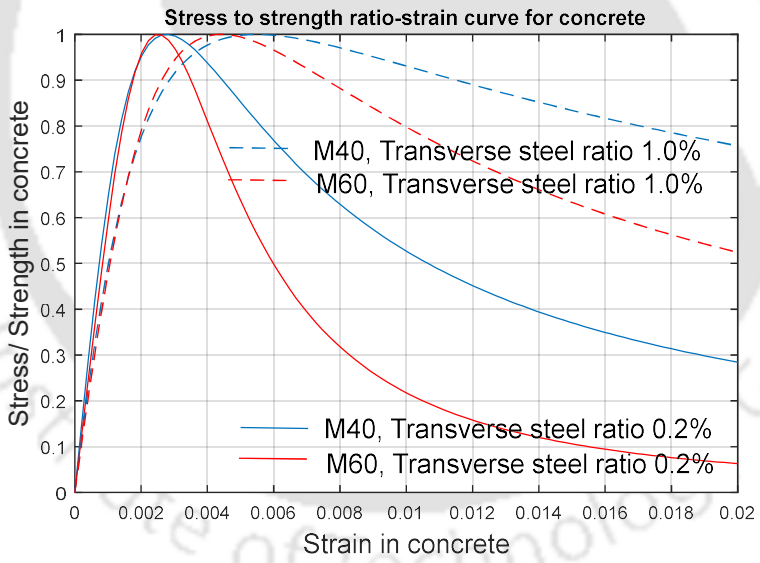

Fig. 3.42. Stress-strain curve for concrete as per Mander *et al.* (1988) for different grade of concrete and different ρ_s . S_h = 100mm, ρ_{cc} = 1%, fy = 500MPa

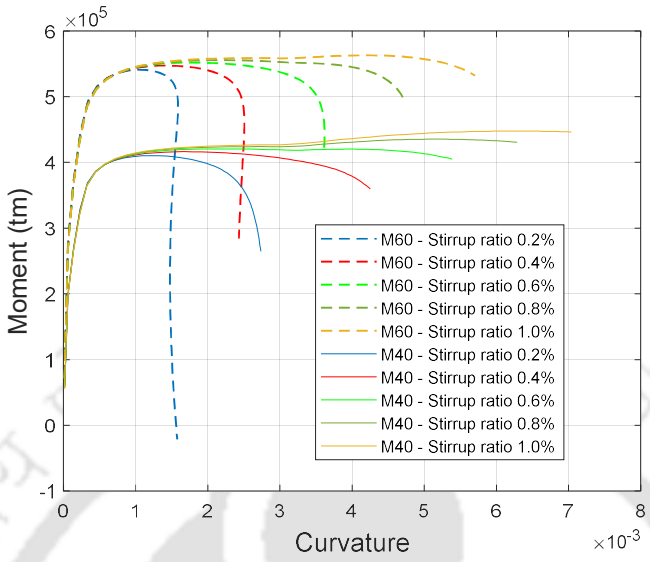

Fig. 3.43. Moment-curvature curve for circular hollow section for different grade of concrete and different ρ_s (0.2, 0.4, 0.6, 0.8, 1.0%, values correspond to increasing curvature) – D_o = 16m, D_i = 14m, P/Af_{ck} = 0.2, S_h = 100mm, ρ_{cc} = 1%, fy = 500MPa.

Table 3.17. Deflection ductility and R for different ρ_s values and different grade of concrete for section with D_o = 16m, D_i = 14m, ρ_{cc} = 1%, S_h = 100mm, P/Af_{ck} = 0.2, fy = 500MPa, f_{su} = 700 MPa

ρ_s	M40			M60		
	Deflection ductility	Reserve strength factor	R	Deflection ductility	Reserve strength factor	R
0.2%	1.97	1.2	2.37	1.90	1.16	2.20
0.4%	2.21	1.2	2.64	2.09	1.16	2.41
0.6%	2.41	1.2	2.88	2.26	1.16	2.63
0.8%	4.24	1.2	5.08	2.42	1.16	2.87
1.0%	5.92	1.2	7.09	3.03	1.16	3.52

From Table 3.17, it is found that the ratio of the R values for two different grades of concrete for lower ρ_s is about 0.9 whereas for higher ρ_s it is about 0.5. From the Moment-curvature curves in Fig. 3.43, it can be seen that moment capacity of the section with higher grade of concrete is naturally higher. The maximum moment capacity occurring at almost same curvature for both the grade of concrete against ρ_s value up to 0.6%, while for ρ_s value higher than 0.6%, maximum moment capacity occurring for M40 grade are at relatively

higher curvature. As a result, the deflection ductility values are much higher for M40 grade for these higher ρ_s value.

3.5.5. Effect of slenderness of structure on *R*

It has been found that the slenderness of structure affects the deflection ductility as due to the P-Δ effect, additional moments in the section gets induced thus corresponding to the ultimate curvature which provides the deflection ductility, a negative stiffness effect is induced which causes failure. In order to avoid this situation, ultimate curvature should be considered lesser than the capacity of the section which will reduce the value of deflection ductility. In the present case the structure which has been studied corresponds to slender ness ratio (L_{eff}/r), i.e. effective length/ radius of gyration of the section) just less than 50 and it is found that negative stiffness effect has not occurred. The structures having slenderness value more than 50 will have less deflection ductility than the structures with slenderness value less than 50.

3.5.6. Effect of transverse steel ratio(ρ_s), main steel ratio (ρ_{cc}) and vertical load (P/Afck) on *R*

Analysis has been done for section parameters as defined earlier. Fig. 3.44 to 3.46 show the M-ϕ curves for different sections of various parameters. From the curves it is clear that with higher ρ_s value the section can take more curvature. With higher values of axial load (P/Af_{ck}) the moment capacity of the section increases but the capacity of taking curvature reduces. Similarly, with higher values of ρ_{cc} the moment capacity of the section increases but the capacity of taking curvature reduces. Interesting point can be noted that with increase in ρ_{cc} the curve patterns remain same. The curves for ρ_{cc} = 4% have not been shown for the same reason.

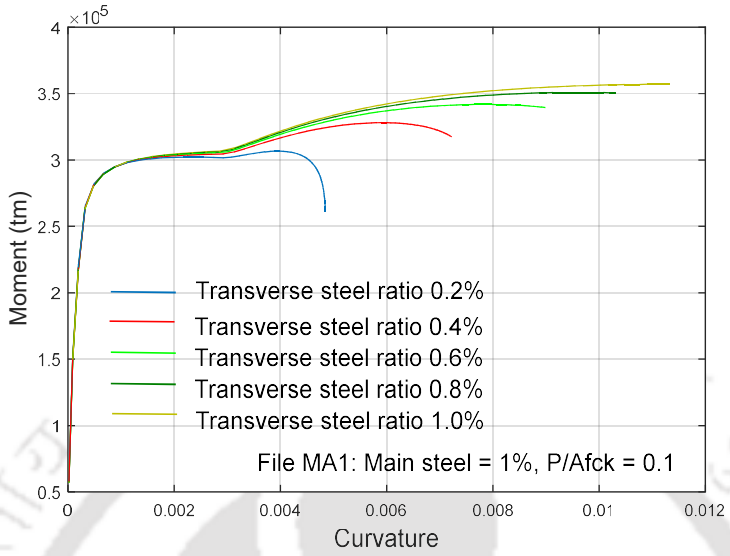

(a)

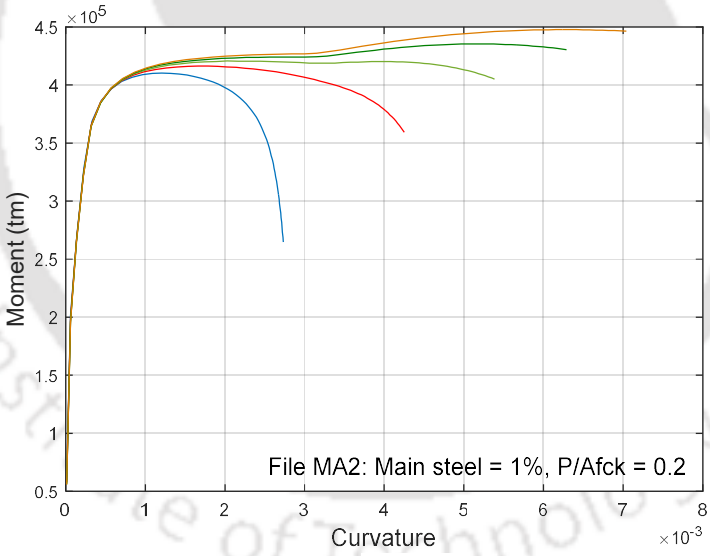

(b)

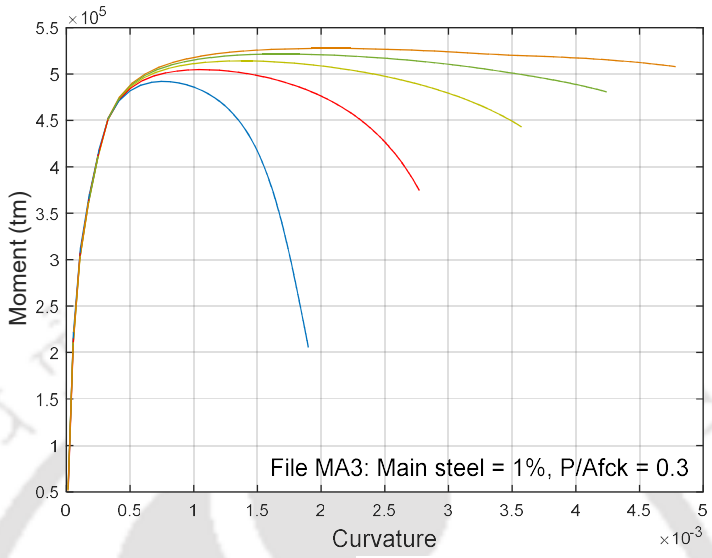

(c)

Fig. 3.44. (a), (b), (c) Moment-curvature curve for circular hollow section for different ρ_s (0.2, 0.4, 0.6, 0.8, 1.0 %,) and different P/Af_{ck} (0.1, 0.2, 0.3), - D_o = 16m, D_i = 14m, S_h = 100mm, ρ_{cc} = 1%, f_y = 500MPa, f_{ck} = 40 MPa

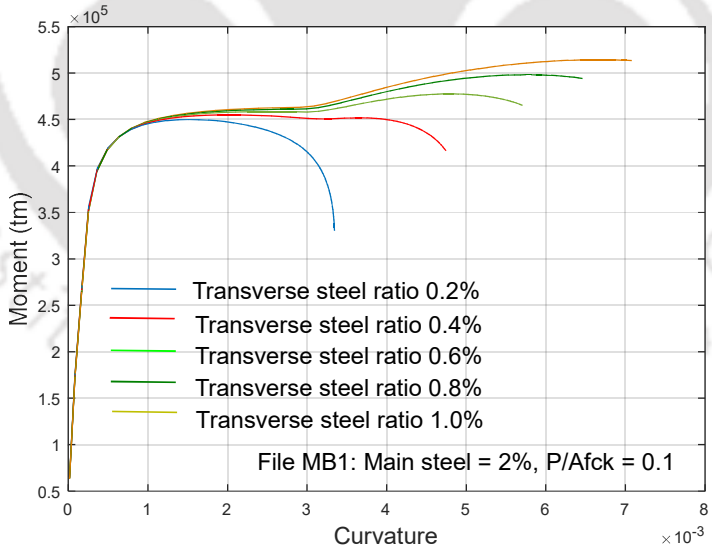

(a)

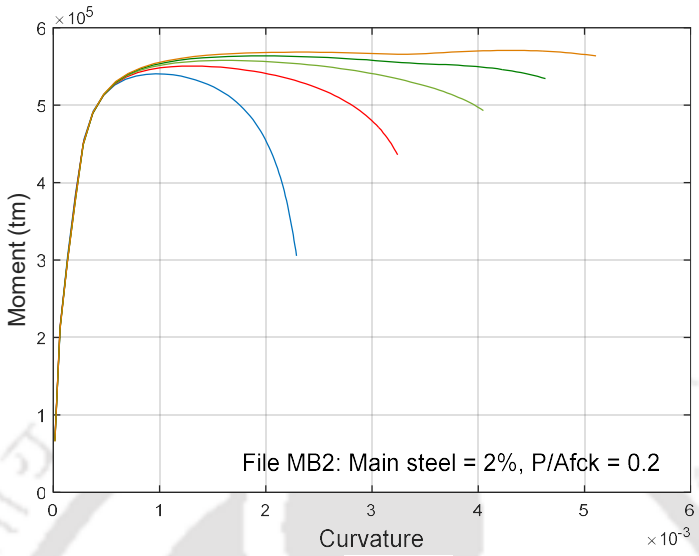

(b)

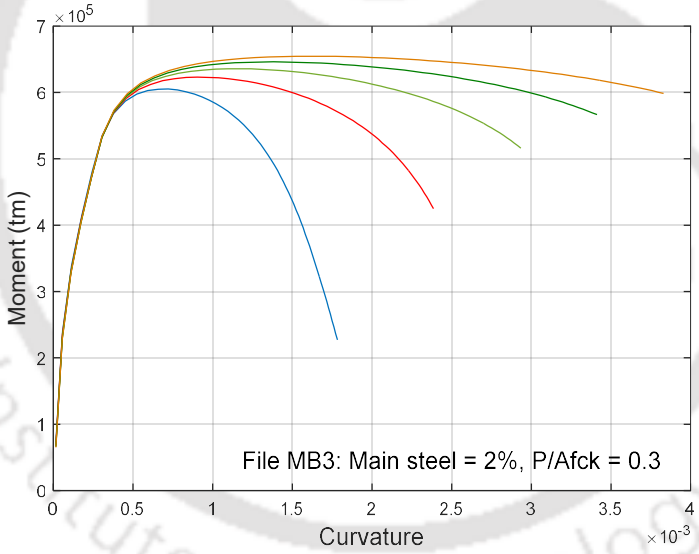

(c)

Fig. 3.45. (a), (b), (c) Moment-curvature curve for circular hollow section for different ρ_s (0.2, 0.4, 0.6, 0.8, 1.0 %,) and different P/Af_{ck} (0.1, 0.2, 0.3), - D_o = 16m, D_i = 14m, S_h = 100mm, ρ_{cc} = 2%, f_y = 500MPa, f_{ck} = 40 MPa

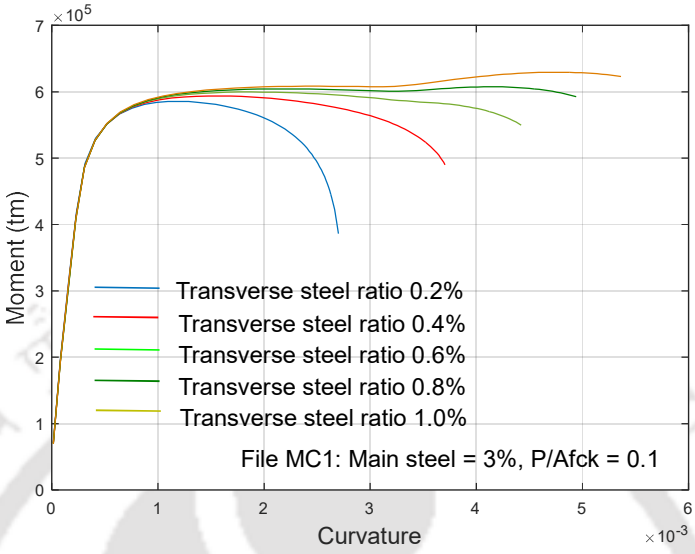

(a)

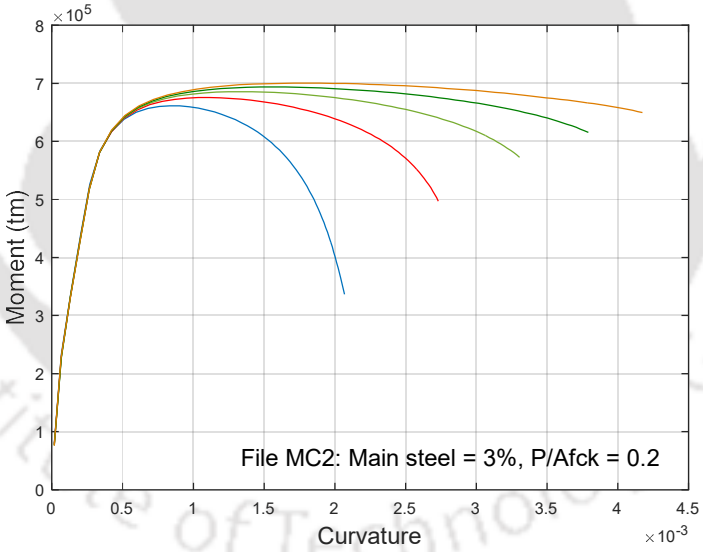

(b)

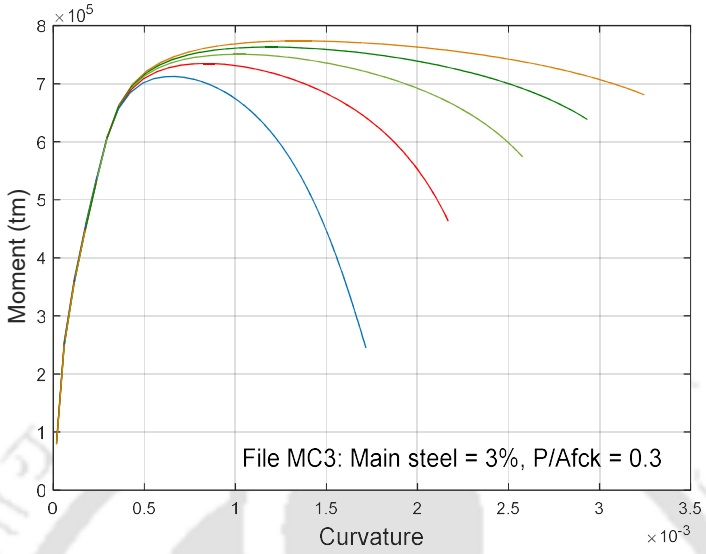

(c)

Fig. 3.46. (a), (b), (c) Moment-curvature curve for circular hollow section for different ρ_s (0.2, 0.4, 0.6, 0.8, 1.0 %,) and different P/Af_{ck} (0.1, 0.2, 0.3), - D_o = 16m, D_i = 14m, S_h = 100mm, ρ_{cc} = 3%, f_y = 500MPa, f_{ck} = 40 MPa

Summary of the results of deflection ductility and response reduction factors are shown in Table 3.18 to 3.20. The values of R shown in the table has been represented graphically in Fig. 3.47.

Table 3.18. Deflection ductility and R for different ρ_s and ρ_{cc} values for P/Af_{ck} = 0.1 for section with D_o = 16m, D_i = 14m, S_h = 100mm, fy = 500MPa, f_{su} = 700 MPa, f_{ck} = 40 MPa

ρ_s	ρ_{cc} = 1%			ρ_{cc} = 2%			ρ_{cc} = 3%			ρ_{cc} = 4%		
	D	*O*	*R*	*D*	*O*	*R*	*D*	*O*	*R*	*D*	*O*	*R*
0.2%	3.4	1.28	4.4	2.15	1.42	3.1	1.96	1.49	2.9	1.85	1.53	2.8
0.4%	7.66	1.28	9.8	2.33	1.42	3.3	2.12	1.49	3.2	1.98	1.54	3.0
0.6%	10.94	1.28	14.0	4.57	1.42	6.5	2.25	1.49	3.4	2.08	1.54	3.2
0.8%	13.41	1.28	17.1	6.69	1.43	9.5	2.78	1.49	4.1	2.17	1.54	3.3
1.0%	15.27	1.28	19.5	8.46	1.43	12.1	4.13	1.49	6.2	2.25	1.54	3.5

Note: D = Deflection Ductility, O = Reserve strength factor

Table 3.19. Deflection ductility and R for different ρ_s and ρ_{cc} values for $P/Af_{ck} = 0.2$ for section with D_o = 16m, D_i = 14m, S_h = 100mm, fy = 500MPa, f_{su} = 700 MPa, f_{ck} = 40 MPa

ρ_s	ρ_{cc} = 1%			ρ_{cc} = 2%			ρ_{cc} = 3%			ρ_{cc} = 4%		
	D	*O*	*R*	*D*	*O*	*R*	*D*	*O*	*R*	*D*	*O*	*R*
0.2%	1.97	1.20	2.4	1.80	1.30	2.3	1.67	1.38	2.3	1.61	1.42	2.3
0.4%	2.21	1.20	2.6	1.97	1.30	2.6	1.81	1.38	2.5	1.73	1.42	2.5
0.6%	2.41	1.20	2.9	2.11	1.30	2.7	1.92	1.38	2.7	1.83	1.42	2.6
0.8%	4.24	1.20	5.1	2.24	1.30	2.9	2.03	1.38	2.8	1.92	1.42	2.7
1.0%	5.92	1.20	7.1	2.69	1.31	3.5	2.12	1.38	2.9	1.99	1.42	2.8

Note: D = Deflection Ductility, O = Reserve strength factor

Table 3.20. Deflection ductility and R for different ρ_s and ρ_{cc} values for $P/Af_{ck} = 0.3$ for section with D_o = 16m, D_i = 14m, S_h = 100mm, fy = 500MPa, f_{su} = 700 MPa, f_{ck} = 40 MPa

ρ_s	ρ_{cc} = 1%			ρ_{cc} = 2%			ρ_{cc} = 3%			ρ_{cc} = 4%		
	D	*O*	*R*	*D*	*O*	*R*	*D*	*O*	*R*	*D*	*O*	*R*
0.2%	1.55	1.16	1.8	1.49	1.24	1.8	1.44	1.30	1.9	1.40	1.35	1.9
0.4%	1.74	1.16	2.0	1.64	1.24	2.0	1.56	1.31	2.0	1.52	1.35	2.1
0.6%	1.92	1.16	2.2	1.77	1.24	2.2	1.67	1.31	2.2	1.61	1.35	2.2
0.8%	2.07	1.16	2.4	1.89	1.25	2.4	1.76	1.31	2.3	1.69	1.35	2.3
1.0%	2.22	1.16	2.6	2.00	1.25	2.5	1.85	1.31	2.4	1.76	1.36	2.4

Note: D = Deflection Ductility, O = Reserve strength factor

A summary of R value is shown in Table 3.21 for the case under consideration. Minimum and maximum ρ_s value and corresponding R values are tabulated. From the graphs shown in Fig. 3.47 it can be said that the variation of R with respect to ρ_s is generally linear except for few cases like the curve for $P/Af_{ck} = 0.1$ & $\rho_{cc} = 2\%$; $P/Af_{ck} = 0.2$ & ρ_{cc} =1%. For these cases a modification has been suggested in the Table 3.21 so that linear interpolation can be done for any intermediate value of ρ_s maintaining a safe R value.

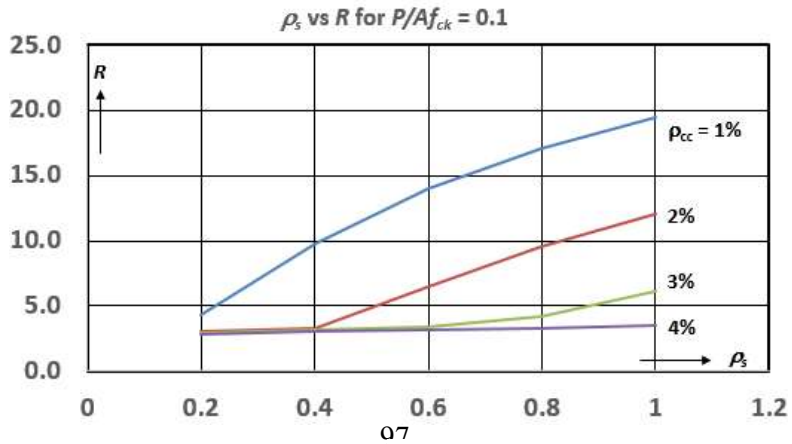

97

(a)

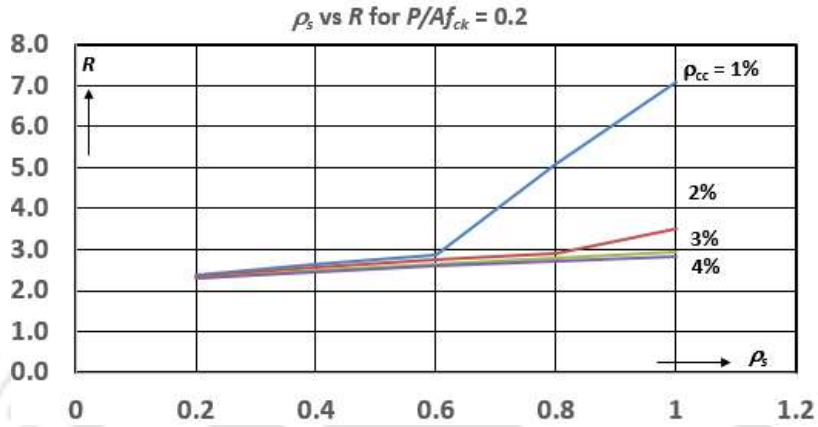

(b)

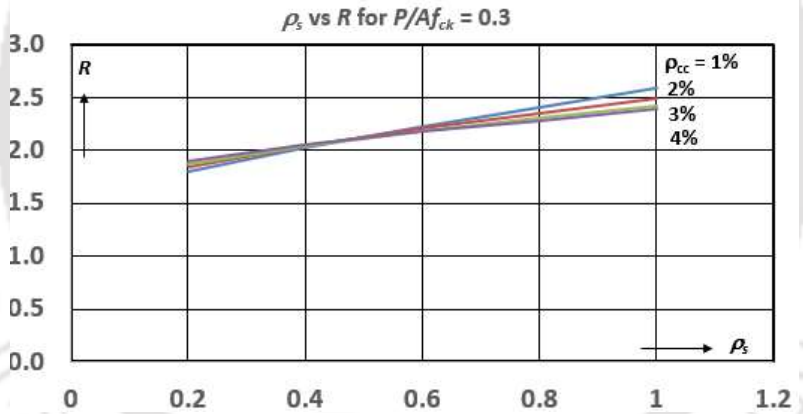

(c)

Fig. 3.47. (a), (b), (c) Transverse steel ratio (ρ_s) *vs* Response reduction factor I for circular hollow section for different main steel ratio (ρ_{cc}) and Vertical load (P/Af_{ck}) - D_o = 16m, D_i = 14m, S_h = 100mm, f_{ck} = 40MPa, f_y = 500MPa, , f_{su} = 700Mpa, f_{ck} = 40 MPa

Table 3.21. Summary of R value for section with D_o = 16m, D_i = 14m, S_h = 100mm, fy = 500Mpa, f_{su} = 700 MPa

	ρ_{cc} = 1%	ρ_{cc} = 2%	ρ_{cc} = 3%	ρ_{cc} = 4%
P/Af_{ck} = 0.1				
ρ_s = 0.2%	4.4	3.1	2.9	2.8
ρ_s = 1.0%	19.5	6.2	6.2	3.5
P/Af_{ck} = 0.2				
ρ_s = 0.2%	2.4	2.3	2.3	2.3
ρ_s = 1.0%	3.5	3.5	2.9	2.8
P/Af_{ck} = 0.3				
ρ_s = 0.2%	1.8	1.8	1.9	1.9
ρ_s = 1.0%	2.6	2.5	2.4	2.4

Considering the effect of varying effective section property for which R values can be enhanced by 12% as discussed in Section 3.4.7, a generalised R value can be considered by multiplying the values in Table 3.21 by 0.8 (for confining width effect, refer Section 3.5.2) x 1.12 (for varying effective section property) = 0.9. The values are shown in Table 3.22. For ρ_s between 0.2 & 1% and P/Af_{ck} between 0.1 & 0.2, 0.2 & 0.3, the values can be interpolated.

Table 3.22. Recommended value of R for large diameter hollow circular section with wall thickness varying between 500mm and 2000mm, Grade of steel fy500, f_{su} = 700MPa, maximum grade of concrete M40

	ρ_{cc} = 1%	ρ_{cc} = 2%	ρ_{cc} = 3%	ρ_{cc} = 4%
P/Af_{ck} = 0.1				
ρ_s = 0.2%	4.0	2.8	2.6	2.5
ρ_s = 1.0%	5.5	5.5	5.5	3.0
P/Af_{ck} = 0.2				
ρ_s = 0.2%	2.2	2.0	2.0	2.0
ρ_s = 1.0%	3.0	3.0	2.6	2.5
P/Af_{ck} = 0.3				
ρ_s = 0.2%	1.6	1.6	1.7	1.7
ρ_s = 1.0%	2.3	2.2	2.2	2.2

The calculated value of R corresponding to P/Af_{ck} = 0.1, ρ_{cc} = 1% and ρ_s = 1.0% in Table 3.22 comes to 17.1. However, for all practical purposes, such high value of R gives rise to deflection of the cantilever pier top beyond functional requirement like avoidance of

pounding etc and thus a practicable value keeping in parity with the other values of R obtained has been suggested. Thus, the recommended value of R for large diameter hollow circular section for grade of concrete up to M40 and grade of steel Fe500 with UT 700 MPa can be obtained from Table 3.22. The actual theoretical value of R as per the theory described in this chapter can be obtained from the graphs in Fig. 3.47 multiplied by the factor 0.9.

3.6. Effect of opening in the wall of hollow circular section on *R*

Wall openings in hollow circular pier section is necessary for inspection purpose. Corresponding response reduction factor is likely to be lesser compared to the section with no wall opening and the same has been discussed in the present section. M-ϕ curve has been generated considering the effect of opening in the section. It has been found that the stress-strain relation of Mander *et al*. (1988) with the proposed k_e value as per Eq. 3.49 can be used for hollow circular section with wall opening with reduced strain capacity (up to 0.01) as shown in Fig. 3.27. Thus, the M-ϕ curve has been generated using the stress-strain relation of concrete as per Mander *et al*. (1988). The R value of the section has been proposed in such a way that the maximum strain in concrete remains within 0.01.

Following cases have been studied:

Case 1: $P/Af_{ck} = 0.1$, $\rho_{cc} = 1\%$, $\rho_s = 0.2\%$
Case 2: $P/Af_{ck} = 0.1$, $\rho_{cc} = 1\%$, $\rho_s = 1.0\%$
Case 3: $P/Af_{ck} = 0.2$, $\rho_{cc} = 2\%$, $\rho_s = 0.2\%$
Case 4: $P/Af_{ck} = 0.2$, $\rho_{cc} = 2\%$, $\rho_s = 1.0\%$
Case 5: $P/Af_{ck} = 0.3$, $\rho_{cc} = 1\%$, $\rho_s = 0.2\%$
Case 6: $P/Af_{ck} = 0.3$, $\rho_{cc} = 4\%$, $\rho_s = 1.0\%$

The Deflection ductility values of the section for the cases as mentioned above have been shown in Table 3.23. The ratio of deflection ductility with respect to the values corresponding to no wall opening case has been shown in Table 3.24.

Table 3.23. Deflection ductility corresponding to different opening size in hollow circular section with D_o = 16m, D_i = 14m, S_h = 100mm, fy = 500MPa, f_{su} = 700 MPa, f_{ck} = 40 MPa

Opening size (In degree)	Case 1	Case 2	Case 3	Case 4	Case 5	Case 6
0	3.40	15.27	1.80	2.69	1.55	1.76
8	2.43	13.57	1.53	2.47	1.47	1.70
16	2.30	11.89	1.45	2.31	1.41	1.65

Table 3.24. Ratio of Deflection ductility corresponding to different opening size in hollow circular section with D_o = 16m, D_i = 14m, S_h = 100mm, fy = 500MPa, f_{su} = 700 MPa, f_{ck} = 40 MPa

Opening size (In degree)	Case 1	Case 2	Case 3	Case 4	Case 5	Case 6
0	1.00	1.00	1.00	1.00	1.00	1.00
8	071	0.89	0.85	0.92	0.95	0.97
16	0.68	0.78	0.81	0.86	0.91	0.94

From the Table 3.24, it can be found that for Case 1, the ratio of deflection ductility varies from 1 to 0.68 and for Case 2, the ratio varies from 1.0 to 0.78 for ρ_s value between 0.2% and 1%. A general variation value from 1.0 to 0.7 for the case P/Af_{ck} = 0.1 may be considered for simplification.

Similarly, for Case 3 and Case 4, the ratio varies from 1 to 0.81 and from 1 to 0.86 respectively for ρ_s value between 0.2% and 1%. A general variation value from 1.0 to 0.8 may be considered for the case P/Af_{ck} = 0.2 for simplification

Similarly, for Case 5 and Case 6, the ratio varies from 1 to 0.91 and from 1 to 0.94 respectively for ρ_s value between 0.2% and 1%. A general variation value from 1.0 to 0.9 may be considered for the case P/Af_{ck} = 0.3 for simplification.

Table 3.25 proposes the multiplication factors which are to be applied on the values shown in Table 3.22 to get the value of R for section with wall opening. Opening size 0 degree corresponds to the section with no wall opening and corresponding to this the multiplication factor is 1. The values of multiplication factor shown in Table 3.25 may be interpolated for

any opening size between 0 and 16 degree. The degree of opening is the angle subtended by opening size with respect to the radius of the circular section.

Table 3.25. Multiplication factor for *R* for pier with hollow section with opening

P/Af_{ck}	Opening size 0 degree	Opening size 16 degree
0.1	1	0.7
0.2	1	0.8
0.3	1	0.9

3.7. Concluding remarks

In this chapter, a detailed discussion has been presented on the assessment of response reduction factor *R* for large diameter hollow circular section. These types of sections are generally used for bridges with tall pier in high seismic zone. The values of *R* have been found to be dependent on different parameters namely, axial load (P/Af_{ck}), main steel ratio (ρ_{cc}) and transverse steel ratio (ρ_s) and the values are accordingly proposed. Opening in wall in hollow circular pier section is essential for inspection purpose. The present study proposes the values of *R* for both the cases, i.e. section without wall opening and section with wall opening. The proposed values are applicable for non-slender pier (slenderness ratio within 50) and grade of concrete up to M40.

The stress-strain curve has been used following Mander *et al*. (1988). The confinement effective coefficient (k_e) for hollow circular section has been proposed, which has been substantiated by detailed FEA. No such recommendation is found for confinement effective coefficient (k_e) for hollow circular section in the literature.

Ultimate strain in concrete has been estimated from strain energy balance approach of the concrete section at which first fracture occurs at confining steels as suggested by Mander *et al.* (1988). It has been found that the concrete strain corresponding to the ultimate moment capacity of the sections under study lies within this ultimate concrete strain. In case of hollow circular section with wall opening, ultimate concrete strain is less than that of section without opening. Thus, the *R* value of section with opening has been proposed in such a way that the concrete strain remains with in this reduced ultimate concrete strain capacity.

It has been found that confining width on displacement ductility has significant effect. The effect of change in confining width on the value of R, however, cannot be established. R values are observed to vary from 80% to 100% for wall thickness varying between 0.5m and 2.0m, when compared with the value for 1m wall thickness. Suitable reduction factor has been recommended in the proposed R so that the same can be used in general for all wall thicknesses.

The spacing of stirrup has significant effect on the value of R. It has been found that stirrup spacing above 150 mm causes drastic reduction in ductility of any section. In general, 100 mm spacing of stirrup in special confining zone, where plastic hinge may be formed has been recommended in all the standards/codes and the same has been used in the present study. It has been found that the diameter of stirrup with identical transverse steel ratio (ρ_s) has insignificant effect on R so long the stirrup spacing is below 150mm.

For section where slenderness ratio of pier is more than 50, ductility reduces drastically due to P-Δ effect. Grade of concrete has significant effect on the ductility of any section if transverse steel ratio (ρ_s) is high. The strain carrying capacity of high strength concrete is much lesser compared to that of M40 grade and results in reduction in ductility of the section.

In general, in different codes/ standards, unique value of R for different components of structure are recommended. As such the codes/ standards do not recommend the R value of hollow circular section and for design of bridges the values recommended for solid sections are used for hollow circular pier section. If the values obtained in the present study is compared with the code/ standards recommended values, then it can be found that for some cases, the code recommended values are either over safe whereas in some other cases the values are inadequate. As such, the unique recommended value in the code does not cover all the cases under which a structure may undergo. Thus, an attempt has been made to propose R value for piers with hollow circular section, with or without wall opening, covering some of the possible variations in design parameters.

The value of R increases with increase in transverse steel ratio (ρ_s), with decrease in vertical load (P/Af_{ck}) and with decrease in main steel ratio (ρ_{cc}). The proposed value of R varies

from maximum 5.5 to minimum 1.6 depending on the factors as mentioned. Thus, the code recommended *R* value which is 3 (As per IRS, BIS and IRC) irrespective of other depending parameters is not compatible with the actual behaviour and detailing of the structure as observed in the present study. The recommended *R* values of hollow circular section with door opening reduces with opening size and the reduction varies from 1 to 0.7 times of the value of *R* corresponding to section without door opening.

Chapter 4

Asynchronous motion and its effect on response of tall railway bridges

4.1. Introduction

This study is related to the assessment of seismic performance of a long multi-span railway bridge with OWG superstructure, located in the highest seismic zone of India. Piers are very tall with heights varying from 60 to 140 m. In a long bridge, spatial variation in the input seismic excitation should be considered and the effect of such varied excitation at different pier foundation level on the seismic performance of the overall bridge should be assessed. A detailed finite element model with soil-structure interaction is considered. Asynchronous ground motions are modelled using conditional simulation by considering the coherency losses and a time delay of arrival with change in phase as well as amplitude of the earthquake signals from origin to the spatial points of interest along the bridge. Multi-support excitation of the bridge is performed by converting the acceleration time history to displacement time history with reduced time step. The responses at different pier locations for the synchronous and asynchronous motion are evaluated and the requirement of asynchronous input in multi-support excitation for long bridge with tall piers are observed to be significant for assessment of safety of running train through the bridge.

4.2. Analysis of long bridge under asynchronous motion

It is understood from the literature survey and from logical inference that the asynchronous motion may cause enhanced relative motion in pier top in multi support long bridge as compared to synchronous motion. In railway bridge, this effect may lead to serious disturbance to the running train due to relative displacement of the continuous rail over piers. Thus, a detailed study is presented to appreciate the influence of synchronous and asynchronous seismic ground motion on any possibilities of change in track alignment during seismic event.

4.2.1 Modelling of the bridge under consideration

The bridge under consideration is a railway bridge with open web girder superstructure. The bridge is located in Manipur, India, which has the highest seismicity in the country. The total length of the bridge is 703 m, which comprises of eight simply supported spans. It has two 69 m span with through type OWG girder, five numbers of 103.5 m span with through type OWG girder and a plate girder span of 28.5 m. The bridge consists of seven intermediate annular piers of height ranging from 60 m to 141 m. The tall Piers resting on pile foundations are flexible and are to be modelled appropriately to represent their actual behaviour. The piles are of 1.5m diameter and their length varies between 22m to 30m depending on the location of pier on hill slope or on river bed. Fig. 4.1 shows the overall configuration of the bridge. The OWG superstructure members are modelled with beam element as per their actual cross section wherein appropriate releases are made to ensure only axial degrees of freedom to the chord members. Rotational degrees of freedom are released for stringers and cross girders to ensure shear transfer only without transferring moment. Hollow piers are modelled with beam elements, while plate elements are used to model the pile caps. All the superstructure spans are simply supported and boundary conditions are imposed with help of body constraints in SAP 2000 Nonlinear. The near-field soil is modelled using Beam on Winkler Foundation, where soil elements are modelled as discrete non-linear springs as specified in API (2008). The soil resistance in the lateral and axial direction of the pile are summarized as *P-y* curve to represent the relationship between the lateral resistance of soil and pile displacement, *t-z* curve to represent the relationship between shaft skin frictional force and relative movement of the pile with respect to the soil, *Q-z* curve to represent the mobilized tip bearing capacity and settlement. The detailed finite element model of the considered bridge along with soil-pile system is shown in Fig. 4.2.

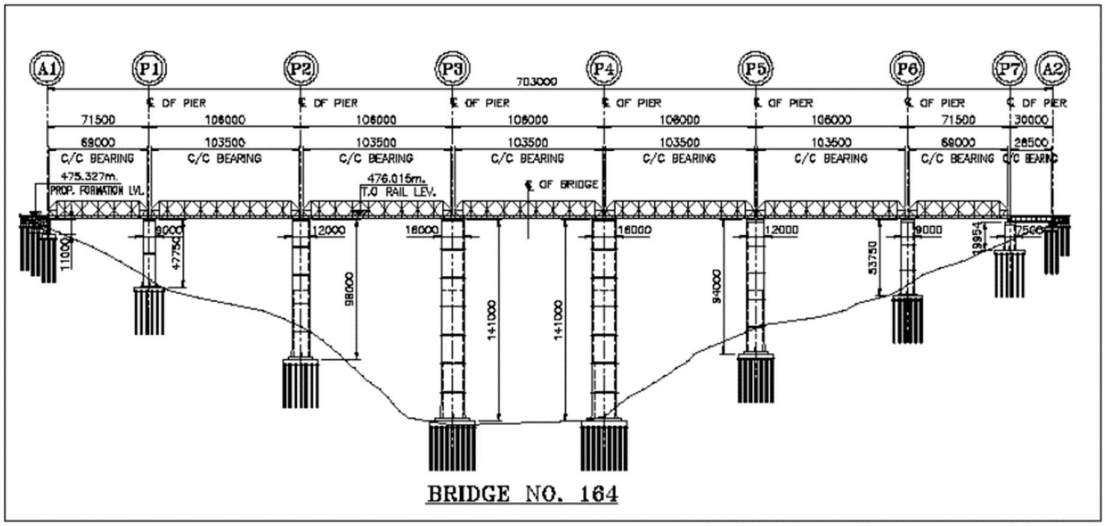

Fig. 4.1. Tall long railway bridge in Manipur

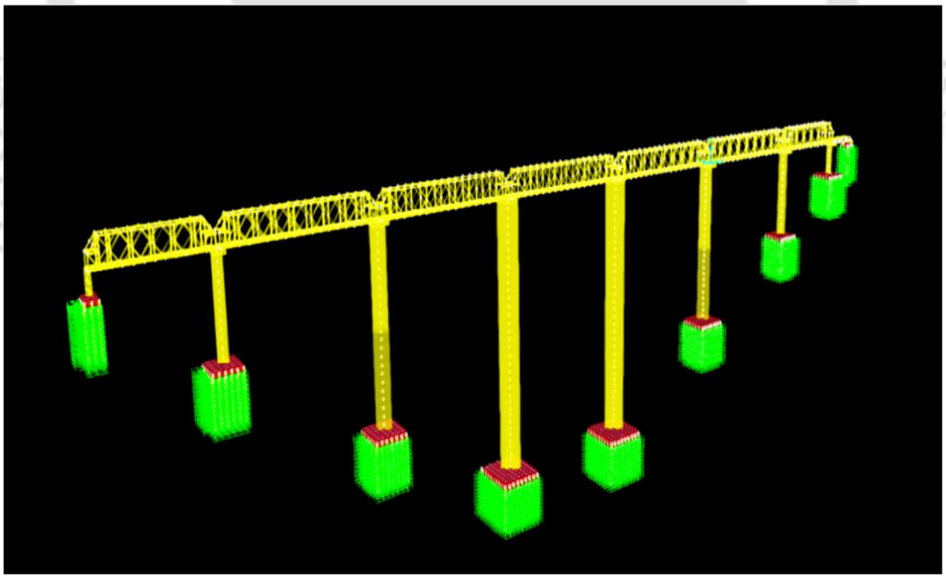

Fig. 4.2. Finite Element model of the bridge with Near-field soil springs

4.2.2 Generation of Asynchronous motion

According to the spectral representation theorem, if the ground motion at a point x_i is a homogeneous mean-square continuous real-time process $z_i(t)$, then it can be expressed as a sum of the independent sinusoidal process as

$$z_i(t) = \sum_{k=1}^{K-1}[A_{ik}\cos\omega_k(t) + B_{ik}\sin\omega_k(t)] \quad (4.1)$$

At K discrete frequencies, each separated by $\Delta\omega$. The random coefficients A_{ik} and B_{ik} are mean zero, implying that the resultant process $z_i(t)$ is also mean zero. From the point of view of simulation, it is convenient to discretize time and generate $z_i(t_j)$ at the time t_j= $j\Delta t$, j = 0,1,2……, $K-1$. In this case, the coefficients A_{ik} and B_{ik} are related to $z_i(t_j)$ through discrete Fourier transform (DFT),

$$A_{ik} = \frac{1}{K}\sum_{j=0}^{K-1} z_i(t_j)\cos\left(\frac{2\pi kj}{K}\right) \quad (4.2)$$

$$B_{ik} = \frac{1}{K}\sum_{j=0}^{K-1} z_i(t_j)\sin\left(\frac{2\pi kj}{K}\right) \quad (4.3)$$

Where Δt=$t_f/(K-1)$, $\omega_k = k\Delta\omega$, $\Delta\omega = 2\pi/(K\Delta t)$, k = 0,1,….. K-1. And t_f is the time duration of the process $z_i(t)$. The following symmetry conditions about the Nyquist frequency, $\omega_{\frac{k}{2}} = {}^{\pi}/_{\Delta t}$, apply to the Fourier coefficients A_{ik} and B_{ik} when the process $z_i(t_j)$ is real,

$$A_{ik} = A_{i,K-k} \text{ and } B_{ik} = B_{i,K-k} \quad \text{for } k = 1,2,\ldots.K/2 \quad (4.4)$$

It can be shown that by making use of the Eq, 4.2 & Eq. 4.3 and the symmetry conditions from Eq. 4.4 the covariance $c_{ij}(\omega_k) = E[A_{ik}A_{jk}] = E[B_{ik}B_{jk}]$ where A & B are mutually independent between coefficients at two spatial points x_i and x_j can be written as in Eq. 4.5 by Fenton *et al.* (1991).

$$c_{ij} = \begin{cases} \frac{1}{2}\rho_{wk}(\gamma_{ij})G(\omega_k)\Delta\omega, & for\ k = 0 \\ \frac{1}{4}\{\rho_{w,k}(\gamma_{ij})G(\omega_k) + \rho_{w,K-k}(\gamma_{ij})G(\omega_{K-k})\}\Delta\omega, & for\ k = 1,2,\ldots\ldots\frac{K}{2}-1. \\ \rho_{wk}(\gamma_{ij})G(\omega_k)\Delta\omega, & for\ k = K/2 \end{cases} \quad (4.5)$$

Where γ_{ij}=x_i-x_j is the relative position vector, $G(\omega_k)$ is the one-sided "point" spectral density function, and $\rho_{wk}(\gamma_{ij})$ is the frequency-dependent spatial correlation function. The above relationships implicitly assume that the ground motion is statistically homogenous both in space and time.

Consider now the simulation of earthquake ground motion at a set of $'m'$ target unknown points x_β given that some motions have been recorded at a set of $n = N - m$ recording

known points x_α, where N is the total number of spatial locations under consideration. Using Eq. 4.5, the NxN covariance matrix $C_k = [C_{ij}(\omega_k)]$, i,j = 1,2,……n,……$n+m$, for each Fourier frequency,ω_k, k = 0,1,…..$^{K}/_{2}$. can be assembled and expressed as the symmetric matrix.

$$c_k = \begin{bmatrix} c_{\alpha\alpha} & c_{\alpha\beta} \\ c_{\alpha\beta} & c_{\beta\beta} \end{bmatrix} \tag{4.6}$$

Where $c_{\alpha\alpha}$ is the covariance matrix between known points, $c_{\beta\beta}$ is the covariance matrix between unknown target points and $c_{\alpha\beta}$ is the covariance matrix between known and unknown points, all at the frequency ω_k.

Let $A_s = \{A_{s\alpha}, A_{s\beta}\}$, denote the set of simulated Fourier coefficients at the frequency ω_k, where the subsets $A_{s\alpha} = \{ A_{1k}, A_{2k}, A_{3k}, \dots\dots\dots\dots A_{nk}\}$ and $A_{s\beta} = \{ A_{n+1,k}, \dots\dots\dots\dots A_{n+m,k}\}$ corresponds to coefficients at known and unknown target points, respectively. The set of coefficients B_s can be defined similarly. Now, for admissible spatial correlation and spectral density functions, $\rho_{wk}(\gamma_{ij})$ and $G(\omega_k)$, the matrix C_k is positive and can be expressed as the product of a lower triangular matrix L_k and its transpose employing a Cholesky decomposition.

$$C_k = L_k L_k^T \tag{4.7}$$

Assuming that $z_i(t)$ is normally distributed (Gaussian), then A_s and B_s can be generated from

$$A_s = L_k U_k \quad \& \quad B_s = L_k V_k \tag{4.8}$$

Where each element of $U_k^T = \{U_{1k}, U_{2k}, \dots\dots\dots\dots U_{Nk}\}$ and $V_k^T = \{V_{1k}, V_{2k}, \dots\dots\dots\dots V_{Nk}\}$ are independent standard normal random variables. Under these definitions, $A_s and\ B_s$ have the correct distributions like $E[A_s]$= 0, $cov[A_s] = L_k\{\text{cov}[u_k]\}L_k^T = C_k$, since $E[U_k] = 0$ and $\text{cov}[u_k] = I$, the identity matrix.

Thus, the generation of the correlated set of Fourier coefficients can proceed using K sets of independent random numbers and the Cholesky decomposition of C_k at each frequency $\omega_k, k = 0,1,2 \dots\dots K-1$, to yield the correlated set of ground motions. To produce motions that are conditioned on the recordings at points x_α, a set of Best Linear Unbiased

Estimators (BLUE) must be employed for each of the unknown points x_β by Heredia-Zavoni, 1993;

$$A^*_{s\beta} = C^T_{\alpha\beta} C^{-1}_{\alpha\alpha} A_{s\alpha}, \qquad B^*_{s\beta} = C^T_{\alpha\beta} C^{-1}_{\alpha\alpha} B_{s\alpha} \tag{4.9}$$

So that $A^*_{s\beta}$ and $B^*_{s\beta}$ are the best linear unbiased estimates of the simulated Fourier coefficients at the unknown target points. Similarly, given the actual Fourier coefficients at the known points that are obtained by Fourier decomposition of the recordings, A_α and B_α, the BLUE coefficients at the unknown points are given by

$$A^*_{\beta} = C^T_{\alpha\beta} C^{-1}_{\alpha\alpha} A_{\alpha}, \qquad B^*_{\beta} = C^T_{\alpha\beta} C^{-1}_{\alpha\alpha} B_{\alpha} \tag{4.10}$$

Finally, the conditioned Fourier coefficients may be obtained by combining all three forms

$$A_C = A^*_\beta + A_{s\beta} - A^*_{s\beta}, \qquad B_C = B^*_\beta + B_{s\beta} - B^*_{s\beta} \tag{4.11}$$

The conditioned Fourier coefficients A_C and B_C have the proper covariance structure, thus the conditioned random field exactly matches the known motions at the known points and becomes increasingly 'random' with distance from the known points.

$$z_j(t) = \sum_{k=1}^{K} A_c \, cos\omega_k(t - \Gamma) + B_C \, sin\omega_k(t - \Gamma) \tag{4.12}$$

Where 'Γ' is the time lag between the two generation points such that

$$\Gamma = \frac{x_{PQ}\, cos\Psi}{v_{app}} \tag{4.13}$$

'Ψ'is the angle between the vector of surface wave propagation and the vector that goes from P to Q and $'v_{app}'$ is the surface wave velocity.

In order to quantify the acceleration time histories in different points in space, all that is needed is a definition of the correlation between amplitudes and of their dispersion, as measured by the covariance matrix of their amplitudes.

The diagonal terms of the covariance matrix are expressed by the Power Spectral Density (PSD) function at each generation point and the off-diagonal terms of the covariance matrix are defined by the correlation coefficient $'\rho'$ which defines the similitude in terms of amplitudes for each frequency between two signals generated at two different points and by the Power spectral density assumed at these points.

In the case of propagation between two points P and Q, the diagonal terms of the covariance matrix are quantified via Power spectral density functions PSD_{PP} and PSD_{QQ} at P and Q only. The off-diagonal terms PSD_{PQ} and PSD_{QP} are obtained by a coherence coefficient $'\rho'$ and PSD functions at the two points P and Q, crossed by the signal during the propagation.

The correlation coefficient $'\rho'$ can be expressed via coherency functions. There are different coherency functions in literature able to describe the coherence variation from point to point for each signal frequency. The isotropic frequency-dependent spatial correlation function given by Fenton (1991) is given in Eq. 4.14.

$$\rho_{(x)} = e^{-\omega_k |X|/(2\pi v_s s)} \tag{4.14}$$

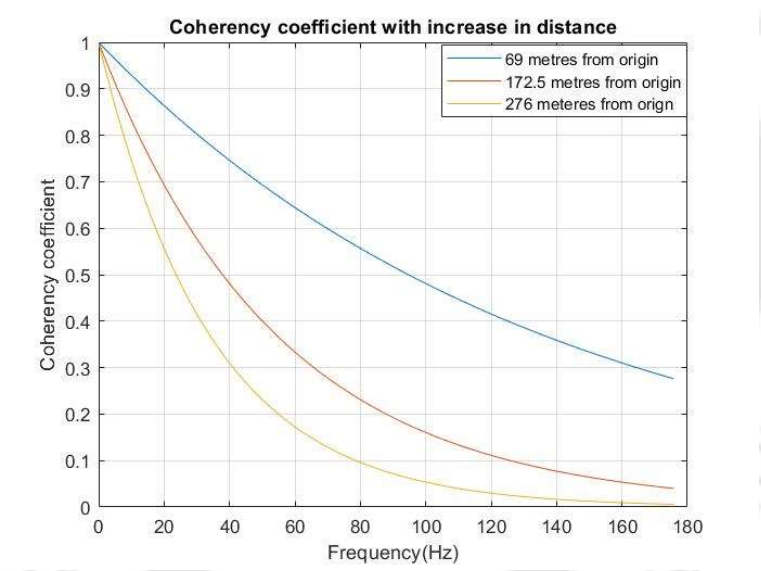

Fig. 4.3. Coherence co-efficient with increase in distance

The coherence model for each circular frequency is a function of the distance X between the two points where the signals are generated and $'v_s'$ is the shear wave velocity and $'s'$ is the coherence parameter. The generation of asynchronous signal on a complex site composed of different soil units, the effect of soil wave interaction can be different for each soil unit and so it is important to consider the proper input PSD function for each soil unit.

The Auto-power spectral density function of the ground acceleration characterizing the earthquake process is assumed to be of the following form modified by Clough and Penzien (1975).

$$G(\omega_k) = s_0 \left|H_g(\omega)\right|^2 \left|H_f(\omega)\right|^2 \tag{4.15}$$

$$H_g(\omega) = \frac{\omega_g^2 + 2i\xi_g\omega_g\omega}{\omega_g^2 - \omega^2 + 2i\xi_g\omega_g\omega} \tag{4.16}$$

$$H_f(\omega) = \frac{\omega^2}{\omega_f^2 - \omega^2 + 2i\xi_f\omega_f\omega} \tag{4.17}$$

Where S_0 is the amplitude of the white-noise bedrock acceleration; ω_g and ξ_g are the filter parameters of the well-known Kanai-Tajimi model representing the natural frequency and damping of the soil layer and ω_f and ξ_f are parameters of a second filter which is introduced to assure finite power for the ground motion.

The parameters of the auto-power spectral density function corresponding to different soil types proposed by Dumanogluid *et al*. (2003) are listed in Table 4.1.

Table 4.1. Parameters of Auto-Power spectral density function corresponding to different soil

Soil type	ω_g (rad/sec)	ξ_g	ω_f (rad/sec)	ξ_f	S_o (m^2/sec^3)
Firm	15.0	0.6	1.5	0.6	0.00177
Medium	10.0	0.4	1.0	0.6	0.00263
Soft	5.0	0.2	0.5	0.6	0.00369

A set of nine correlated ground motions are generated at a distance of different spans of the bridge at the respective foundations. The ground motions that are considered are made to spectrum compatible for Design based Earthquake (DBE) using SeismoMatch software and also using self-generated code in MATLAB and are conditioned to generate correlated earthquake motion at different support positions of the bridge.

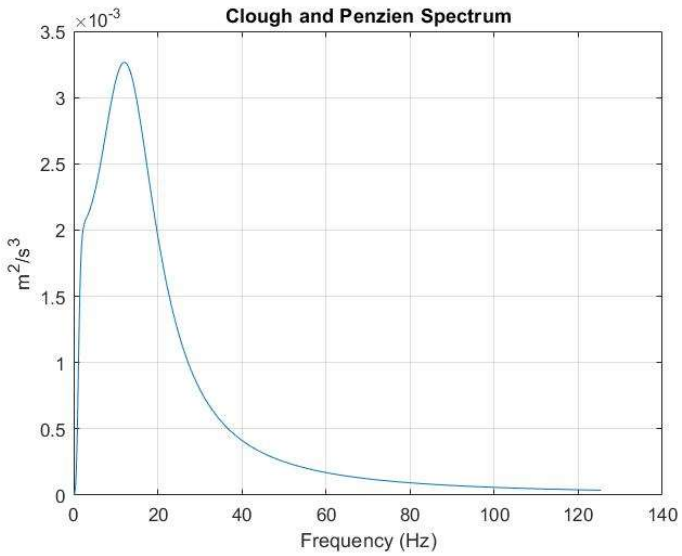

Fig. 4.4. Spectrum proposed by Clough and Penzien spectrum (1975)

4.2.3 Input ground acceleration time history

Time history analyses have been performed by selecting two earthquake signals such as El Centro 1940 and Koyna 1967. These time histories are made spectrum compatible for Design Basis Earthquake (DBE) as per IS:1893-2016 with respect to site-specific hazard level using SeismoMatch. Fig. 4.5 to Fig. 4.8 show different considered input ground motions and their Fourier Amplitudes. Table 4.2 summarizes the predominant frequency range and Peak Ground Acceleration of the considered ground motions.

Table 4.2. Characteristics of Input ground motions

Ground motion	El Centro	Koyna
PGA (in 'g')	0.304	0.473
Frequency range (Hz)	0.1-10	1-10

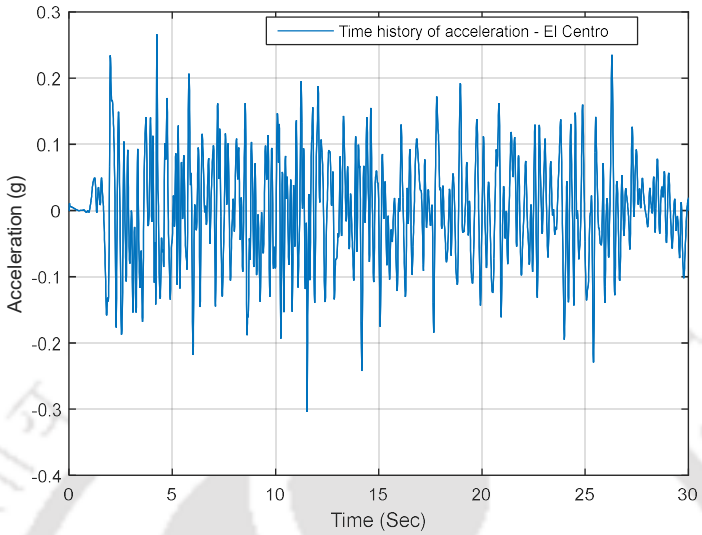

Fig. 4.5. El Centro Ground motion

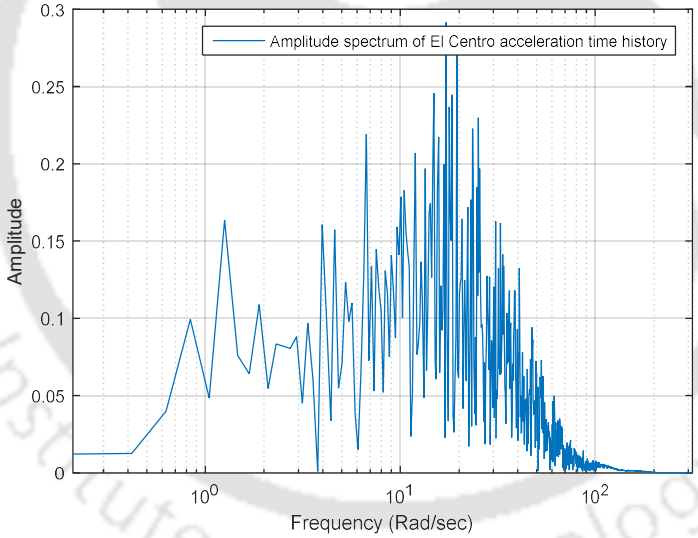

Fig. 4.6. Fourier transform of El Centro ground motion

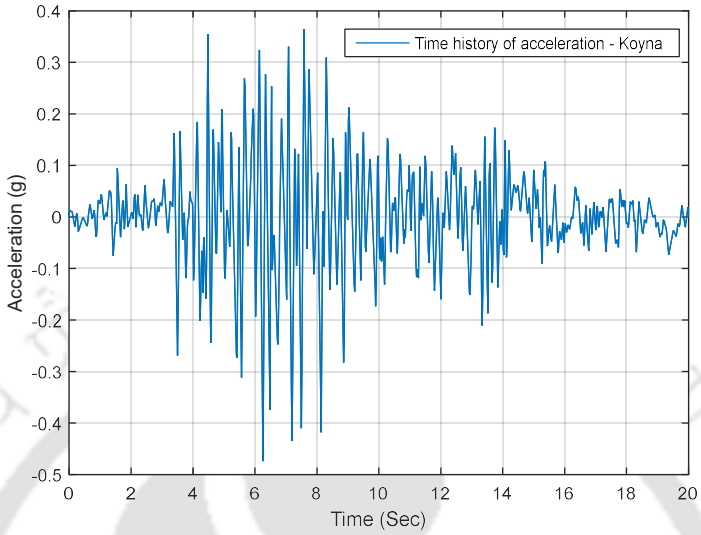

Fig. 4.7. Koyna ground motion

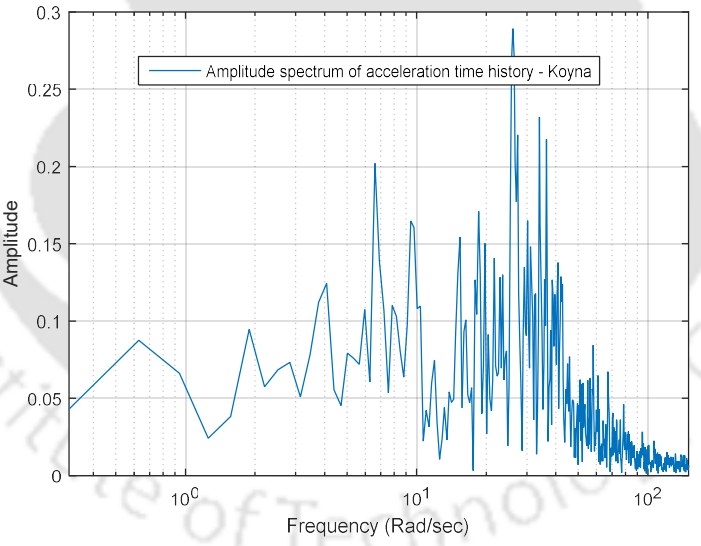

Fig. 4.8. Fourier transform of Koyna ground motion

4.2.4 Analysis method of multi support excitation

Multi-support excitation in SAP 2000 Nonlinear is performed by converting acceleration time history to displacement time history, while the time step is reduced to $\frac{1}{10}\ th$ of

acceleration time history. The *P-y* spring is positioned along with two orthogonal directions on the horizontal plane and is connected to the pile at discrete points over its length. The converted displacement time history and applied as joint/ground displacement at each fixed end of the two-jointed *P-y* spring (Fig. 4.9). The structural response that is obtained from displacement-based input is the total displacement response, whereas for acceleration-based input, the response that is obtained is the relative displacement response. The equations of motions that are solved by SAP 2000 for performing multi-support excitation are

$$\begin{bmatrix} M_{ss} & M_{sb} \\ M_{sb} & M_{bb} \end{bmatrix} \begin{pmatrix} \ddot{u}_s \\ \ddot{u}_b \end{pmatrix} + \begin{bmatrix} C_{ss} & C_{sb} \\ C_{sb} & C_{bb} \end{bmatrix} \begin{pmatrix} \dot{u}_s \\ \dot{u}_b \end{pmatrix} + \begin{bmatrix} k_{ss} & k_{sb} \\ k_{sb} & k_{bb} \end{bmatrix} \begin{pmatrix} u_s \\ u_b \end{pmatrix} = \begin{Bmatrix} 0 \\ R_b \end{Bmatrix} \tag{4.18}$$

where $\ddot{u}_s, \dot{u}_s, u_s$ are the vectors representing the motion of the superstructure in the absolute coordinate system; $\ddot{u}_b, \dot{u}_b, u_b$ are the vectors representing ground motion in the absolute coordinates; M_{ii}, C_{ii}, k_{ii} are the mass, damping and stiffness matrices. The subscripts like *ss, bb* and *sb* are the degrees of freedom of superstructure, base and their coupled term. R_b is the lateral reaction at the nodes of the foundation. Considering the expanded form of first row of Eq. 4.18, we get

$$M_{ss}\ddot{u}_s + C_{ss}\dot{u}_s + k_{ss}u_s = -(M_{sb}\ddot{u}_b + C_{sb}\dot{u}_b + k_{sb}u_b) \tag{4.19}$$

In case of the lumped mass model, all non-diagonal terms are zero, thus M_{sb} is equal to zero. The damping term $-C_{sb}\dot{u}_b$ is usually small relative to the inertia term and thus can be neglected. So, Eq. 4.19 can be written as

$$M_{ss}\ddot{u}_s + C_{ss}\dot{u}_s + k_{ss}u_s = -k_{sb}u_b \tag{4.20}$$

where u_b is the vector of ground motion in terms of displacements; $-k_{sb}u_b$ is the force experienced by the superstructure for the ground motion in the absolute coordinates. Eq. 4.20 is the displacement-based input model for the analysis of structure under ground motion.

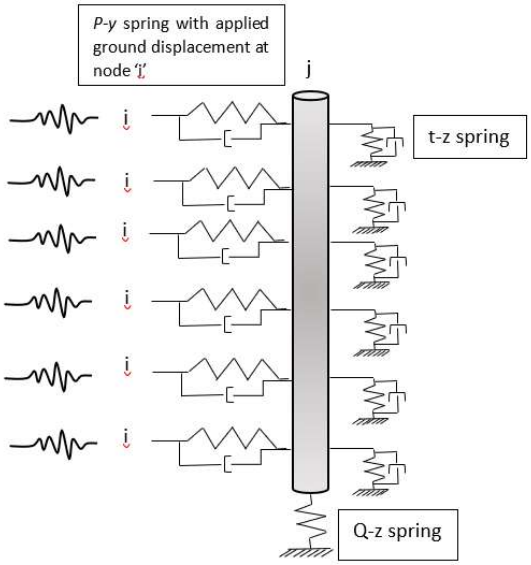

Fig. 4.9. Schematic diagram of Pile with input ground displacement at 'i^{th}' node

4.2.4.1. Procedure for solution of multi support excitation problem in SAP 2000

It is necessary to first convert the acceleration time history record to its corresponding displacement time history. The output accuracy will depend upon the input time step for displacement time history response. SAP 2000 manual suggest using a smaller time step i.e., $\frac{1}{10}$ that of acceleration record.

The integration process performed to produce displacement time history records from the acceleration time history records should produce zero displacements at either end of the displacement record, if non-zero displacement exists a baseline correction must be applied and the same has been done as per the general procedure using code in MATLAB.

Once the displacement time history is obtained from the acceleration record, a ground motion may be applied to specific support restraints through manual multi-support excitation, described as follows

- At joints of interest i.e., at the fixed end of the soil-spring element attached to the pile, define a load pattern. This loading pattern should apply unit values of joint displacement in the direction of applied acceleration.

- Assign the displacement time-history to the above-created load pattern in order to apply the excitation in the desired direction and mention the arrival time of this time history in the advanced load parameter options in SAP 2000 Nonlinear.

4.3. Seismic analysis of the long span bridge for synchronous and asynchronous input motion

Considering the fault plane along the longitudinal direction and the direction of propagation of waves is also along the longitudinal direction exciting the structure in the transverse direction, the transverse displacements response of the pier and abutment tops and its effect on track alignment has been compared.

In the present study, two earthquake records with different peak accelerations, frequency contents and durations have been selected as input motion for the time-history analysis of the considered bridge. These recorded earthquakes are Koyna (1967): Comp – Longitudinal and El Centro (1940): Comp – 180. These input earthquake motions have been converted to spectrum compatible with respect to design spectrum for DBE (5% damped) as presented in IS: 1893, 2016. These spectrum compatible time histories are used as synchronous input motion. The conditional simulation of earthquakes that vary spatially using the procedure that has been developed by Fenton *et al*. (1991) is adopted in this study and is used as asynchronous input motion.

4.3.1 Comparison of responses at Pier top

As the earthquake wave reaches Pier-P1, there is a reduction in the amplitude of the absolute displacement as compared to A1. This is expected since there is a reduction in the amplitude and shift in phase as the wave travels from one pier to another. However, due to the continuity of the bridge, the relative displacement is higher in case of asynchronous and wave passage effect due to the delay in arrival time at different piers as shown in Fig. 4.10 (a) and (b). This trend of decrease in the total displacement response and increase in relative displacement are also observed in the subsequent piers as may be seen in Figs. 4.10. (c-d). The displacement time histories at the pier and abutment top are further used to

specifically show the peak values of displacement for both the cases of Koyna and El Centro ground motion (Fig. 4.11).

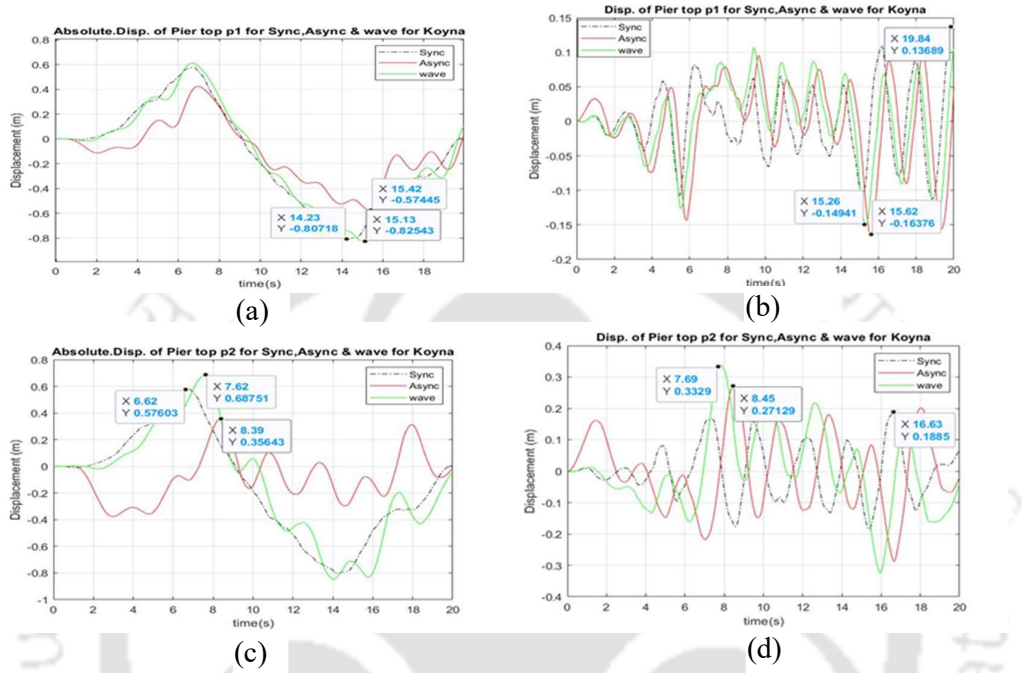

Fig. 4.10. Displacement response of different piers under Koyna input

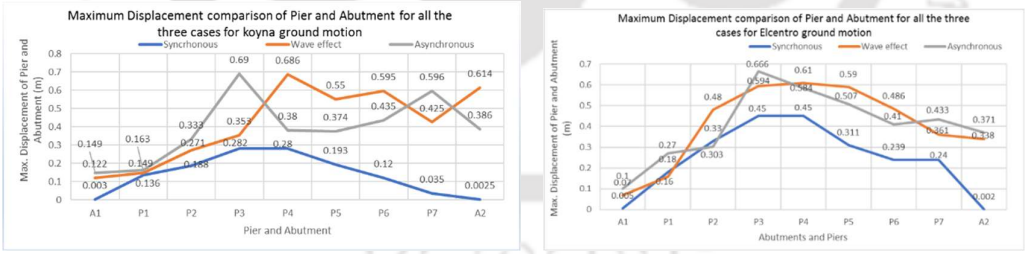

(a) With Koyna input motion (b) With El-Centro input motion

Fig. 4.11. Maximum absolute displacement values for two different input motion

4.3.2 The relative displacement of adjacent piers

The bridge under consideration have different height of piers and thus introduces geometric irregularity. The piers which are adjacent to each other and have the same natural frequency may vibrate in phase without introducing any relative displacement between them. In the

present case, both Pier-3 and Pier-4 are of 141m height with 103.5m span between them and are observed to move in the same phase for synchronous input case. Considering the wave passage effect or asynchronous motion, the wave hit these piers at different arrival times and there is a significant relative displacement between those two piers which cannot be observed in the synchronous motion-based analysis. This larger relative displacement may result in unseating of girders from supporting bearings. The relative displacement responses of the adjacent piers with different geometric configurations are shown in Fig. 4.12 (a) & (b). The peak values of the relative displacements of different girders are specifically shown in Fig. 4.13. It is seen that girders supported on the identical piers show larger relative displacement in the asynchronous and wave passage compared to synchronous case.

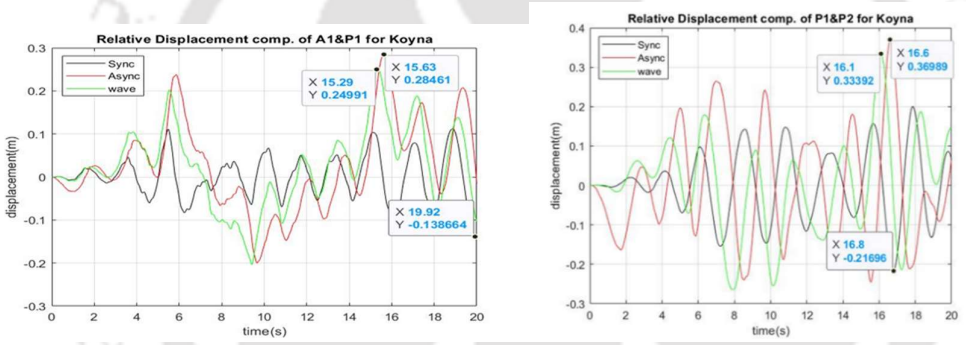

(a) Between A1 and P1 (b) Between P1 and P2

Fig. 4.12. Relative displacements between two consecutive supports

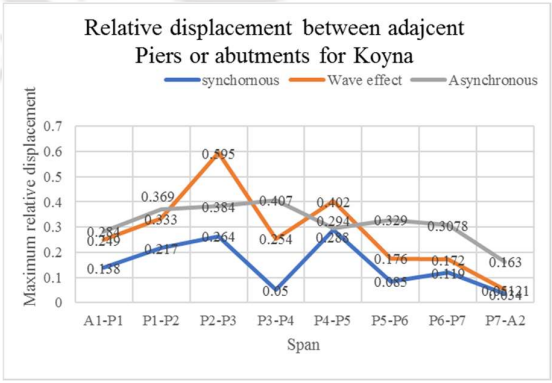

Fig. 4.13. Relative displacements of different spans of the bridge

4.3.3 Other significant observations

The input motion with wave passage effect and coherency losses can introduce significant variation in responses of some degree of freedom, which are otherwise observed to have negligible values under synchronous motion as input. A few superstructure nodes such as node number 387 on span P3-P4 and node number 588 on span P1-P2 are considered for the study, which are rotational degree of freedom i.e., torsion for the considered span. Fig. 4.14. (a) & (b) clearly indicate that the torsion at those nodes are significantly higher for asynchronous case and motion with wave passage effect than the similar values corresponding to synchronous motion case. Similar observations were also made by Balamonica *et al*. (2015) that the torsional degree of freedom is underestimated in analysis with synchronous input and may cause significant torsional stresses in the superstructure.

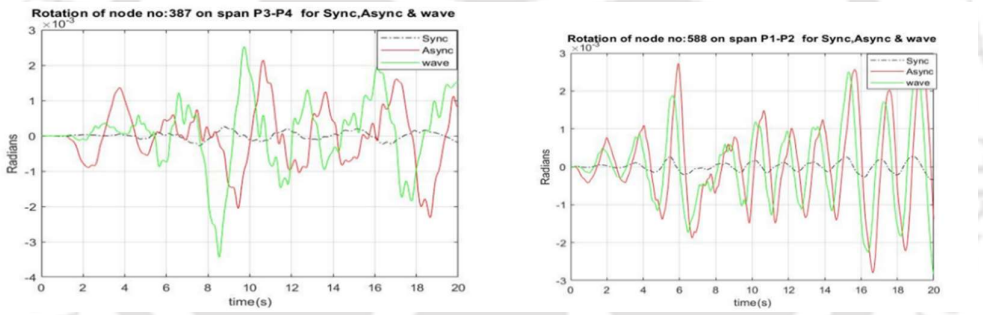

(a) At node 387 on span P3-P4 (b) At node 588 on span P1-P2

Fig. 4.14. Torsional rotation under El-Centro ground motion

4.3.4 Effect on track curvature

The curvature of the deflected track has been studied for El-Centro EQ and Koyna EQ. Fig. 4.15 to Fig. 4.28 show the track alignment corresponding to maximum absolute displacement of the top of the individual substructure and corresponding effect of curvature in the track along the length of the bridge for El Centro EQ ground motion. In Fig. 4.29 and Fig. 4.30, the curvature of the deflected track has been plotted along the length of the bridge at different time instances when the individual pier top deflections are maximum corresponding to El Centro and Koyna EQ.

The actual absolute deflection of the pier tops and the mid span absolute deflection of the superstructures at the desired time instances have been taken from the analysis results of

SAP 2000. These points have been joined by spline using codes in MATLAB to get the deflected shape of the track. The boundary condition to form the spline is, angle of rotation of the track at the two abutment ends are zero as the track beyond the abutments may be considered as aligned along the bridge axis. Curvature of the deflected shape of the track has been calculated along the length of the bridge from the spline coordinates.

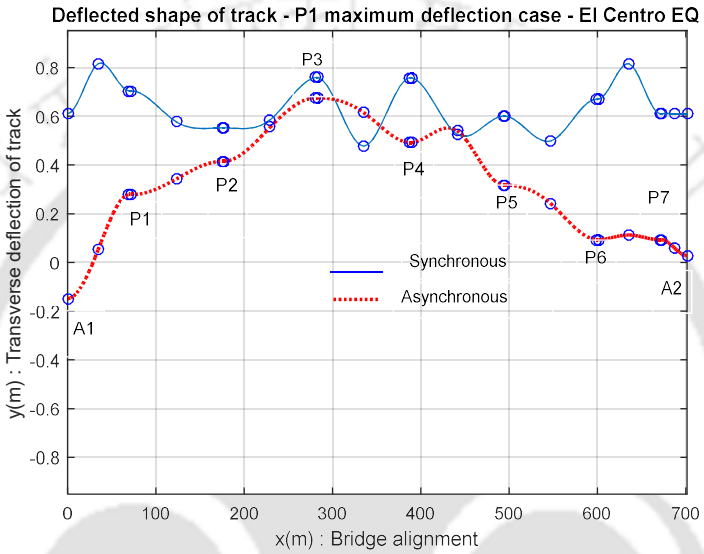

Fig. 4.15. Track alignment when P1 absolute displacement is maximum – El Centro

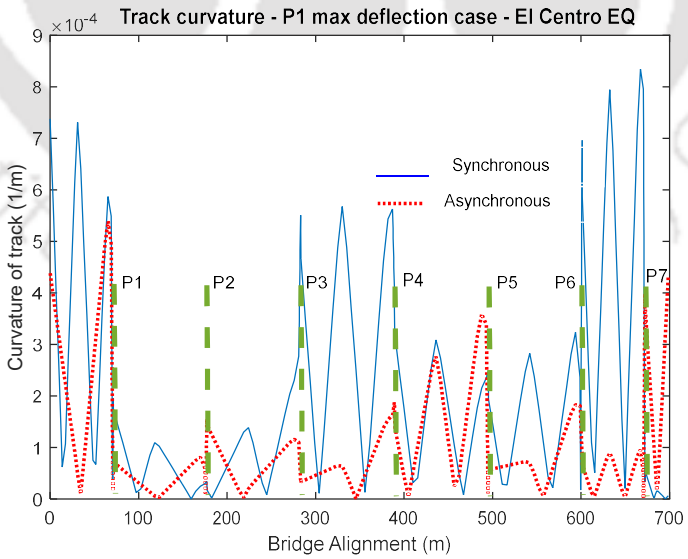

Fig. 4.16. Track curvature when P1 absolute displacement is maximum – El Centro

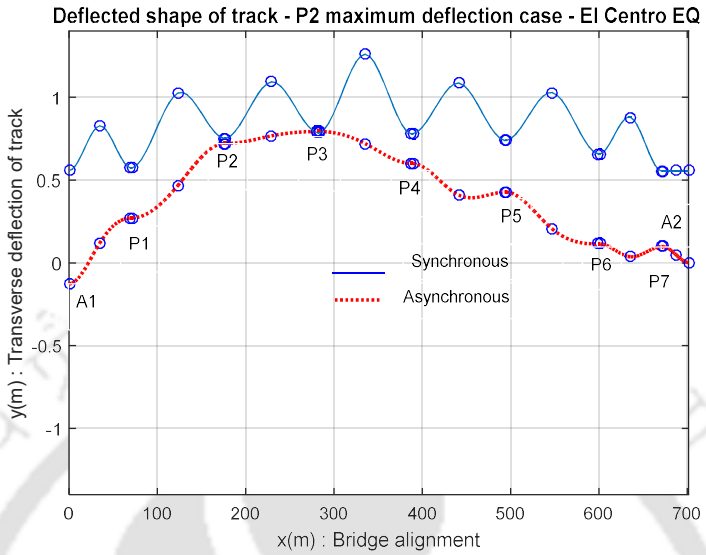

Fig. 4.17. Track alignment when P2 absolute displacement is maximum – El Centro

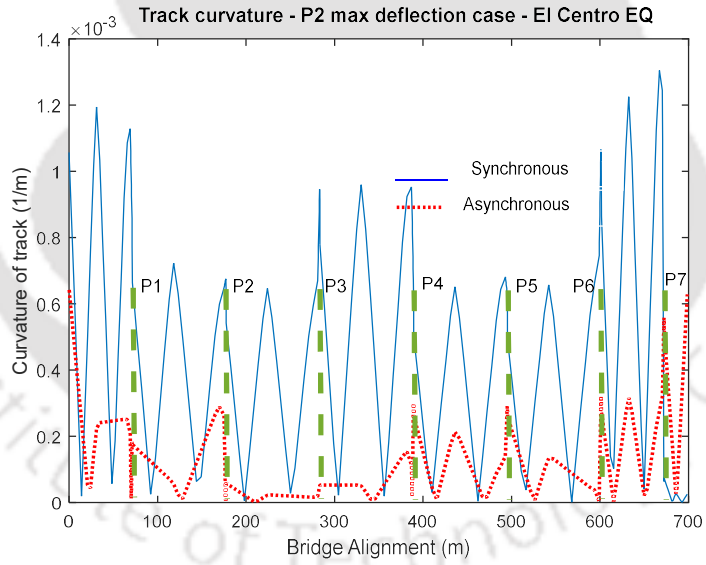

Fig. 4.18. Track curvature when P2 absolute displacement is maximum – El Centro

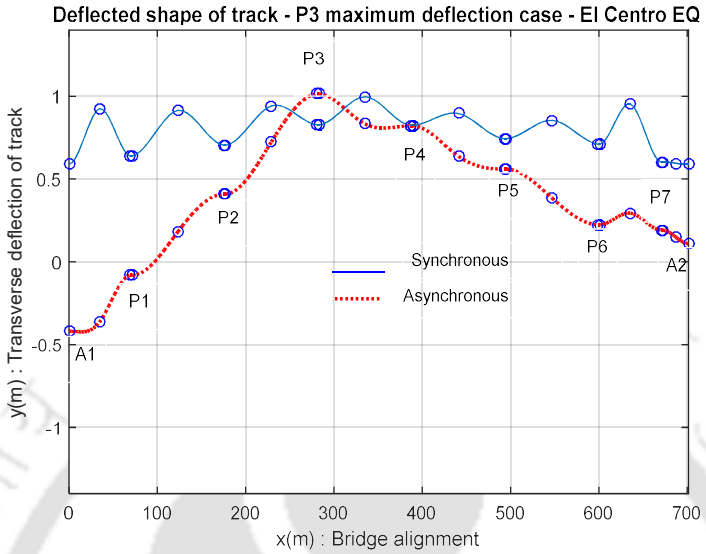

Fig. 4.19. Track alignment when P3 absolute displacement is maximum – El Centro

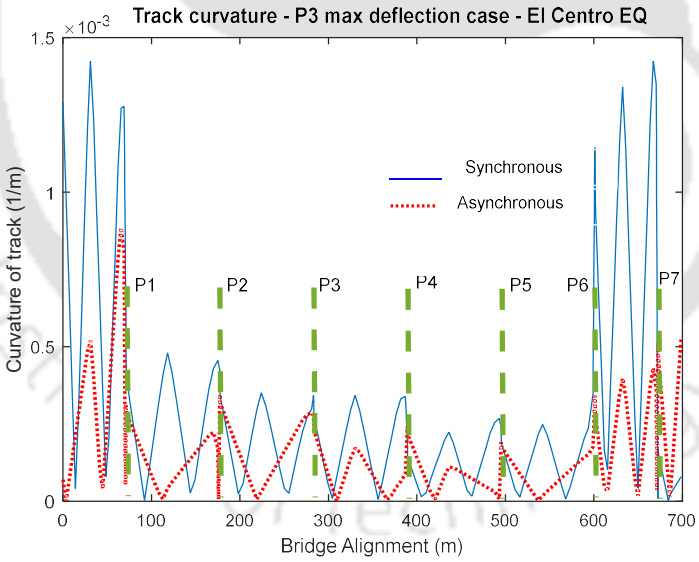

Fig. 4.20. Track curvature when P3 absolute displacement is maximum – El Centro

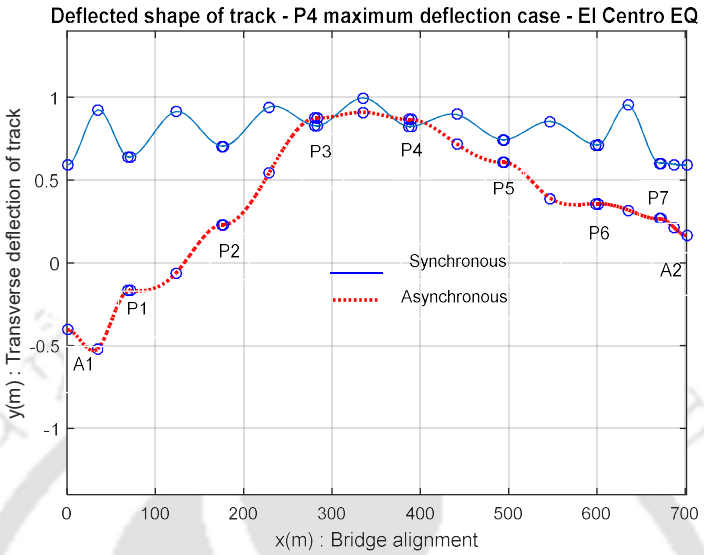

Fig. 4.21. Track alignment when P4 absolute displacement is maximum – El Centro

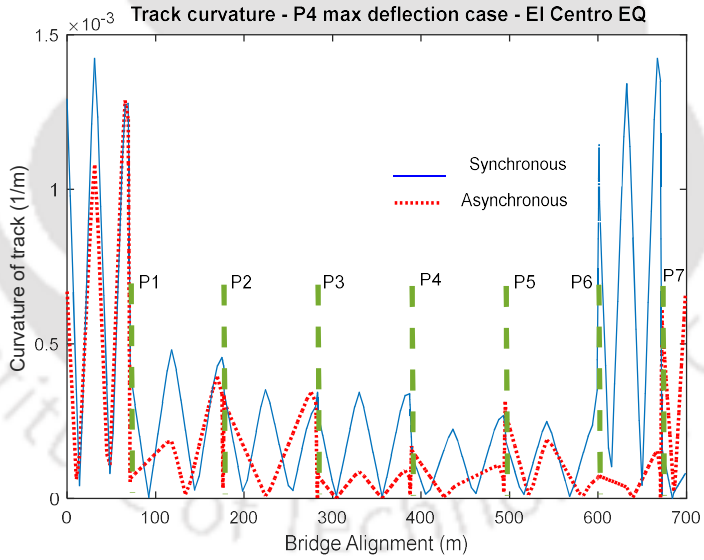

Fig. 4.22. Track curvature when P4 absolute displacement is maximum – El Centro

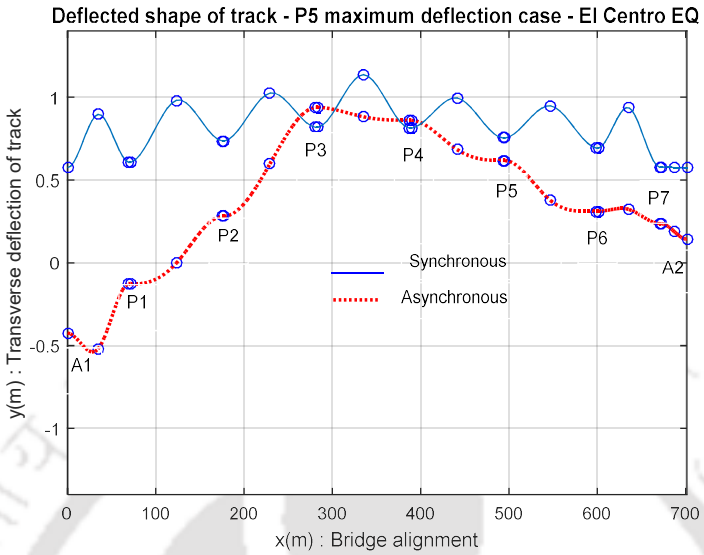

Fig. 4.23. Track alignment when P5 absolute displacement is maximum – El Centro

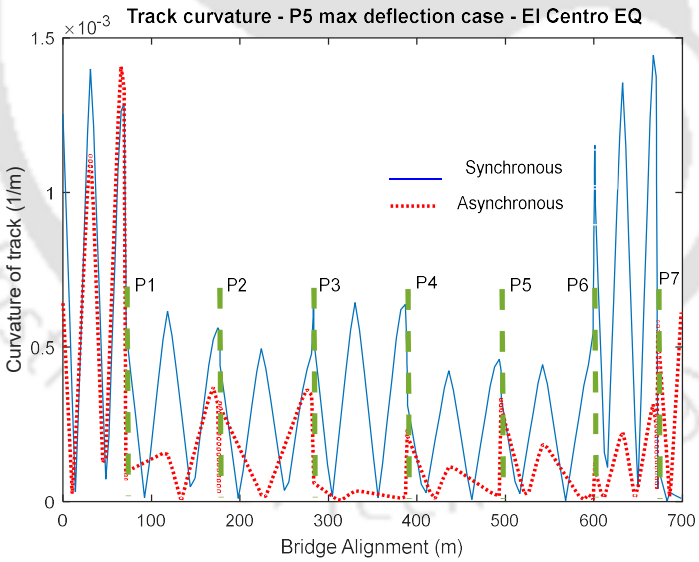

Fig. 4.24. Track curvature when P5 absolute displacement is maximum – El Centro

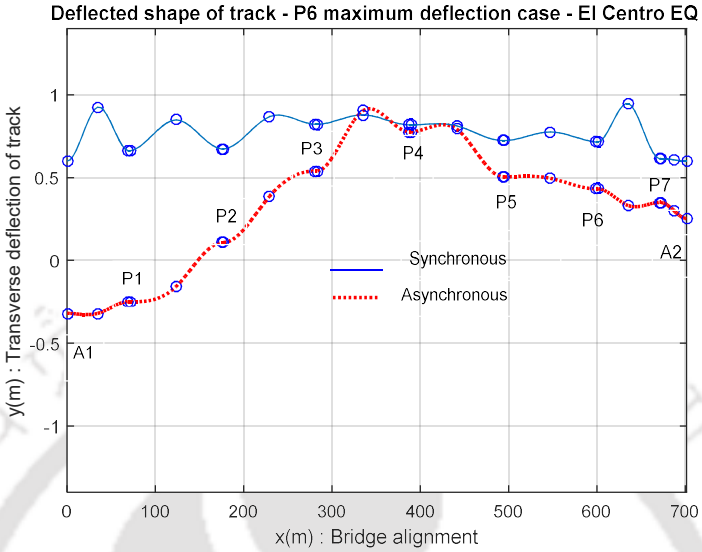

Fig. 4.25. Track alignment when P6 absolute displacement is maximum – El Centro

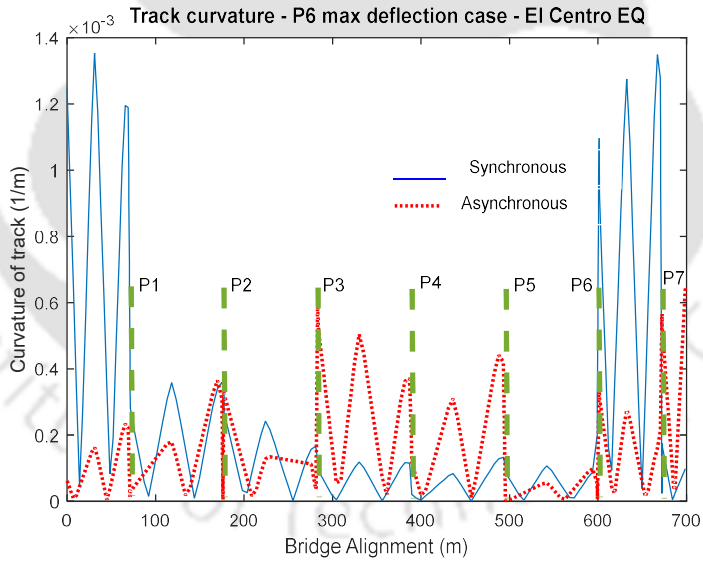

Fig. 4.26. Track curvature when P6 absolute displacement is maximum – El Centro

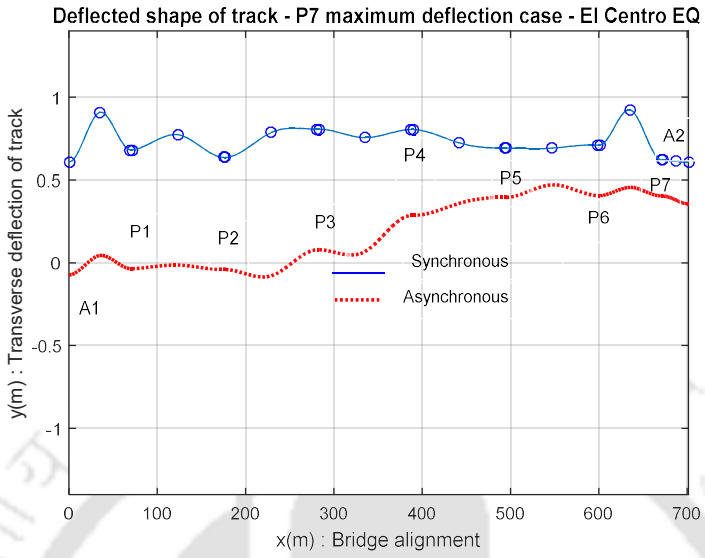

Fig. 4.27. Track alignment when P7 absolute displacement is maximum – El Centro

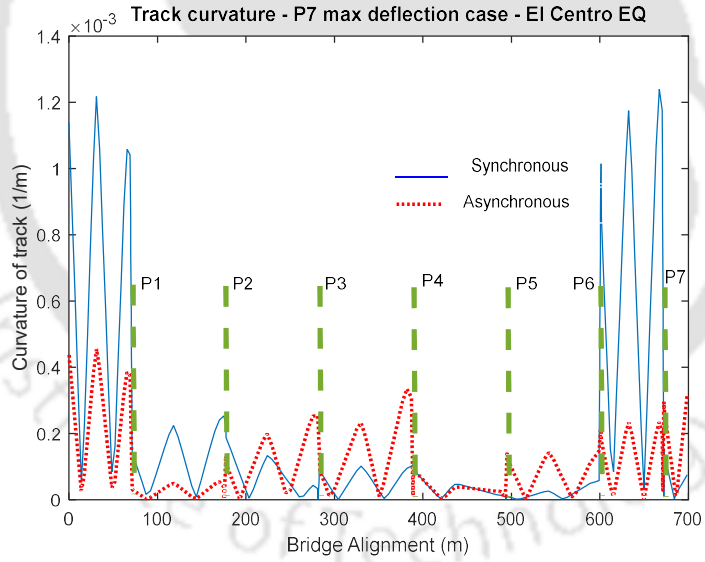

Fig. 4.28. Track curvature when P7 absolute displacement is maximum – El Centro

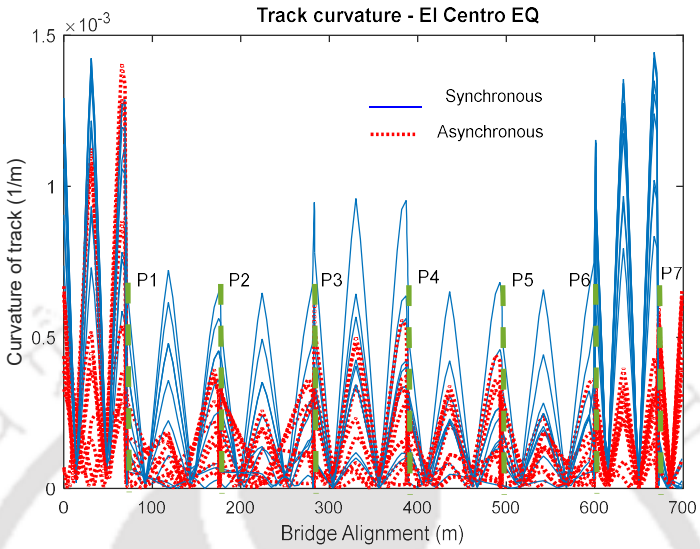

Fig. 4.29. Track curvature for synchronous and asynchronous ground motion considering El-Centro EQ at various time instances when individual pier deflections are maximum

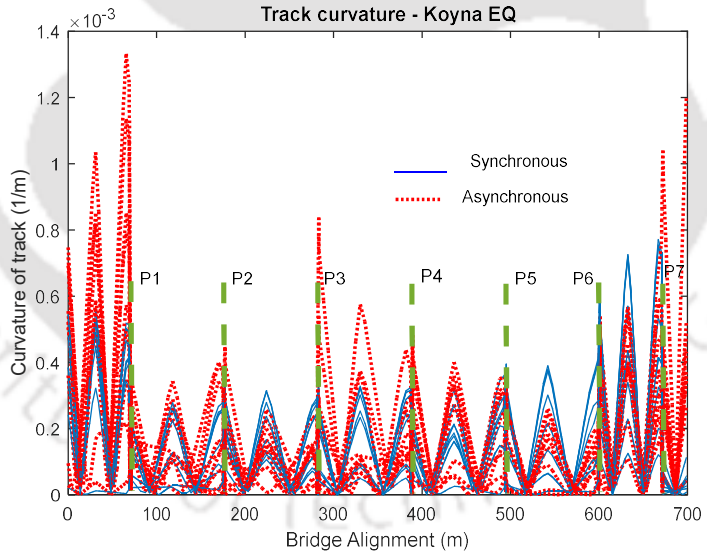

Fig. 4.30. Track curvature for synchronous and asynchronous ground motion considering Koyna EQ at various time instances when individual pier deflections are maximum

From Fig. 4.15 to 4.28, from the deflected shape of the track it can be found that overall absolute displacement of the pier tops are more in synchronous motion compared to the asynchronous one. However, the relative movement of one pier top compared to the

consecutive pier top does not show any specific trend of one is higher compared to the other. The same is also apparent from the curvature diagrams amongst the Fig. 4.15 to 4.28. In Fig. 4.16, curvatures at the edge and at the centre of the bridge alignment is much higher in synchronous motion compared to asynchronous one. In Fig. 4.18, in general all along the length of the bridge, curvature is higher in case of synchronous motion. In Fig. 4.20, Fig. 4.22 and Fig. 4.24, curvature at the edge of the bridge is much higher for synchronous motion. In Fig. 4.26 and Fig. 4.28, curvature at the centre of the bridge is higher for asynchronous motion. In Fig. 4.29, all the track curvature graphs for El Cento EQ have been superimposed and it is generally seen that the curvature of track under synchronous motion is higher. Similar plots for Koyna EQ has been prepared and superimposed as is shown in Fig. 4.30 where the trend is found to be opposite to the previous case shown in Fig. 4.29, i.e. the track curvature is in general more in case of asynchronous motion.

The safe velocity of the train during EQ varies with the curvature of the track. More is the curvature less will be the safe velocity. From the above discussion, it may be inferred that track curvature for asynchronous ground motion may be higher or lower compared to the synchronous ground motion for different EQ time history. Hence, analyses should be carried out considering both synchronous and asynchronous ground motion for long bridges for assessment of safety of running train during earthquake.

4.4. Concluding remarks

A long-span bridge with through type OWG is considered for the detailed seismic analysis. Finite element model of the bridge is made along with SSI using 1D nonlinear uncoupled springs. The bridge model is analysed using synchronous and asynchronous ground motions and the responses of the bridge are studied. The displacement responses of the Pier and abutments are observed along with the relative displacement of adjacent piers.

The important conclusions are as follows:

- Increase in the displacement demand in piers and abutments are observed for the analysis with asynchronous input as compared to synchronous input based analysis. The maximum relative displacement between top of piers is occurring in between the two tallest piers P3 and P4 (141m tall) and value is 407mm for asynchronous

motion against 50mm for synchronous motion. The maximum relative displacement is 264mm corresponding to synchronous motion and is occurring between piers P2 and P3 where the pier height is less. The same value for asynchronous motion is 384mm.

- Coherency losses in input motion may result in unseating of the superstructure due to larger relative displacement of adjacent piers.
- Active rotational degree of freedom that may lead to higher torsion in the superstructure, which is significant in asynchronous motion compared to synchronous motion. The maximum torsional rotation in the superstructure at P3-P4 for asynchronous motion is 2e-3 against synchronous motion which is 2e-5. The same torsional rotation in the superstructure at P1-P2 for asynchronous motion is 2.8e-3 against synchronous motion which is 2.5e-5.
- Effect of curvature in track due to synchronous motion and asynchronous motion is case sensitive and depends on the characteristics of ground motion itself. For El-Centro EQ the curvature of the track is on average 0.75E-3 against synchronous motion and 0.25E-3 for asynchronous motion. At two edges of the bridge ie at span A1-P1 and P6-P7, P7-A2, the values are relatively high. The same figures for Koyna EQ are 0.25E-3 and 0.4E-e3. At the two edges of the bridge, the figures are relatively high like El-Centro EQ case. This shows that the track curvature is more for synchronous motion in case of El-Centro EQ where as it is more for asynchronous EQ in case of Koyna EQ.

Chapter 5

Tuned Mass Damper and its effect on vertical response of OWG rail bridge

5.1. Introduction

During movement of train, the effect of vertical flexibility of superstructure, flexibility of suspension system of the train and track surface roughness amplifies the deflection of bridge deck. Tuned mass damper (TMD) may reduce this vertical dynamic deflection of the super-structure. This may cause reduction in the coefficient of dynamic augmentation (CDA) value leading to lesser steel consumption in the design of superstructure and hence may reduce mass of the superstructure, which in turn will reduce the design focres of substructure. The study of TMD for 103.5m open web girder (OWG) superstructure has been done in detail to understand the effect of TMD on reduction of CDA of flexible light superstructure bridge.

5.2. Methodology adopted

A typical span of 103.5 m with OWG configuration has been considered for study which are being constructed by North Eastern Frontier Railway in their present projects of connecting North eastern states of India with railway line.

A Vehicle Bridge Interaction (VBI) model has been introduced to simulate the train load. The vehicle model considered is having 27 DOF as shown in Fig. 5.1. Effect of track irregularity has been included in the analysis. Single bogie loading (SBL) is considered in the analysis having four axles with total load of 100T as shown in Fig. 5.2 (a). Similarly, Multiple bogie loadings (MBL) have also been considered in the analysis which is equivalent to 9.33 t/m loading as per the 25T-2008 loading standard of Indian railway as presented in Fig. 5.2 (b). From the VBI model, the responses like midspan deflection, strains at central top chord and central bottom chord have been plotted as a function of speed of the vehicle. From these plots, Coefficient of Dynamic Augmentation (CDA) can

be estimated as a function of speed for chord members of the OWG. TMD has been added at the mid span of the superstructure and its effect is studied. The study has been done for both SBL and MBL condition for OWG model.

The speed *vs* deflection graphs has been plotted up to 1000 kmph speed. The high speed has been considered to understand the speeds at which the maximum deflections are likely to occur. Principally, the focus has been kept to explore the effect of TMD up to the standard speed in Indian Railway scenario, which is considered as 180 kmph.

5.2.1. Formulation of VBI model

The VBI system models consist of the vehicle model, bridge model and their interaction model. For the vehicle model, the car body, bogies and wheel-sets of each vehicle are considered as rigid components with 27 DOFs i.e., the elastic deformations of these components are not taken into consideration (Yang and Wu (2001). The suspension systems that link the car body and the bogies (secondary suspension system) and also the bogies and the wheel sets (primary suspension system) are represented by springs with linear property and dampers with viscous property as shown in Fig. 5.1. In modelling of car-body and each of the bogies in a vehicle, 5 DOFs are considered as lateral ($y^{c,b}$), vertical ($z^{c,b}$), roll ($\theta_x^{c,b}$), yaw ($\theta_y^{c,b}$), and pitch ($\theta_z^{c,b}$) displacement. On the other hand, for each of the wheel-set, 3 DOFs are considered, which are lateral (y^w), vertical (z^w), roll (θ_x^w). Here, superscripts "*c*", "*b*" and "*w*" stand for car-body, bogie and wheel-set. Further, it is also assumed that the wheels of the vehicle axles always remain in contact with the rails i.e., the axles are constrained by the rail and thus there is no relative displacement, velocity or acceleration between the wheel-sets and the rail-track. Therefore, 12 DOFs which are associated with the four axles, become dependent on rail and as a result independent DOFs of a vehicle body become 15, out of total 27 DOFs. The formulation procedure presented below is adopted from Yang and Wu (2001).

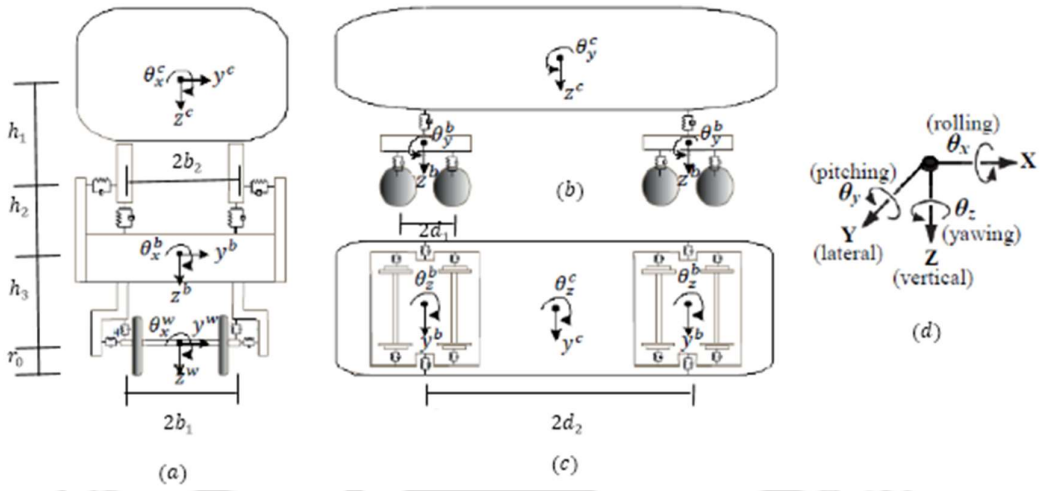

Fig. 5.1. Three-dimensional vehicle model: (a) rear view, (b) side view, (c) top view, (d) sign convention [Antolin *et al*. (2013)]

The bridge can be modelled by either Euler- Bernoulli or other type of beam elements with nodal DOF's at both ends. At a particular time, some of these elements will experience the vehicle wheels. The vehicle is decomposed into two parts: the upper or non-contact part (e.g. car body, bogie, and suspension system as in case of moving system model) and the contact part (i.e. wheels). Consider *n* wheelsets, which is represented by one vertical DOF and let the corresponding displacement vector as $\{d_w\}$.Similarly, the displacement vector for the upper part can be denoted as $\{d_u\}$.Correspondingly, there are *n* contact points on the bridge, displacement at those points are denoted by$\{d_c\}$.

Let$[m_v]$, $[c_v]$, and $[k_v]$respectively denote the mass, damping, and stiffness matrix of the whole vehicle, and also $\{d_v\}$the displacement vector of the vehicle. The equation of motion for the vehicle can be written as:

$$[m_v]\{\ddot{d}_v\} + [c_v]\{\dot{d}_v\} + [k_v]\{d_v\} = \{f_v\} \tag{5.1}$$

where$\{f_v\}$is the force vector, and $\{d_v\}$is the displacement vector for whole vehicle composed of $\{d_w\}$ and $\{d_u\}$ i.e. $\{d_v\} = \langle\langle d_u\rangle\langle d_w\rangle\rangle^T$. The vector $\{f_v\}$can be decomposed into two parts:

$$\{f_v\} = \{f_e\} + [l]\{f_c\} \tag{5.2}$$

where $\{f_e\}$denotes the external forces excluding the contact forces, $\{f_c\}$ denotes the contact forces acting on the bridge, and $[l]$ is the transformation matrix. The wheel displacement vector $\{d_w\}$can be related to the contact displacement $\{d_c\}$of the bridge by the constraint equation:

$$\{d_w\} = [\Gamma]\{d_c\} \tag{5.3}$$

where[Γ]is the transformation matrix; for no jump condition, [Γ]is a unit matrix.

Assuming that all kinematic information about the system is known at time *t*, and is required to determine the behaviour of the system for time *t*+Δ*t,* while Δ*t* is a small-time increment. The equation of motion for the system in time *t*+Δ*t* can be written in terms of upper part and wheel part as following:

$$\begin{bmatrix}[m_{uu}] & [m_{uw}]\\ [m_{wu}] & [m_{ww}]\end{bmatrix}\begin{Bmatrix}\{\ddot{d}_u\}\\ \{\ddot{d}_w\}\end{Bmatrix}_{t+\Delta t} + \begin{bmatrix}[c_{uu}] & [c_{uw}]\\ [c_{wu}] & [c_{ww}]\end{bmatrix}\begin{Bmatrix}\{\dot{d}_u\}\\ \{\dot{d}_w\}\end{Bmatrix}_{t+\Delta t} + \begin{bmatrix}[k_{uu}] & [k_{uw}]\\ [k_{wu}] & [k_{ww}]\end{bmatrix}\begin{Bmatrix}\{d_u\}\\ \{d_w\}\end{Bmatrix}_{t+\Delta t} = \begin{Bmatrix}\{f_{ue}\}\\ \{f_{we}\}\end{Bmatrix}_{t+\Delta t} + \begin{bmatrix}[l_u]\\ [l_w]\end{bmatrix}\{f_c\}_{t+\Delta t} \tag{5.4}$$

Here, subscripts '*uu*', '*ww*' refer to upper and lower part of vehicle, while '*uw*' and '*wu*' imply the coupling between them, $\{f_{ue}\}$ and $\{f_{we}\}$ denote the external forces acting on the upper and wheel parts of the vehicle. The first row in Eq. 5.4 is regarding the equation of motion of the upper part and the second row is for the wheel part. Since the contact forces only act on the wheels, the sub matrix $\{l_u\}$ has to be a zero matrix.

Expanding the first-row part of the Eq. 5.4 and using Newmark scheme of time integration, the responses related to upper part of vehicle can be obtained in terms of unknown response quantities of lower part of vehicles. Further, if the displacement $\{d_u\}_{t+\Delta t}$and its derivatives are substituted in the second row of Eq. 5.4, the contact force is then$\{f_c\}_{t+\Delta t}$obtained as (detailed procedure can be found in Yang and Wu, 2001).

$$\{f_c\}_{t+\Delta t} = [m_c]\{\ddot{d}_w\}_{t+\Delta t} + [c_c]\{\dot{d}_w\}_{t+\Delta t} + [k_c]\{d_w\}_{t+\Delta t} + \{p_c\}_{t+\Delta t} + \{q_c\}_t \tag{5.5}$$

Expressions of all the quantities in Eq. 5.5 can be found in Yang and Wu (2001). Now, using the constraint equation presented in Eq. 5.3, the contact forces $\{f_c\}_{t+\Delta t}$can be

reformulated in terms of contact displacement $\{d_c\}$considering [Γ] a unit matrix. Therefore, the i^{th} entry of the $\{f_c\}_{t+\Delta t}$ as the contact forces between i^{th} wheel and the bridge $\{V_{i,t+\Delta t}\}$can be calculated as:

$$\{V_{i,t+\Delta t}\} = p_{ci,t+\Delta t} + q_{ci,t} + \sum_{j=1}^{n}\left(m_{cij}\ddot{d}_{cj,t+\Delta t} + c_{cij}\dot{d}_{cj,t+\Delta t} + k_{cij}d_{cj,t+\Delta t}\right) \quad (5.6)$$

where m_{cij}, c_{cij}, and k_{cij} are respectively the entry in the i^{th} row and j^{th} column of the contact matrices $[m_c]$, $[c_c]$, and $[k_c]$. Similarly, the $\{p_c\}_{t+\Delta t}\ and\ \{q_c\}_t$, are the entry located in the i^{th} row of the corresponding vectors, i.e. $\{p_c\}_{t+\Delta t}\ and\ \{q_c\}_t$.

Let us assume that n wheels of the moving vehicle are acting on the n element k_1, k_2, …,k_n of the bridge elements. These elements are considered as VBI element since they are directly loaded with the vehicle. The rest of the bridge elements will be treated as the regular beam elements. For the k_ith beam element of the bridge, which is loaded by the contact force$V_{i,t+\Delta t}$, the equation of motion at time $t + \Delta t$ is:

$$[m_{bi}]\{\ddot{d}_{bi}\}_{t+\Delta t} + [c_{bi}]\{\dot{d}_{bi}\}_{t+\Delta t} + [k_{bi}]\{d_{bi}\}_{t+\Delta t} = \{f_{bi}\}_{t+\Delta t} - \{f_{bci}\}_{t+\Delta t} \quad (5.7)$$

where$[m_{bi}]$, $[c_{bi}]$, and $[k_{bi}]$are the mass, damping and stiffness matrices of the k_ith beam element. $\{d_{bi}\}$ is the nodal displacement vector of this element and $\{f_{bi}\}$ is the vector of the nodal external forces. $\{f_{bci}\}_{t+\Delta t}$ is the vector of the equivalent nodal forces resulted from $V_{i,t+\Delta t}$ (contact) force. So, these equivalent nodal forces using interpolation functions, as applied in finite element analysis, can be expressed as

$$\{f_{bci}\}_{t+\Delta t} = \{N_{ci}^h\}H_{i,t+\Delta t} + \{N_{ci}^v\}V_{i,t+\Delta t} \quad (5.8)$$

where $\{N_{ci}^h\}$ and $\{N_{ci}^v\}$ are the interpolations functions related to horizontal and vertical DOFs. $H_{i,t+\Delta t}$, the horizontal contact force can be found out from the following formula

$$H_{i,t+\Delta t} = \mu_i V_{i,t+\Delta t} \quad (5.9)$$

Here, μ_i is the friction coefficient between wheel and rail. Now using Eq. 5.6 and Eq. 5.8, Eq. 5.7 can be arranged as follows,

$$\begin{aligned}&[m_{bi}]\{\ddot{d}_{bi}\}_{t+\Delta t} + [c_{bi}]\{\dot{d}_{bi}\}_{t+\Delta t} + [k_{bi}]\{d_{bi}\}_{t+\Delta t} \\ &= \{f_{bi}\}_{t+\Delta t} - \sum\left([m^*_{cij}]\{\ddot{d}_{bj}\} + [c^*_{cij}]\{\dot{d}_{bj}\} + [k^*_{cij}]\{d_{bj}\}\right) \\ &- \{p^*_{ci}\}_{t+\Delta t} - \{q^*_{ci}\}_t\end{aligned} \tag{5.10}$$

where the matrices with an asterisk are calculated using contact matrices and interpolation vectors [Yang *et al*. (2004)], where the only unknowns are related to bridge.

In the preceding sections, VBI elements were introduced and the effect of vehicle load was incorporated in the asterisks matrices. The rest of bridge elements that are free of vehicle loads are treated as original beam elements. Versatility of the VBI element is such that it can be easily assembled into the whole bridge structural matrices, i.e. stiffness, damping and mass matrices. Consider the equation of motion for the entire bridge as follows:

$$[M]\{\ddot{D}\}_{t+\Delta t} + [C]\{\dot{D}\}_{t+\Delta t} + [K]\{D\}_{t+\Delta t} = \{F_b\}_{t+\Delta t} - \{P^*_c\}_{t+\Delta t} - \{Q^*_c\}_t \tag{5.11}$$

where $\{D\}$ represents the displacement matrix, [M], [C], [K] are the assembled structural matrices. $\{F_b\}$ is the vector of external forces, and $\{P^*_c\}$ and $\{Q^*_c\}$ are the equivalent contact forces in global coordinates, which can be solved for the bridge responses as well as for vehicle responses through the use of Eq. 5.3 to Eq. 5.5. The assembled matrices can be obtained from

$$\begin{aligned}[M] &= [M_b] + [M^*_c] = \sum[m_{bi}] + \sum\sum[m^*_{cij}] \\ [C] &= [C_b] + [C^*_c] = \sum[c_{bi}] + \sum\sum[c^*_{cij}] \\ [K] &= [K_b] + [K^*_c] = \sum[k_{bi}] + \sum\sum[k^*_{cij}]\end{aligned} \tag{5.12}$$

where $[M_b]$, $[C_b]$, $[K_b]$are the structural matrices of the bridge which is free of any vehicle loads. Similarly,$[M^*_c]$, $[C^*_c]$, $[K^*_c]$are the contact matrices which includes the effect of the VBI elements in the global coordinate. In addition, vectors for global contact forces can be assembled as

$$\{P^*_c\}_{t+\Delta t} = \sum\{p^*_c\}_{t+\Delta t}\,; \quad \{Q^*_c\}_t = \sum\{q^*_c\}_t \tag{5.13}$$

5.2.2. Train load, OWG and Equivalent beam model

The train loads have been considered as SBL and MBL. SBL is comprised of 4 axles, load on each axle is 25T, with total load of each bogie 100T. The MBL is series of SBL and are placed such a distance apart that the equivalent UDL on the OWG becomes 9.33 T/m, the standard equivalent UDL corresponding to 25T axle of 2008, as per IRS. The SBL is shown in Fig. 5.2 (a) and MBL in Fig. 5.2 (b),

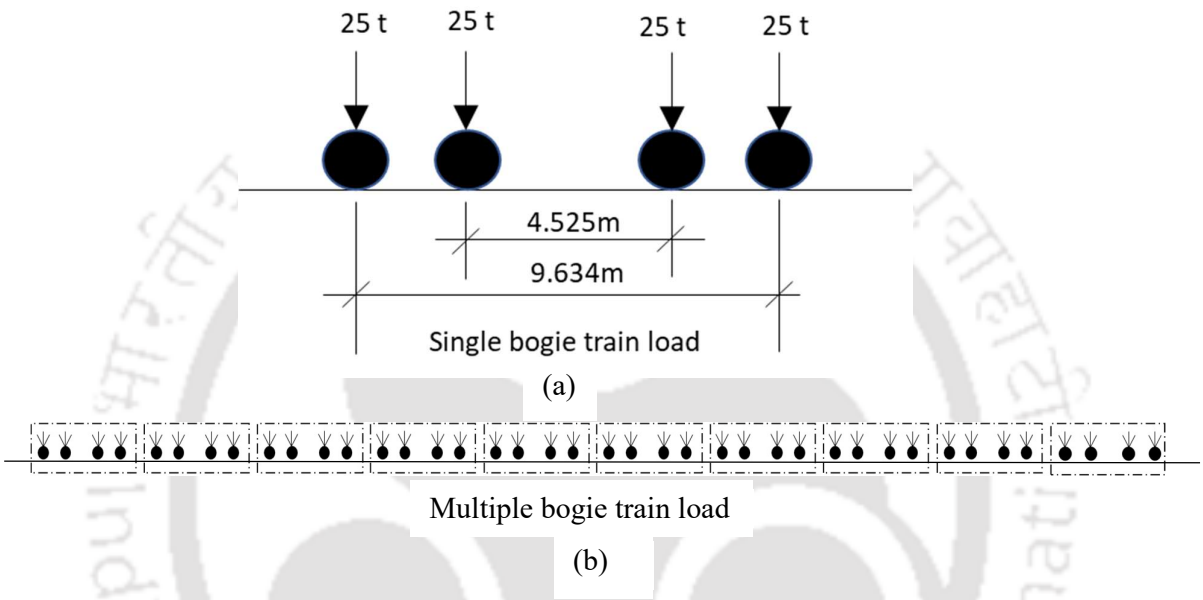

Fig. 5.2. (a) Single bogie load (SBL)and (b) Multiple bogie load (MBL) configuration

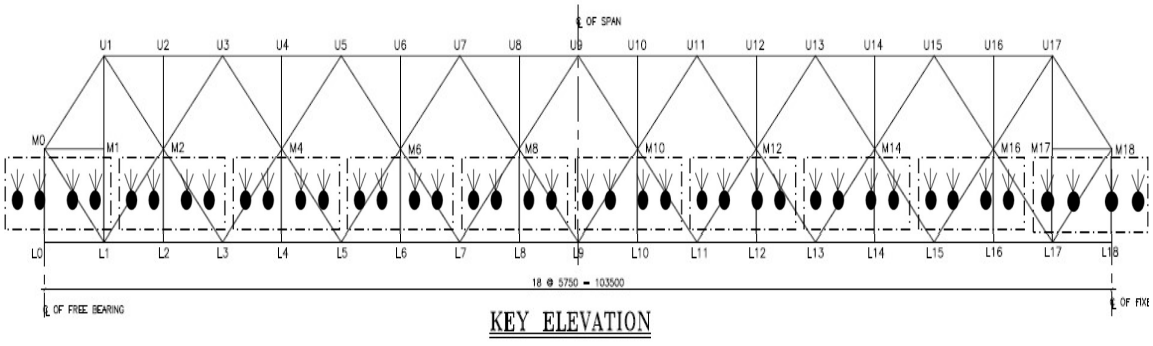

Fig. 5.3. OWG of 103.5m span showing MBL position

The MBL on OWG of 103.5m span is shown in Fig. 5.3. The TMD applied on OWG is placed at the mid-span of each of the two parallel trusses, 8.5m apart.

5.2.3. Application of TMD and Optimization of parameters

Three parameters of TMD, which influence the response of the structure are the mass *m*, stiffness *k* and the damping *c* of the TMD.

The mass of TMD is considered as a fraction of the total mass of the system. It cannot be very high as the same will lead to increase in static response of the structure. The value is generally considered between 0.5% - 2%.

The frequency of vibration of the TMD for attaining most effective reduction of dynamic response should remain very close to the first fundamental frequency of the structure in the corresponding direction, which in the present case is vertical direction. Thus, the frequency ratio has been considered varying between 0.995 to 1.05.

The damping ratio of the TMD has been considered to be varying between 2% to 10%.

The response of the structure has been studied for optimised TMD parameters. The results have been compared with those with no TMD condition. Optimisation of the parameters have been done by using *fmincon* in MATLAB. While doing optimisation, the track irregularities parameters have been considered as fixed, instead of random, in order to get the convergence in the optimisation results.

The parameters which are optimised are as follows:

$q = [\zeta, f, \mu]$; where,

$\zeta = c/2m\omega_t$, m is mass of TMD and ω_t is the frequency of TMD

$f = \omega_t/\omega_n$, ω_t is the frequency of TMD and ω_n is the first fundamental frequency of the structure in vertical direction

$\mu = m/M$, m is mass of TMD and M is total mass of the structure

The lower bound values are taken as l_b = [0.02, 0.995, 0.005]

Two upper bound limit has been cosidered to check the different TMD parameters and corresponding reductions in deflection:

u_{b1} = [0.1, 1.05, 0.02]

u_{b2} = [0.1, 1.05, 0.01]

The TMD parameters are optimised within the lower and upper bound as per the following expression: $l_b \leq q \leq u_b$

The two optimisations corresponding to two upper limits have been presented as Optimised TMD (1) and Optimised TMD (2) in the subsequent Tables and Figures.

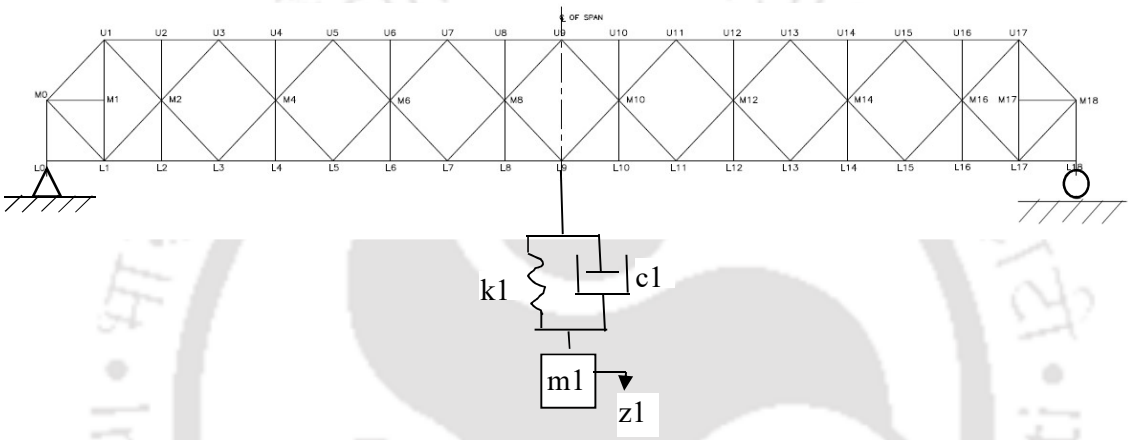

Fig. 5.4. TMD configuration in OWG

Fig. 5.4 shows the OWG along with the TMD at the midspan. Eq. 5.14 and 5.15 are the governing equations of single TMD applied at the i^{th} DOF of the structure.

$$m_{ii}\ddot{y_i} + (c_{ii} + c_1)\dot{y_i} - c_1\dot{y_1} + (k_{ii} + k_1)y_i - k_1y_1 = F_i \quad (5.14)$$

$$m_1\ddot{y_1} - c_1\dot{y_i} + c_1\dot{y_1} - k_1y_i + k_1y_1 = f_1 \quad (5.15)$$

5.3. Results and Discussion

5.3.1. Effect of TMD on 103.5m span OWG model with SBL

The speed *vs* mid-span deflection has been plotted in Fig. 5.5 for OWG model with SBL to understand the speeds at which the deflection is maximum compared to the other speeds. It has been found that there are two local maximum deflection corresponding to speed 250 kmph and 400 kmph. The global maximum deflection occurs at speed 750 kmph. Thus, the effect of TMD has been performed for four different speeds of SBL, namely, 180 kmph

which is the normal maximum speed of train, 250 kmph, 400 kmph and 750kmph. The higher velocities are considered to understand the effect of TMD against the speed at which maximum deflection occurs compared to the other speeds.

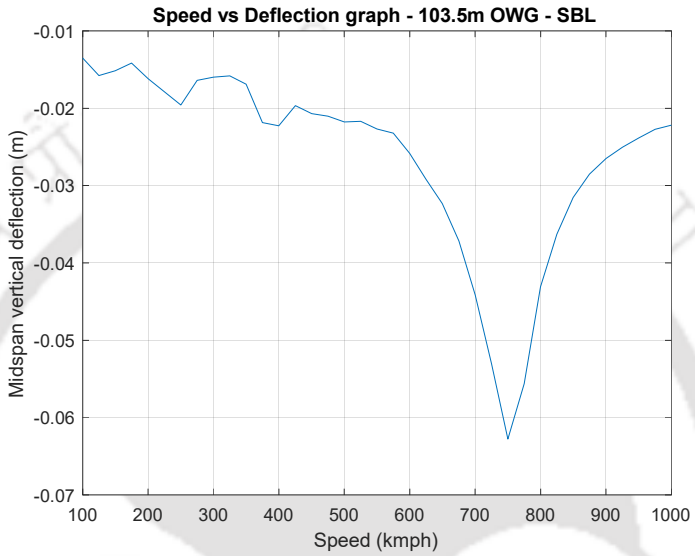

Fig. 5.5. Midspan vertical deflection at different speed for 103.5 m span OWG with SBL

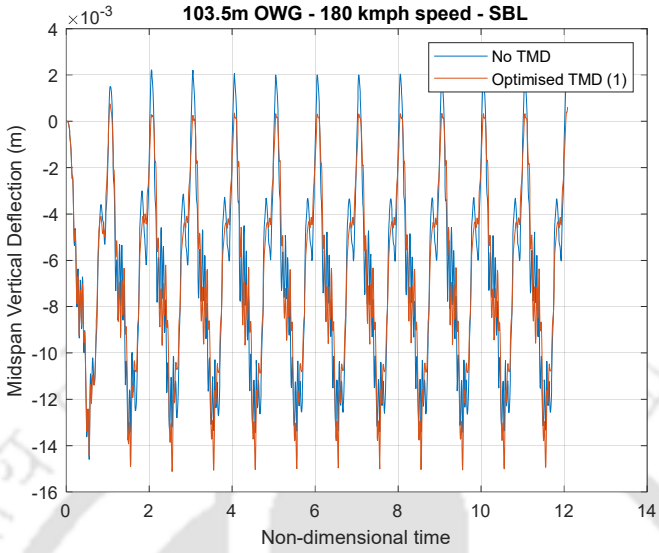

Fig. 5.6. Midspan deflection graphs of 103.5 m span OWG with SBL at 180 kmph

Table 5.1. Midspan deflection values of 103.5 m span OWG with SBL at 180 kmph

Sl. No.	Mass ratio	Frequency ratio	Damping ratio	Midspan deflection (mm)	Reduction in deflection	Criteria
1	-	-	-	13.4	-	No TMD
2	1.98%	1.011	4.5%	15.0	-12%	Optimised TMD (1)

From Fig. 5.6 and Table 5.1, it can be seen that for 180 kmph speed, the effect of TMD is negative. For 1.98% mass, the reduction is -12%.

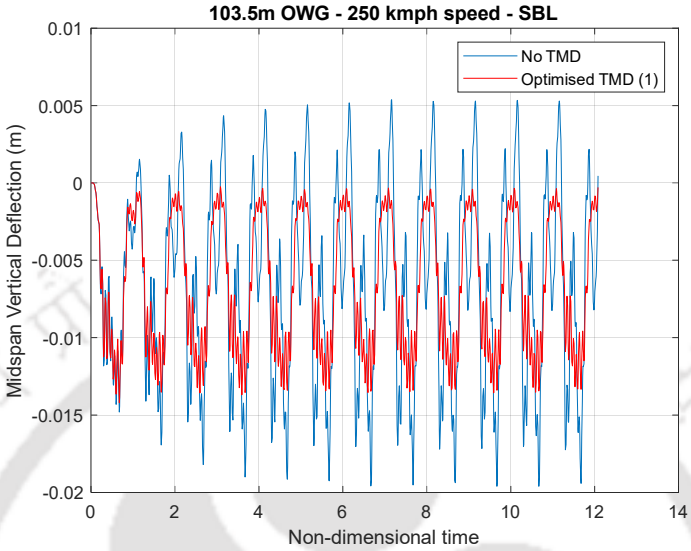

Fig. 5.7. Midspan deflection graphs of 103.5 m span OWG with SBL at 250 kmph

Table 5.2. Midspan deflection values of 103.5 m span OWG with SBL at 250 kmph

Sl. No.	Mass ratio	Frequency ratio	Damping ratio	Midspan deflection (mm)	Reduction in deflection	Criteria
1	-	-	-	19.70	-	No TMD
2	1.2%	1.0198	5%	15.6	20.8%	Optimised TMD (1)
3	0.6%	1.0197	4.99%	16.5	16.2%	Optimised TMD (2)

From Fig. 5.7 and Table 5.2, it can be seen that for 250 km speed, which is a speed corresponding to a local peak in deflection (Refer Fig. 5.5) with SBL, the effect in reduction in deflection has significantly improved. It can be seen that with 1.2% mass, reduction is 20.8% and for 0.6% mass, reduction is 16.2%. The graph has been shown for Optimised TMD (1) only for clarity and the same has been maintained in all subsequent graphs.

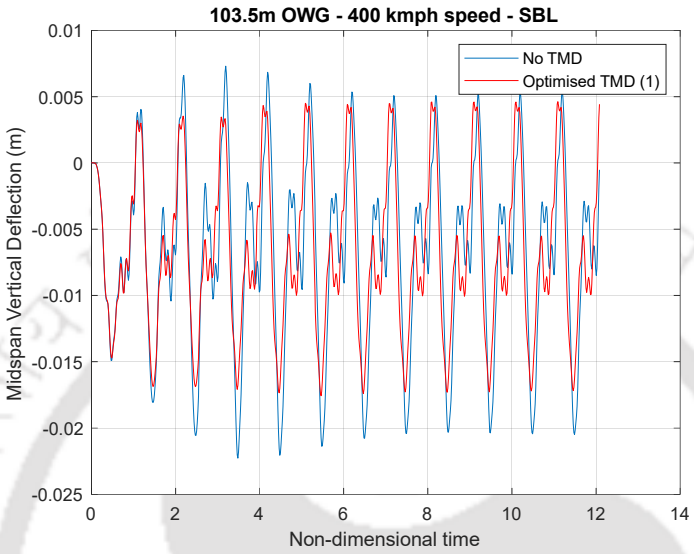

Fig. 5.8. Midspan deflection graphs of 103.5 m span OWG with SBL at 400 kmph

Table 5.3. Midspan deflection values of 103.5 m span OWG with SBL at 400 kmph

Sl. No.	Mass ratio	Frequency ratio	Damping ratio	Midspan deflection (mm)	Reduction in deflection	Criteria
1	-	-	-	22.27	-	No TMD
2	1.76%	1.0216	4.02%	16.9	24%	Optimised TMD (1)
3	0.6%	1.0198	5%	19.7	11.5%	Optimised TMD (2)

From Fig. 5.8 and Table 5.3, it can be seen that for 400 km speed, which is also a local peak of deflection as per Fig. 5.6 with SBL, the effect in reduction in deflection is also substantial. It can be seen that for 1.76% mass, the reduction in deflection is 24% and for 0.6% mass, the reduction is 11.5%.

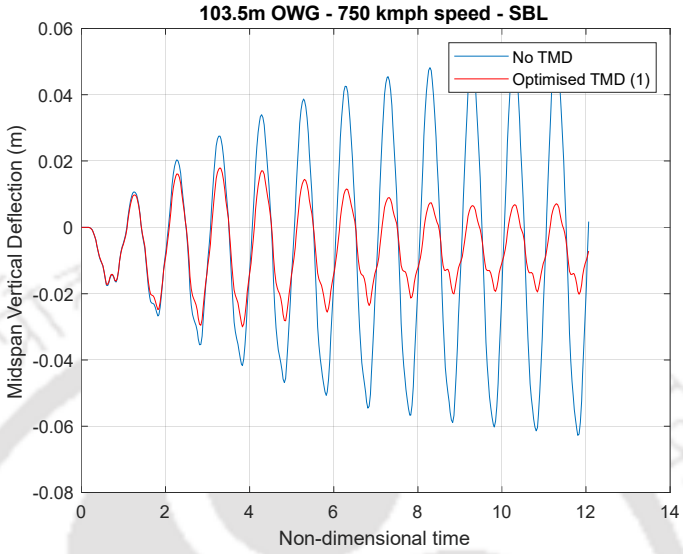

Fig. 5.9. Midspan deflection graphs of 103.5 m span OWG with SBL at 750 kmph

Table 5.4. Midspan deflection values of 103.5 m span OWG with SBL at 750 kmph

Sl. No.	Mass ratio	Frequency ratio	Damping ratio	Midspan deflection (mm)	Reduction in deflection	Criteria
1	-	-	-	62.76	-	No TMD
2	1.84%	1.011	3.27%	30.2	51.9%	Optimised TMD (1)
3	0.92%	1.0108	3.14	36.1	42.5%	Optimised TMD (2)

From Fig. 5.9 and Table 5.4, it can be seen that the effect of TMD is best at 750 kmph. which is the resonance condition, i.e. the frequency of occurrence of the bogie load is same as the fundamental frequency of the structure in vertical direction. It can be seen that with 1.84% TMD mass, the reduction in deflection is about 51.9% and for 0.92% mass, the reduction is 42.5%.

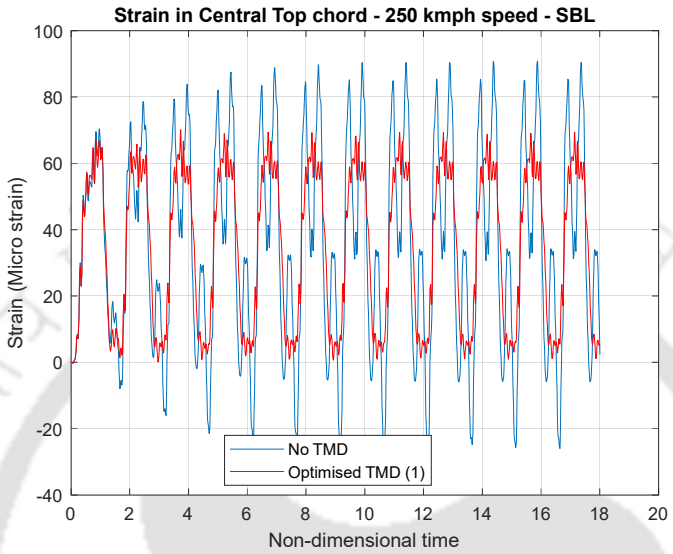

Fig. 5.10. Strain graphs for central top chord of 103.5 m span OWG with SBL at 250 kmph

Table 5.5. Strain values for central top chord of 103.5 m span OWG with SBL at 250 kmph

Sl. No.	Mass ratio	Frequency ratio	Damping ratio	Strain (Micro strain)	Reduction in deflection	Criteria
1	-	-	-	89.95	-	No TMD
2	1.2%	1.0198	5%	69.40	22.8%	Optimised TMD (1)

Strains in top chord and bottom chord members have been plotted for the same optimised parameters (Optimised TMD 1), which have been obtained in case of deflection. From Fig. 5.10 and Table 5.5, it can be seen that for 250 kmph speed, the reduction in strain in central top chord is similar to that obtained in deflection. The reduction in strain is 22.8% as against reduction in midspan deflection is 20.8 % (Table 5.2). In all the strain calculation, only Optimisation (1) results have been shown as results are almost similar to that is obtained for deflection.

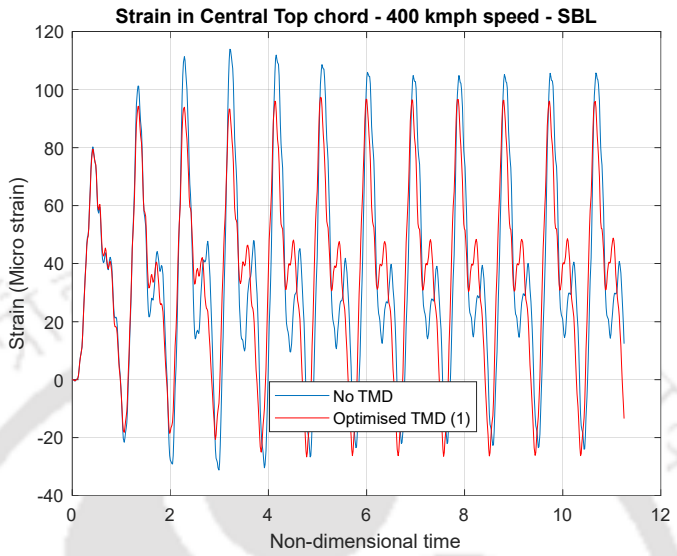

Fig. 5.11. Strain graphs for central top chord of 103.5 m span OWG with SBL at 400 kmph

Table 5.6. Strain values for central top chord of 103.5 m span OWG with SBL at 400 kmph

Sl. No.	Mass ratio	Frequency ratio	Damping ratio	Strain (Micro strain)	Reduction in deflection	Criteria
1	-	-	-	113.83	-	No TMD
2	1.76%	1.0216	4.02%	97.32	14.7%	Optimised TMD (1)

From Fig. 5.11 and Table 5.6, it can be seen that for 400 kmph speed, the reduction in strain in central top chord is less compared to that of deflection. The reduction in strain is 14.7% as against reduction in deflection which is 24% (Table 5.3).

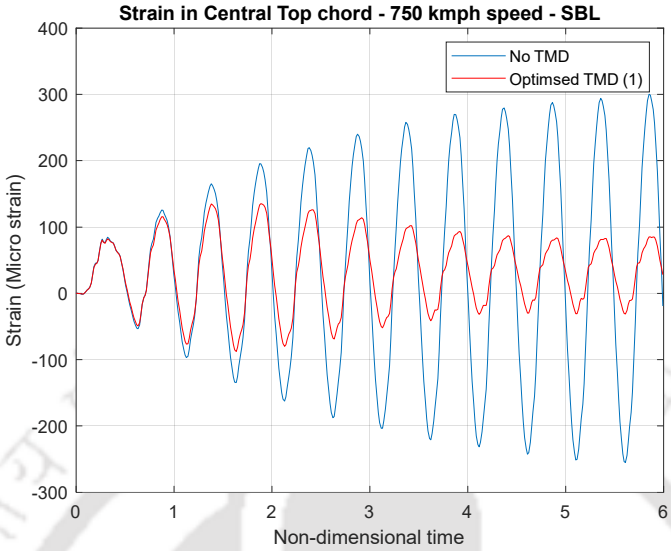

Fig. 5.12. Strain graphs for central top chord of 103.5 m span OWG with SBL at 750 kmph

Table 5.7. Strain values for central top chord of 103.5 m span OWG with SBL at 750 kmph

Sl. No.	Mass ratio	Frequency ratio	Damping ratio	Strain (Micro strain)	Reduction in deflection	Criteria
1	-	-	-	298.7	-	No TMD
2	1.84%	1.011	3.27%	130.5	56.3%	Optimised TMD (1)

From Fig. 5.12 and Table 5.7, it can be seen that the effect of TMD is best at 750 kmph and the reduction in strain in central top chord is almost same of that for deflection. It can be found that with 1.84% TMD mass, the reduction in strain is 56.3% as against reduction in deflection 51.9% (Table 5.4).

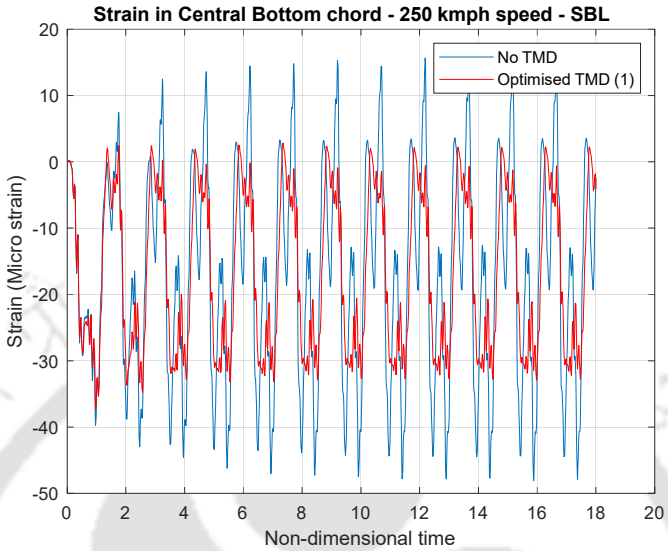

Fig. 5.13. Strain graphs for central bottom chord of 103.5 m span OWG with SBL at 250 kmph

Table 5.8. Strain values for central bottom chord of 103.5 m span OWG with SBL at 250 kmph

Sl. No.	Mass ratio	Frequency ratio	Damping ratio	Strain (Micro strain)	Reduction in deflection	Criteria
1	-	-	-	47.70	-	No TMD
2	1.2%	1.0198	5%	38.24	19.8%	Optimised TMD (1)

From Fig. 5.13 and Table 5.8, it can be seen that for 250 km speed, the reduction in strain in central bottom chord is similar to that obtained in deflection. It can be seen that with 1.2% mass, the reduction in strain is 19.8% as against reduction in deflection 20.8% (Table 5.2)

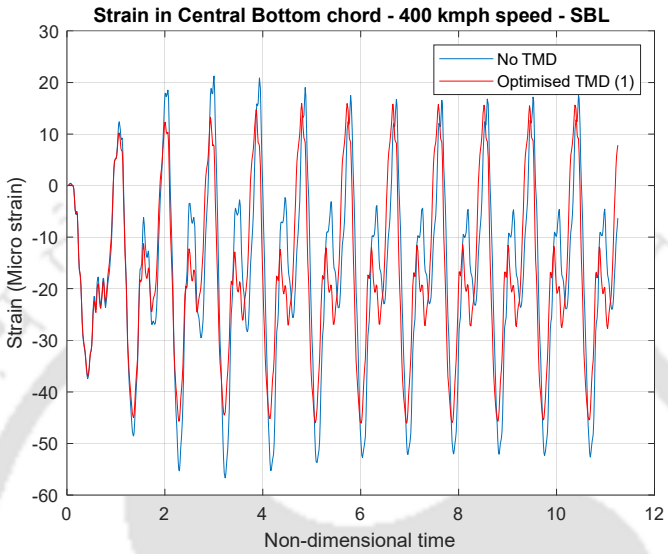

Fig. 5.14. Strain graphs for central bottom chord of 103.5 m span OWG with SBL at 400 kmph

Table 5.9. Strain values for central bottom chord of 103.5 m span OWG with SBL at 400 kmph

Sl. No.	Mass ratio	Frequency ratio	Damping ratio	Strain (Micro strain)	Reduction in deflection	Criteria
1	-	-	-	56.66	-	No TMD
2	1.76%	1.0216	4.02%	45.43	19.8%	Optimised TMD (1)

From Fig. 5.14 and Table 5.9, it can be seen that for 400 km speed, the reduction in strain in central bottom chord is almost similar to that obtained in deflection. It can be seen that with 1.76% mass, the reduction in strain is 19.8% as against reduction in midspan deflection 24% (Table 5.3).

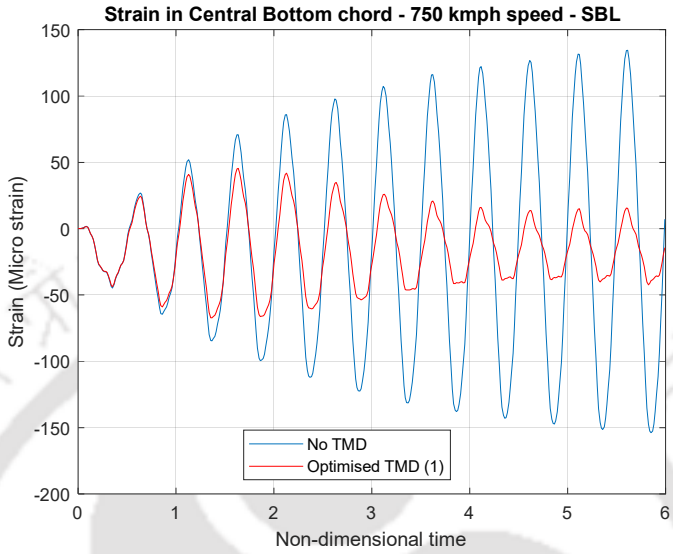

Fig. 5.15. Strain graphs for central bottom chord of 103.5 m span OWG with SBL at 750 kmph

Table 5.10. Strain values for central bottom chord of 103.5 m span OWG with SBL at 750 kmph

Sl. No.	Mass ratio	Frequency ratio	Damping ratio	Strain (Micro strain)	Reduction in deflection	Criteria
1	-	-	-	153.9	-	No TMD
2	1.84%	1.011	3.27%	67.1	56.4%	Optimised TMD (1)

From Fig. 5.15 and Table 5.10, it can be seen that the effect of TMD is best at 750 kmph and the reduction in strain in central bottom chord is almost same of that for deflection. It can be found that with 1.84% TMD mass, the reduction in strain is about 56.4% as against reduction in midspan deflection 51.9% (Table 5.4).

From the above results of effect of TMD in reducing the vehicle induced vibration response of OWG span for SBL condition, it is found that the effect is most predominant at 750 kmph speed. It can be seen that the resonance condition occurs at this speed as the frequency of occurrence of SBL matches with the fundamental frequency of the structure in vertical direction. The SBL acts as a concentrated load on the span as the width of the SBL which is 9.634m (Fig. 5.2(a)) compared to the span length of the OWG which is 103.5m, is very less. It has been found that at 180 kmph speed, the TMD effect is negative, ie the midspan defection is more when TMD is applied. This result also corroborates with the findings of the studies by Heyder (2015), where he showed that at some speed range beyond the speed at which resonance occurs, caused negative effect of TMD.

5.3.2. Effect of TMD on 103.5m span OWG model with MBL

The speed *vs* midpan deflection curve has been plotted as shown in Fig. 5.16 in OWG model with MBL.

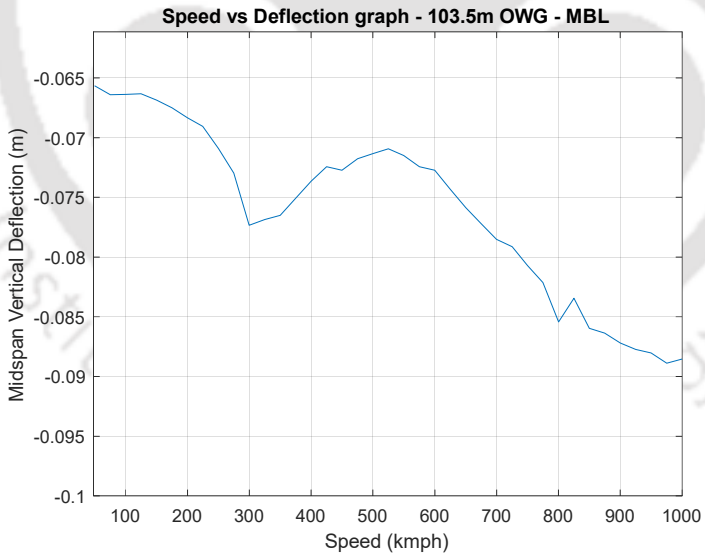

Fig. 5.16. Midspan vertical deflection at different speed for 103.5 m span OWG with MBL

It has been found that there is one local maximum corresponding to speed 300 kmph. Beyond this speed, deflection increases almost continuously. Thus the effect of TMD has been evaluated for two different speeds of MBL, namely, 180 kmph which is the normal maximum speed of train and 300 kmph.

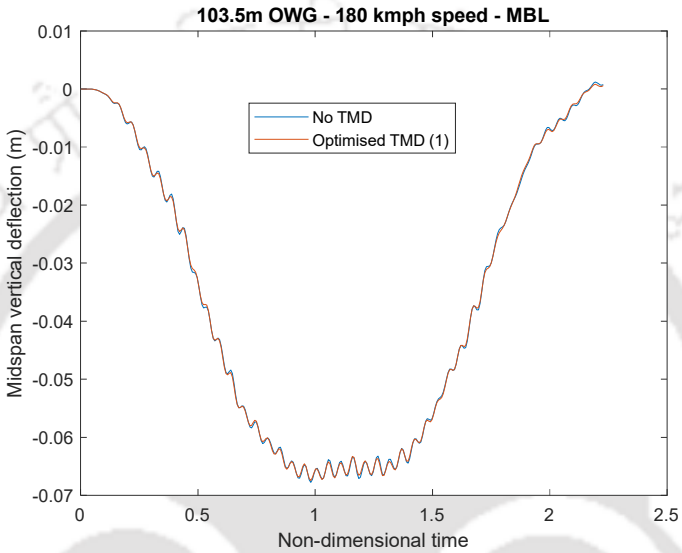

Fig. 5.17. Mid-span deflection for 103.5 m span OWG with MBL at 180 kmph

Table 5.11. Mid-span deflection of 103.5 m span OWG with MBL at 180 kmph

Sl. No.	Mass ratio	Frequency ratio	Damping ratio	Midspan deflection (mm)	Reduction in deflection	Criteria
1	-	-	-	67.79	-	No TMD
2	1.98%	1.011	4.55%	67.4	0.6%	Optimised TMD (1)

From Fig. 5.17 and Table 5.11, it can be seen that for MBL in OWG with 180 kmph speed, there is no effect of TMD in reduction in deflection. With 1.98% TMD mass, the reduction in deflection is only 0.6%.

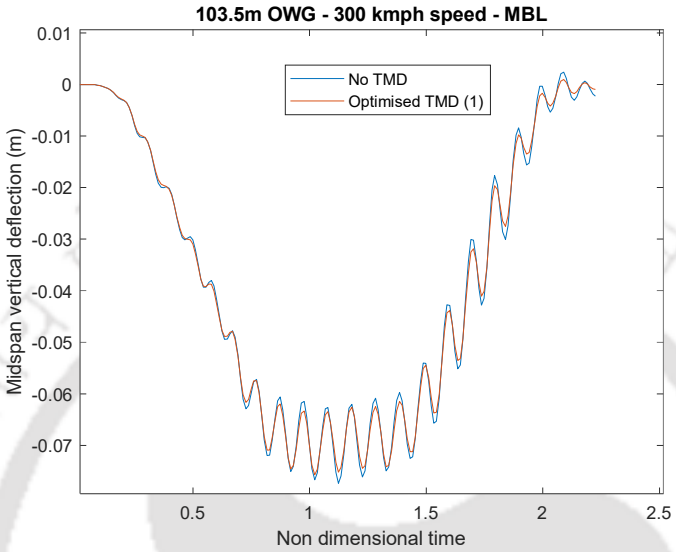

Fig. 5.18. Mid-span deflection for 103.5 m span OWG with MBL at 300 kmph

Table 5.12. Mid-span deflection of 103.5 m span OWG with MBL at 300 kmph

Sl. No.	Mass ratio	Frequency ratio	Damping ratio	Midspan deflection (mm)	Reduction in deflection	Criteria
1	-	-	-	77.34	-	No TMD
2	1.95%	1.018	3.9	75.7	2.12%	Optimised TMD (1)

From Fig. 5.18 and Table 5.12 it can be seen that for 300 kmph speed the effect of TMD is also insignificant. With 1.95% mass, the reduction in deflection is only 2.12%.

From the above results of effect of TMD in reducing the vehicle induced vibration response of OWG span for MBL condition, it is found that at no speed within the considered range, the TMD is becoming effective. As such, the presence of MBL in the long span OWG being considered is almost acting as a uniform distributed load and hence resonance effect does not occur. This leads to performance of TMD insignificant in terms of reducing vehicle induced vibration response in vertical direction.

5.4. Concluding remarks

The effect of SBL on the OWG has been found predominant as per the above study. However, in case of MBL, the effect is found to be insignificant for the range of speed considered for the running train. The basic reason behind these results is that for SBL case, the load is acting almost like a concentrated load as the length of a bogie is smaller compared to the span length (Wheel spread of SBL is 9.634m whereas the span length is 103.5m). Due to this reason, resonance can occur for some specific speed at which the frequency of occurrence of SBL matches with the fundamental frequency of the structure in vertical direction. As the effect of TMD is most predominant when the frequency of occurrence of load remains within some close zone of the fundamental frequency of structure, the results with SBL is significant. In case of MBL, as the entire span length is covered with the loads, effect of resonance is not occurring. As a result, the effect of TMD with MBL condition is not significant.

From the speed *vs* deflection graph, it can be seen (Fig. 5.5) that under SBL condition, maximum deflection occurs at 750 kmph speed. It can be found that at this speed, the frequency of occurrence of SBL matches closely with the fundamental frequency of the structure and causes resonance. Some local peaks are visible at 250kmph and 400 kmph speed. However below 250kmph speed, the speed *vs* deflection graph is flat. From the results it can be found that at 180kmph, the effect TMD is Nil. This result also corroborates with the findings of the studies by Heyder (2015), where he showed that at some speed range beyond the speed at which resonance occurs, caused negative effect of TMD. The positive effects occurs at 250kmph and beyond. Maximum effect is visible at the resonance speed, i.e. at 750kmph. Two cases of optimisation was done, one for TMD mass ratio less than 1% and the other is for TMD mass ratio between 1% and 2%. At 250kmph speed the reduction in midspan deflection is 16.2% against 0.6% TMD mass ratio. The same value is 20.8% against 1.2% TMD mass ratio. At 400kmph speed the reduction in midspan deflection is 11.5% against 0.6% TMD mass ratio. The same value is 24% against 1.76% TMD mass ratio. The maximum effect is at 750kmph speed at which the reduction in midspan deflection is 42.5% against 0.92% TMD mass ratio and 51.9% against 1.84% TMD mass ratio. For the above cases the optimised damping ratio lies between 3% to 5%.

In case of MBL, the speed *vs* deflection graph (Fig. 5.16) shows that a local peak occurs at 300 kmph speed. However, the deflection almost increases monotonically with higher speeds. As such, no resonance condition occurs under MBL condition. As a result, the effect of TMD has been found almost Nil in case of MBL.

The results of midspan deflection and the strains at central top chord and bottom chord show similar trend in terms of effectiveness of TMD under SBL loading with speed above 250kmph.

Literature survey shows that in all the previous studies, the bridge length is small compared to the wheel distance of the load. Span lengths were varying up to 40m. Corresponding wheel configuration considered by them is such that even if MBL condition is considered, the effect of resonance is occurring at some speeds and as a result, significant effect of TMD has been reported by them. However, no study has been done till date on long span bridges and as such from the results obtained, it can be concluded that, TMD is not effective to reduce vehicle induced vertical vibration response of long span OWG rail bridges.

Chapter 6

Summary and Conclusions

6.1. Summary

Bridges are integral part of a transportation system of a country and proper design and construction of bridges is highly important for advancement of the Nation. There are guidelines for the design and construction of bridges based on the technical knowledge and standard practices prevailing in the country. However, further studies may be necessary for some special cases for better understanding of the behaviour of the structure to ensure safety and economy. Northeast Frontier Railway (NFR) has envisaged to connect the Northeast states of India which are hitherto not connected in a complete way. The railway lines pass through eastern trail of Himalaya resulting construction of large number of tunnels and bridges. The bridges are meant to cross the deep gorges resulting in tall piers ranging from 20m to 141m height and multiple number of OWG of steel superstructure of 103.5m span. The entire area is under highest seismic zone. The design of the bridges has been done using the available codes and standards. However, it was felt that some of the guidelines laid in the standards are not adequately covering some aspects for design and as a result, conservative design parameters are chosen, which may lead to uneconomic design. With these aspects in mind, some focus area have been identified for further study which comprised the present thesis work. The topics are namely: 1) Response reduction factor of large diameter hollow circular pier section, 2) Asynchronous ground motion and its effect on response of tall pier railway bridges and 3) TMD and its effect on vehicle induced vertical response of long span OWG railway bridges.

Literature study shows that adequate research material is available on the response reduction factor R of hollow section with dimension ranging from 400mm square to 800mm diameter with wall thickness ranging between 100mm to 250mm. It was felt that the effect of confinement width may play a significant role in the value of R. In the case of piers designed in the railway link project in Northeast states, the hollow circular pier diameters range between 4m to 16m with wall thick varying between 0.5m to 2.0m. Moreover, the

pier sections have door openings at the bottom and top to enable inspection of inside surface of pier for maintenance purpose. It has been felt that further study may be useful to understand the effect of thickness of large diameter hollow pier section on *R*. Moreover, no study is available on the effect of wall opening in hollow circular section on *R*.

M-ϕ curve has been generated for hollow circular pier section based on the various parameters like axial load (P/Af_{ck}), main steel ratio (ρ_{cc}) and transverse steel ratio (ρ_s). The stress-strain curve for concrete has been taken from the model of Mander *et al*. (1988). This model is based on behaviour of both rectangular and circular section. The proposed theoretical model was validated using experimental findings. However, the model is based on solid section of column and accordingly the confinement effective coefficient (k_e) is applicable for solid section only. The expression of k_e for hollow circular section has been proposed in the present study. Full scale FE model has been simulated for hollow circular pier section and has been analysed in Abaqus. The unconfined stress-strain graph of concrete as per Mander's model has been given as input to the FEA. The stress-strain relation as obtained from the FEA has been compared with the stress-strain relation given by Mander *et al*. (1988) incorporating the expression of proposed k_e and has been found to agree quite well. This authenticates the proposed expression of k_e.

The ultimate concrete strain has been adopted from strain energy balance approach of the concrete section at which first fracture occurs at confining steels as per Mander *et al.* (1988). The *M*-ϕ curves for the pier sections have been generated restricting the ultimate strain in concrete to the above value. Yield curvature and ultimate curvature have been calculated from the *M*-ϕ curve which gives the curvature ductility and deflection ductility of the section. Instead of calculating the ductility from the average length of plastic hinge, the actual area under the *M*-ϕ curve has been considered.

The presence of uncracked section in between two cracked section provides some stiffening action of the pier and the same has been taken into consideration while estimating the overall ductility of the hollow circular pier. The *P*-Δ effect has been included while estimating the ultimate curvature and corresponding ultimate moment. The effect of grade of concrete (f_{ck}) and grade of steel (f_y) on *R* have been studied. The effect of spacing of transverse steel (S_h), diameter of the transverse steel has also been studied. Effect of

confined width of concrete on *R* has been studied by considering the width varying between 0.5m to 2.0m which are the standard thickness of wall of hollow pier having diameter starting from 4m to 16m.

Effect of opening has been studied by formulating the *M-ϕ* curve for hollow circular section with the specified discontinuity. The same stress-strain relation of concrete which was used for the section without opening has been used here. However, the analysis of FE model with wall opening shows reduction in ultimate concrete strain and thus the *R* values proposed for the section with wall opening has been so adjusted that it satisfies the reduced ultimate concrete strain value.

The slenderness effect plays an important role in the value of *R* for any pier section. The proposed values of *R* in general are applicable for pier with slenderness ratio up to 50. The *M-ϕ* curve is greatly influenced by the nature of stress-strain graph of concrete. The present study is based on stress-strain relation of concrete proposed by Mander *et al*. (1988) which is valid up to M50 grade. Effect of grade of steel is considerable in the value of *R*. The present study is based on the standard grade of steel prevailing in the construction industry which is Fe500 with ultimate tensile strength 700 MPa.

As per established theory, yield reduction factor value is same as deflection ductility when the natural period of the structure is high. Thus, response reduction factor has been calculated by multiplying deflection ductility with reserve strength factor. Attempt has been made to recommend the rational values of *R* for large diameter hollow circular piers based on various design parameters. The value of *R* has also been recommended for hollow circular pier section with wall opening.

The effect of track deflection during transverse seismic forces cause the continuous track to undergo change in curvature which is important to assess for safe movement of train. Analysis with synchronous ground motion is sufficient for bridges with short length, however, in case of long bridges, the effect of asynchronous motion is extremely important to assess the transverse track deflection. The generation of asynchronous ground movement depends on the factors like time of travel of the wave, incoherence effect and the local soil effect at the interface of which the wave propagation gets reflected/ refracted. In the present

case, as the local soil is uniform in between the two extreme abutments of the bridges, this effect is not considered. There are various model of spatial correlation function available to cater for incoherence effect. In general, all the models are a function of few basic parameters namely, distance from the source to the location under consideration, frequency of ground vibration, soil parameter and shear wave velocity of the medium. In the present case, the model suggested by Fenton (1991) has been adopted. Two earthquake events have been considered keeping in parity with the soil parameter of the bridges under study, namely, El Centro earthquake and Koyna earthquake, which are recorded in medium soil and rocky strata respectively. In the present case the bridges are resting on rocky strata. Soil structure interaction model has been generated in SAP. Three different soil spring have been adopted, namely, *P-y* curve to represent interaction between the lateral resistance of soil and pile displacement, *t-z* curve to represent interaction between shaft skin frictional force and relative movement of the pile with respect to the soil, *Q-z* curve to represent the mobilized tip bearing capacity and settlement. Acceleration time history has been converted to displacement time history to give the ground motion input in the pile spring for asynchronous motion as the governing equation requires the displacement time history. The absolute deflection of the pier tops under synchronous and asynchronous ground movement have been obtained from the analysis. Corresponding track curvature is estimated and compared with the safe curvature at which the train can run with its design speed.

The vehicle induced response of the superstructure has been recommended in Indian Railway Standard (IRS) in terms of static equivalent factor varying with respect to span of the member and is applicable for maximum allowable speed of train. The actual vehicle induced response can be obtained by taking into consideration vehicle bridge interaction (VBI) in the analysis. Track irregularity also plays important role in the response. Generally, the vehicle induced response of the superstructure is catered in the design by strengthening the structure. Introduction of TMD may reduce the vehicle induced response under resonant condition of the vehicle induced force. Literature study shows that adequate researches are available on effect of TMD on road bridges of variable span length. Good number of researches are also available on effect of TMD on high speed railway bridges with span length up to 40m. The present railway connection project being undertaken by Indian Railway in the Northeast states are mostly OWG steel structure of span length

103.5m. With these aspects in mind, the present study has been undertaken to assess the effect of TMD on OWG steel long span bridge. The railway prefers simply supported span over continuous one due to the relative ease of maintenance, and thus the same support system has been considered in the present study. Simply supported structure vibrates predominantly in first mode and as a result it is felt that study may be restricted to single TMD at midspan. Following response of the superstructure has been considered to assess the effect of TMD – 1) The midspan deflection, 2) Strain in central top chord and 3) Strain in central bottom chord. The vehicle load has been considered using a 27 DOF vehicle model along with track irregularity. The single bogie load of 100t as recommended in the IRS has been adopted. Both single bogie load (SBL) effect and multiple bogie load (MBL) effect has been considered in the analysis. The MBL has been considered by using series of SBL in such a way that, overall uniform distributed load effect recommended by IRS can be achieved. It has been found that the effect of TMD is significant for the bridge under consideration for SBL for a certain speed above normal speed range. However, the effect of TMD is not at all significant for MBL.

6.2. Conclusion

Major conclusions of the present study may be summarized as follows:

A. On response reduction factor (R) of large diameter hollow circular pier section:

- Confinement effective coefficient (k_e) has been proposed for hollow circular pier section. The stress-strain relation of concrete given by Mander *et al*. (1988) considering this proposed k_e value matches closely with the stress-strain relation found from FE analysis for a full scale model of the pier section under consideration, which suggests the authenticity of the proposed expression of k_e. The confined compressive strength ratio between the manually calculated value with the proposed formula of confinement effective coefficient and that obtained from FEA varies between 0.95 to 0.97.
- The concrete strain corresponding to the ultimate moment capacity of the section remains within the ultimate concrete strain capacity as per the first strain energy

balance approach of the concrete section at which first fracture occurs at confining steels as per Mander *et al.* (1988).

- The spacing of transverse steel plays an important role in the value of *R* and it reduces drastically with spacing more than 150mm.
- Confinement width of concrete has significant effect on the value of *R* due to change in k_e value with respect to confinement width. The proposed value of *R* covers the standard wall thickness of hollow circular pier section.
- The stress-strain graph of concrete near the wall opening shows reduced strain capacity of concrete as compared to that of section without opening.
- Attempt has been made to propose *R* value for pier with large diameter hollow circular section based on design parameters like axial load (P/Af_{ck}), main steel ratio (ρ_{cc}) and transverse steel ratio (ρ_s). The value of *R* increases with increase in transverse steel ratio (ρ_s), with decrease in vertical load (*P/Afck*) and with decrease in main steel ratio (ρ_{cc}). The proposed value of *R* varies from maximum 5.5 to minimum 1.6 depending on the factors as mentioned.
- The proposed *R* values cover circular section without wall opening and with wall opening. The recommended *R* values of hollow circular section with door opening reduces with opening size and the reduction varies from 1 to 0.7 times of the value of *R* corresponding to section without door opening.
- In general, in different codes/ standards, unique value of *R* for different components of structure are recommended. If the values obtained in the present study is compared with the code/ standards recommended values (The value is 3 as per IRS, BIS and IRC), it can be found that for some cases, the code recommended values are either over safe whereas in some other cases the values are inadequate.

B. Asynchronous ground motion and its effect on response of tall pier railway bridges:

- The displacement demand in piers and abutments with asynchronous ground motion has been observed in higher side compared to that of synchronous ground motion.
- Effect of curvature in track due to synchronous motion and asynchronous motion is case sensitive and depends on the characteristics of ground motion itself.

- The desired speed can be achieved in the bridges under consideration in the project in Northeast states for both synchronous and asynchronous ground motion adopted in the study.
- The asynchronous motion need to be considered in the analysis for track deformation study as in some cases of ground motion, it gives higher responses.

C. TMD and its effect on vehicle induced vertical response of long span OWG railway bridges:

- TMD is effective for single bogie loading (SBL) at certain speed above normal speed range adopted in Indian railway for the bridge under consideration. At 180kmph, the effect TMD is Nil. The positive effects occurs at 250kmph and beyond.
- The effect of TMD for SBL is most predominant at speed at which resonance occurs (At 750 kmph speed) i.e. the frequency of occurrence of load matches with the fundamental frequency of structure at vertical direction.
- The effect of TMD under multiple bogie loading is not significant at any speed as the resonance condition does not occur.
- As such it can be concluded that application of TMD is not significant in long span OWG railway bridges.

6.3. Recommendations for future research

Future work may be undertaken in the following areas:

- The value of *R* for high strength concrete of grade between M60 to M120. In case of high strength concrete, the strain capacity varies with the grade of concrete and thus the value of *R* may differ from grade to grade of concrete mix used for the construction of piers.
- The value of *R* for slender pier. Depending on slenderness ratio beyond 50 the *R* value may be a function of slenderness ratio.
- Value of *R* for hollow rectangular section

- VBI to assess lateral stability of train during a seismic event using asynchronous ground motion.
- Active control energy dissipation device instead of passive control device like TMD in reducing response of long span OWG steel bridges.

References

1. Abaqus Documentation, Version 6.14-2 (2018). Dassault Systémes Simulia Corp., Providence.
2. Abouali, S., Shahverdi, M., Ghassemieh, M. and Motavalli, M. (2019). Nonlinear simulation of reinforced concrete beams retrofitted by near-surface mounted iron-based shape memory alloys. *Engineering Structures,* 187:133–148.
3. Adanur, S., Altun, A. C., Başağa, H. B., Kurtulus, S. and Dumanoglu, A. A. (2017). Wave passage effect on the seismic response of suspension bridges considering local soil conditions. *Int. J. Steel Struct.* 17(2), 501–513
4. Antolin, P., Zhang, N., Goicolea, J.M., Xia, H., Astiz, M.A., and Oliva, J. (2013) Consideration of nonlinear wheel–rail contact forces for dynamic vehicle–bridge interaction in high-speed railways. *Journal of Sound and Vibration,* 332(5), pp: 1231-1251.
5. Antoniou, S., Pinho, R. (2004). Development and verification of a displacement-based adaptive pushover procedure. *Journal of Earthquake Engineering*, 8(5):643-661.
6. API. (2008). Recommended Practice for Planning, Designing and Constructing Fixed Offshore Structure. *American Petroleum Institute*.
7. Balamonica, K., Rao, A. R., Sundaran, M. N., Chellapandi, P. and Gopalakrishnan, N. (2015). Experimental studies on CSRDM specimen to validate the use of ritz vectors for the response evaluation of structures subjected to multi-support excitation. *Nucl. Eng. Des.* 282.
8. Balamonica.K., Gopalakrishnan.N. and Ramamohan Rao.A. (2020). Seismic Analysis of Structures Subjected to Spatially Varying Earthquake Using POD Vectors - Experimental and Analytical Studies., *Journal of Earthquake and Tsunami,* Vol. 14, No. 4 (2020) 2050017 (27 pages), World Scientific Publishing Company.
9. Basu Dhiman, Rodda Gopala Krishnany. (2017). Spatial variation and conditional simulation of seismic ground motion. *Bull Earthquake Eng* 16:4399-4426
10. Berrah, K. M. (1993). A modal combination rule for spatially varying ground movement. *Earthq. Eng. Struct. Dyn*. 22, 791–800.
11. Bogdanoff, J.L., Goldberg, J.E. and Schiff, A.J. (1965). The effect of ground transmission time on the response of long structures. *Bull. Seismol. Soc. Am.* 55, 627–640.
12. Burdette, N. J. & Elnashai, A. S. (20080. Effect of Asynchronous Earthquake Motion on Complex Bridges. II: Results and Implications on Assessment. *Journal of Bridge Engineering* 13, 166–172.
13. Burns, N.H. and Siess, C.P. (1962). Load deformation characteristics of beam column connections in reinforced concrete, *Civil Engineering Studies, Structural Research series No. 234*, university of Illinois, 261 pp.
14. Cardone Donatello, (2014). Displacement limits and performance displacement profiles in support of direct displacement-based seismic assessment of bridges. *Earthquake Engineering & Structural Dynamics*, 43:1239–1263

15. Caltrans (2013). *California Department of Transportation*, Seismic design Criteria
16. Cao, V. V. and Ronagh, H. R.. A (2013). Model for damage analysis of concrete. *Advances in concrete construction,* 1(2):187, 2013.
17. Chan, W.W.L. (1955). The ultimate strength and deformation of plastic hinges in RC frameworks. *Magazine of concrete research,* Vol 7, No. 21, pp 121-132.
18. Chopra Anil K. (2007). Dynamics of structures. *Prentice Hall.*
19. Clough, R.W. and Penzien. J. (1975), Dynamics of structures, *McGraw-Hill, New York,* 634 pp.
20. Constantinou, C. Michael and Quarshie, K. Joseph, (1998). Response Modification Factors for Seismically Isolated Bridges. *MCEER*-98-0014
21. Cusson Daniel and Paultrem Patrick, (1995). Stress-strain model of confined high strength concrete. *Journal of Structural Engineering*, 1995, 121:468-477, ASCE
22. Delgado, R. M. and Santos, S. M. dos. (1997). Modelling of railway bridge-vehicle interaction on high speed tracks. *Computers & Structures,* vol. 63, no. 3, pp. 511–523.
23. Dumanogluid, A. A. and Soyluk, K. (2003). A stochastic analysis of long span structures subjected to spatially varying ground motions including the site-response effect. *Engineering Structures* **25**, 1301–1310.
24. FEMA 356 (2000). Prestandard. *US Federal Emergency Management Agency, 2000.* 2–15.
25. Fenton, G. & Vanmarcke, E. H. A. (1991). Conditioned simulation of local fields of earthquake ground motion. *Structural Safety* 10, 247–264.
26. Frahm, H. (1909). Device for Damped Vibrations of Bodies. *US patent No. 989958*.
27. Fr´yba L. (1996). Dynamics of Railway Bridges. *Thomas Telford Publishing*, Prague, Czech Republic.
28. Green, M. F. and Cebon, D. (1997). Dynamic interaction between heavy vehicles and highway bridges. *Computers & Structures,* vol. 62, no. 2, pp. 253–264.
29. Hetenyi, M. (1946). Beams on Elastic Foundation: Theory with Applications in the Fields of Civil and Mechanical Engineering.
30. Heydar Beygi, (2015). Vibration control of a high-speed railway bridge using multiple tuned mass damper. *Master Thesis, Royal Institute of Technolguy. KTH, Department of Civil and Architectural Engineering*, Stockholm, Sweden.
31. Hoshikuma, J. & Priestley, M.J.N (2000). Flexural behaviour of circular hollow columns with a single layer of reinforcement under seismic loading. *Report No. SSRP-2000/ 13, University of California, San Diego, La Jolla, CA*.
32. Inbanathan, M. J. and Wieland, M. (1987). Bridge vibrations due to vehicle moving over rough surface. *Journal of Structural Engineering,* vol. 113, no. 9, pp. 1994–2008.
33. IRC 112 (2020). Code of practice for concrete road bridges. *Indian Road Congress.*
34. IRS Bridge Rules (2014). Rules specifying the loads for design of super-structure of bridges and for assessment of the strength of existing bridges. *Government of India, Ministry of Railways (Railway Board)* - Indian Railway Standrad
35. IS 13920 (2016). Ductile design and deatiling of RC structures subjected to seismic forces – code of practice. *Bureau of Indian Standards*
36. IS 1893 (2016). Criteria for Earth Quake Resistnat Design ofd Structures – Part 1, General Provisions and Buidings. *Bureau of Indian Standards*

37. Jianzhong Li, Mubiao Su and Lichu Fan. (2005). Vibration control of railway bridges under high-speed train using multiple tuned mass dampers. *Journal of Bridge Engineering, ASCE*, 10(3): 312-320.
38. Kahya, V. and Araz, O. (2017). Series tuned mass dampers in train-induced vibration control of railway bridges. *Struct. Eng. Mech.,* 61(4), 453-461
39. Kanai, K. (1957). Semi-empirical formula for the seismic characteristics of ground. *Bulletin of the Earthquake Research Institute*, Tokyo University, Vol. 35, pp. 308-325.
40. Kappos, J. Andreas, (1999). Evaluation of behaviour factors on the basis of ductility and overstrength studies. *Engineering Structures***,** 21 (1999) 823–835
41. Kappos, J. Andreas, Themelina S. Paraskeva and Ioannis F. Moschonas, (2013). Response Modification Factors for Concrete Bridges in Europe. *ASCE Bridge engineering*, 18(12): 1328-1335
42. Kent, D.C. and Park, R. (1971). Flexural members with confined concrete. *Journal of Strctural Div. , ASCE*, Vo. 97, ST7, July 1971, pp 1969-1990
43. Kim Tao-Hoon, Dai-Jeong Seong and Hyun Mock Shin, (2012). Seismic performance assessment of hollow reinforced concrete and prestressed concrete bridge columns. *International Journal of Concrete Structures and Materials*, Vol 6, No. 3.
44. Kiureghian, A. D. E. R. and Neuenhofer, A. (1992). Response spectrum method for multisupport seismic excitations. *Earthq. Eng. Struct. Dyn*. 21, 713–740.
45. Konakli, K. and Der Kiureghian, A. (2012). Simulation of spatially varying ground motions including incoherence, wave-passage and differential site - response effects. *Earthquake Engg. Struct. Dyn.* 41, 495–513.
46. Kramer, L. Steven, (1996). Geotechnical Earthquale Engineering. *Prentice-Hall International Series in Civil Engineering and Engineering Mechanics*.
47. Kulkarni (2016). Seismic performace of a bridge with tall piers. *Proceedings of the Institute od Civil engineers, Bridge Engineering.*
48. Kwon Ho Chul, Kim Man Cheol and Lee In Won, (1998). Vibration control of bridges under moving loads. *Computers & Structures* Vol. 66, No. 4, pp. 473-480.
49. Lavorato, D., Bergami, A., Nuti, C. & Vanzi, I. (2018). Asynchronous earthquake strong motion and RC bridges response. *Journal of Traffic and Transportation engineering,* Vol 5. 454-466.
50. Liang Xiao & Sritharan Sri, (2018). Effects of confinement in circular hollow concrete columns. *Journal of structural engineering*, *ASCE*, 144(9)
51. Li, B., Bi, K., Chouw, N., Butterworth, J. W. and Hao, H. (2012a). Experimental investigation of spatially varying ground motions on bridge pounding, *Earthquake Engg. Struct. Dyn.* 41, 1959–1976.
52. Li, J., Su, M. and Fan, L. (2005). Vibration control of railway bridges under high-speed trains using multiple tuned mass dampers. *Journal of Bridge Eng*., 10, 312-320.
53. Lupoi, A., Franchin, P., Pinto, P. E. & Monti, G. (2005). Seismic design of bridges accounting for spatial variability of ground motion. *Earthquake Engineering and Structural Dynamics* 34, 327–348.
54. Maekawa, K., Pimanmas, A. & Okamura, H. (2001). Nonliner mechanics of reinforced concrete. *London:SPON Press*

55. Mander, J. B., Priestley, M. J., and Park, R. (1988). Theoretical stress-strain model for confined concrete. *Journal of structural engineering*, 114(8):1804–1826.
56. Mander, J. B, Priestley, M.J., and Park, R. (1988). Observed stress-strain behaviour of confined concrete. *Journal of structural engineering*, 114(8):1827–1849.
57. Martin, G. R., Seismic design of pile foundations : Structural and geotechnical issues. *International Conference on Recent Advances in Geotechnical Earthquake Engineering and Soil Dynamics* (1995).
58. Matlock, H. & Bogard, D. (1980). Simplified calculation of p-y curvesfor laterally loaded piles in sand. *Earth Technology Corporation, Inc*.
59. Miguel Leticia Fleck Fadel & Santos Gulherme Piva dos (2021). Optimization of Multiple Tuned Mass Dampers for Road Bridges Taking into Account Bridge-Vehicle Interaction, Random Pavement Roughness and Uncertainties. *Hindwai, Shock & Vibration,* Volume 201, Article ID 6620427.
60. Miranda, E., and Bertero, V.V. (1994). Evaluation of strength reduction factors for earthquake-resistant design. *Earthquake Spectra*, 10:357–79.
61. Mirzabozorg, H., Akbari, M. and Hariri-Ardebili, M. A. (2013). Nonlinear seismic response of a concrete arch dam to spatially varying earthquake ground motions. *Asian J. Civil Eng*. 14(6), 859–879.
62. Mo, Y.L., Wong, D.C. & Maekawa, K. (2003). Seismic performance of hollow bridge columns. *ACI Structural Journal*, 100(3), 337-348
63. Mondal Apurba, Ghosh Siddhartha and G.R. Reddy, (2013). Performance-based evaluation of the response reduction factor for ductile RC frames. *Engineering Structures,* 56 (2013) 1808–1819
64. Nelson I and Weidlinger P (1977). Development of interference response spectra for lifelines seismic analysis. *Grant Report No. 2, Weidlinger Associates, New York*.
65. Paraskeva, T. S., Kappos, A. J. and Sextos, A. G. (2006). Extension of modal pushover analysis to seismic assessment of bridges. *EQ Engineering & Structural Dynamics,* 35:1269–1293
66. Park, R. and Paulay, T. (1975). Reinforced Concrete Structures. *John Wiley and Sons*
67. Popovis, S. (1973). A numerical approach to complete stress-strain curve of concrete. Cement and concrete research. Vol. 3, Issue 5, 583-599.
68. Rashid, M., Mansur, M., and Paramasivam P. (2002). Correlations between mechanical properties of high-strength concrete. *Journal of Materials in Civil Engineering*, 14(3):230–238.
69. Ranzo, G. and Priestley, M.J.N. (2001). Seismic performance of circular hollow columns subjected to high shear. Report No. SSRP-2001/01, *University of California, San Diego, La Jolla, CA*
70. Reese, L.C., Isenhower, W.M., Wang, S.T. (2006). Analysis and Design of Shallow and Deep Foundation, *John Wiley and Sons Inc*. New Jersey.
71. Saatcioglu Murat and Razvi R. Salim, (1992), Strength and ductility of confined concrete. *Journal of Structural Engineering, ASCE.* 118:1590-1607.
72. Sandi, H. (1970). Conventional seismic forces corresponding to nonsynchronous ground motion. *Proc of 3rd European Symp Earthquake Engineering, Sofia, Bulgaria*.

73. Salcher, P., Adam, C., and Kuisle, A. (2019). A stochastic view on the effect of random rail irregularities on railway bridge vibrations. *Structure and Infrastructure Engineering*, vol. 15, no. 12, pp. 1649–1664.
74. SeismoMatch: Earthquake Software for Response Spectrum. SeismoSoft, Italy.
75. Soong, T. T. and Dargush, G. F. (1997). Passive Energy Dissipation Systems in Structural Engineering. *John Wiley & Sons*, Chichester, NY, USA, 1997.
76. Tajimi, H. (1960). A statistical method of determining the maximum response of a building structure during an earthquake. *Proceedings of the 2nd World Conference on Earthquake Engineering,* Tokyo, Vol. 2, pp 781-797.
77. Wang, J. F., Lin, C. C. and Chen, B. L. (2003). Vibration suppression for high-speed railway bridges using tuned mass dampers. *Int. J. Solids Struct*., 40(2), 465-491.
78. Xia, H., Zhang, N., and Roeck, G. De. (2003). Dynamic analysis of high speed railway bridge under articulated trains. *Computers & Structures*, vol. 81, no. 26-27, pp. 2467–2478.
79. Yang, Y.B. and Wu, Y.S. (2001). A versatile element for analysing vehicle-bridge interaction response. *Engineering Structures*, 23(5), pp: 452-469.
80. Yang, Y.B., Yau, J.D. and Wu, Y.S. (2004). Vehicle–bridge interaction dynamics with applications to high-speed railways. *World Scientific Publishing Co*., Singapore.
81. Yeh, Y.K., Mo, Y.L. and Yang, C.Y. (2002). Seismic performance of rectangular hollwo bridge columns. *Journal of Structural Engineering, ASCE*, 128(1), 60-68
82. Zhang, Y. H., Li, Q. S., Lin, J. H. and Williams, F. W. (2009). Random vibration analysis of long-span structures subjected to spatially varying ground motions. *Soil Dyn. Earthq.* Eng. 29, 620–629.
83. Zambrano, A., Rauci, M., and Malangone, P. (2008). Vehicle structure interaction to analyse the primary dynamic aspects of railway bridges. *Structure and Infrastructure Engineering,* vol. 4, no. 2, pp. 107–121.
84. Zerva, A. and Zerva, V. (2002) Spatial variation of seismic ground motions: An overview. *Applied Mechanics Reviews* 55, 271–296.

List of publications

Conferences:

S. Sengupta, S. Kanike & A. Dutta, "Numerical analysis for multi-support excitation of a long bridge with tall piers", Seventh International conference on Civil, Structural & Environmental engineering computing (CIVIL/COMP- 2023), Held at Pecs, Hungary from 28th to 31st August, 2023.

Journals:

S. Sengupta & A. Dutta, "Response reduction factor of large hollow circular section with opening" – Communicated to IABSE